



Universiteit
Leiden
The Netherlands

Nuclear magnetic resonance force microscopy at millikelvin temperatures

Haan, A.M.J. den

Citation

Haan, A. M. J. den. (2016, March 9). *Nuclear magnetic resonance force microscopy at millikelvin temperatures. Casimir PhD Series*. Retrieved from <https://hdl.handle.net/1887/38444>

Version: Not Applicable (or Unknown)

License: [Licence agreement concerning inclusion of doctoral thesis in the Institutional Repository of the University of Leiden](#)

Downloaded from: <https://hdl.handle.net/1887/38444>

Note: To cite this publication please use the final published version (if applicable).

Cover Page



Universiteit Leiden



The handle <http://hdl.handle.net/1887/38444> holds various files of this Leiden University dissertation

Author: Haan, Arthur den

Title: Nuclear magnetic resonance force microscopy at millikelvin temperatures

Issue Date: 2016-03-09

Nuclear magnetic resonance force microscopy at millikelvin temperatures

PROEFSCHRIFT

ter verkrijging van
de graad van Doctor aan de Universiteit Leiden,
op gezag van Rector Magnificus prof. mr. C.J.J.M. Stolker,
volgens besluit van het College voor Promoties
te verdedigen op woensdag 9 maart 2016
klokke 15.00 uur

door

Arthur Mattheus Johannes den Haan

geboren te Brouwershaven
in 1985

Promotor: Prof. dr. ir. T. H. Oosterkamp

Promotiecommissie: Prof. dr. C. L. Degen (ETH Zurich, Zurich, Switzerland)
Dr. R. J. C. Spreeuw (University of Amsterdam)
Prof. dr. J. Aarts
Dr. M. P. Allan
Prof. dr. E. R. Eliel

Casimir PhD series, Delft-Leiden 2015-37

ISBN 978-90-8593-243-7

An electronic version of this thesis can be found at <https://openaccess.leidenuniv.nl>

The work described in this thesis is part of the research programme of the Foundation for Fundamental Research on Matter (FOM), which is part of the Netherlands Organisation for Scientific Research (NWO).

The cover shows an optical microscope image of a part of the MRFM setup with the cantilever and the sample.

To my parents

Contents

1	Introduction	1
2	Experimental setup and methods	5
2.1	Measuring forces and force gradients in magnetic resonance force microscopy	5
2.2	Overview of the experimental setup	7
2.3	Detecting the cantilever motion with a SQUID	8
2.4	Sample characterization	11
2.5	Sample fabrication	13
2.6	Basic protocol of the experiment	16
2.7	Experimental limitations	17
3	Theory and experimental improvements	19
3.1	Sensitivity and force noise	19
3.2	Frequency noise	21
3.3	Comparison of a force measurement and a frequency measurement	23
3.4	T_1 requirements of spins	26
3.5	RF wire: dissipation	26
3.6	NbTiN RF wire: reduced repulsion	28
4	Probing the magnetic moment of FePt micromagnets prepared by Focused Ion Beam milling	31
4.1	Introduction	31
4.2	Fabrication	32
4.3	Characterization	34
4.4	Discussion	37
4.5	Conclusion	37
5	Atomic resolution scanning tunneling microscopy in a cryogen free dilution refrigerator at 15 mK	39
5.1	Introduction	39
5.2	Vibration isolation of the cryostat	40
5.3	STM setup and experimental preparation	44
5.4	Results	47
5.5	Conclusion	49

6 Spin-mediated dissipation and frequency shifts of a cantilever at millikelvin temperatures	51
6.1 Introduction	52
6.2 Theory	52
6.3 Experimental setup	55
6.4 Methods	55
6.5 Discussion	58
6.6 Conclusion	59
7 Nuclear magnetic resonance force microscopy at millikelvin temperatures	61
7.1 Introduction	61
7.2 Experimental setup	62
7.3 Methods	62
7.4 Results	65
7.5 Discussion	67
7.5.1 The Korringa constant	67
7.5.2 The resonance slice thickness	68
7.6 Conclusion	69
8 Radio frequency pulses for nuclear magnetic resonance force microscopy	71
8.1 The motion of a magnetic moment in an external magnetic field	71
8.2 Time varying magnetic field	72
8.3 Sending an RF field	73
8.4 Common RF pulses	74
8.5 Adiabatic inversion	74
8.6 T_2 measurements with B_1 insensitive rotation (BIR)	78
8.7 Pulse sequences for MRFM: OSCAR and CERMIT	80
8.8 Pulse sequences for MRFM: cyclic adiabatic driving	82
8.9 T_1 and T_2 measurements with a single adiabatic inversion	84
A Copper sample fabrication	89
A.1 Patterning pick-up coil and RF-line	89
A.2 Reactive ion etching	89
A.3 Fabricating the second copper layer	90
A.4 Sputtering copper and gold	90
A.5 Lift off	91
B Transformation algorithm for cantilever positioning	93
Bibliography	101
Samenvatting	111
Publications	115

Curriculum Vitae	117
Acknowledgments	119

Chapter 1

Introduction

Magnetic resonance force microscopy (MRFM) has been introduced as a possible tool to obtain nanometer 3D resolution or even the 3D atomic structure of biological samples and proteins for structural biology [1]. The resolution of this technique is still limited by experimental factors, such as thermal force noise (see chapter 2) and the interaction with fluctuations in the surface. Although a resolution of < 10 nm has been achieved with nuclear magnetic resonance force microscopy [2], improvement of orders magnitude in sensitivity is required to efficiently measure the 3D atomic structure of a sample.

To put this into perspective, several other techniques have been successfully implemented to uncover biological structures [3, 4, 5]. The most prominent techniques are X-ray crystallography, in which many identical proteins are coaxed to form a crystal, nuclear magnetic resonance (NMR) and cryo-electron microscopy (cryo-EM). These tools have delivered detailed information on the 3D atomic composition of many protein structures [6, 7] and play an essential role in the current development of pharmaceutical drugs [8, 9, 10] and research in protein misfolding [11]. The knowledge of the mechanisms and the use of computer models is highly dependent on the data (and also the availability of the data [10]) provided by these tools.

Despite the large database of proteins, only a small fraction of the revealed proteins are membrane proteins, which are targets for 50% of the drugs [12]. Moreover, they comprise 20-30% of the total number of proteins in a genome [13, 14]. This relative low number of generated 3D-structures of membrane proteins is due to the technical limitations of the current available techniques [15].

Given the importance of structural biology in current research and the possibility to image membrane proteins, investigation and development of magnetic resonance force microscopy as an extra tool may have significant value. In addition, given the high risks (of invested capital) in pharmaceutical research and the reduction of this risk by new techniques uncovering 3D-protein structures in membranes, shows this increasingly well.

Most of the MRFM-experiments are performed at temperatures near the boiling point of liquid helium (4.2 K). These low temperatures provide a considerable improvement in comparison with room temperature measurements, since the minimal

detectable magnetic moment μ_{min} (as explained in chapter 2 and chapter 3) is given by:

$$\mu_{min} = \frac{1}{G} \sqrt{4\Gamma k_B T \Delta f} \quad (1.1)$$

Where $\Gamma = \frac{\sqrt{km}}{Q}$ is the damping, $G = \partial B / \partial x$ is the gradient of the magnetic field, k_B is the Boltzmann constant, T is the temperature, Δf is the bandwidth and k , m and Q are the spring constant, mass and quality factor of the cantilever respectively.

We try to improve this force sensitivity by more than a factor 10 by measuring at millikelvin temperatures. Moreover, in this low millikelvin temperature regime, many unclear phenomena in condensed matter physics are present. The use of MRFM as a tool for condensed matter physics at millikelvin temperatures is focused on another direction in research, which may contribute on its pathway to the development of MRFM as a tool for the imaging of 3D biological samples.

In this thesis, several other implementations aimed at improving the sensitivity, and thus lowering the minimal detectable magnetic moment, will be introduced. As a milestone, we show magnetic force measurements and nuclear magnetic resonance force measurements below 50 mK temperatures in chapter 6 and chapter 7. Requirements in terms of sensitivity for these measurements are less stringent than for the imaging of biological samples, which makes other (advanced) condensed matter measurements with the current setup possible in the near future.

Recently, diamond cantilevers with high quality factors and low force noise have been developed [16], which may (using the optimal cantilever shape) reduce the force noise by a factor of ten. In addition, a significant improvement of sensitivity may be obtained by using smaller magnets. In chapter 4, the fabrication of a new and smaller magnetic particle will be discussed. Another important factor is the dissipation due to the interaction of the cantilever with the paramagnetic spins in the material, which will be discussed in chapter 6. By using different substrate materials this influence can be reduced as well.

The construction of the thesis is such that the first two chapters (chapter 2 and chapter 3) form the foundation of the thesis in which the experimental setup and the theory will be discussed. Subsequently, chapter 4 and chapter 5 show experimental improvements for MRFM. Several of these improvements enabled the results in magnetic force measurements and nuclear magnetic resonance force measurements, as discussed in chapter 6 and chapter 7. Finally, in chapter 8, the use of different RF-pulses and adiabatic inversion, which may be helpful for future experiments with our current setup, will be discussed.

To be more specific:

- In chapter 2, the focus is directed to the experiments, in which the experimental setup, sample preparation and experimental limitations will be described.
- In chapter 3, the experimental limitations, focused on noise sources will be further evaluated.
- In chapter 4, the design, fabrication and measurement of a smaller magnet with higher field gradients (G) will be discussed. This higher field gradient would yield significant better sensitivity (see Eq. 1.1).

- In chapter 5, vibration reduction measures implemented in our cryogen free dilution refrigerator will be discussed. Moreover, the low vibrations in the cryostat enabled us to perform a benchmark atomic resolution scanning tunneling microscopy experiment on graphite. With these low vibrations, the effective mode temperature (at the eigenfrequency of the cantilever) is dominated by the thermal bath of the cantilever, i.e. the effective mode temperature is thermally limited. When performing cantilever cooling, these low vibration become even more important. We were able to cool the cantilever to $160 \mu\text{K}$, partly due to the efforts in vibration reduction [17].
- In chapter 6, magnetic force measurements on the Si/SiO₂-interface will be discussed. With these measurements a new semi-classical description of the interaction of a para-magnetic spin, having longitudinal and transverse relaxation, with the cantilever is tested.
- In chapter 7, nuclear magnetic resonance force microscopy measurements on a copper sample are described. In these experiments we performed saturation/recovery experiments as a function of frequency, distance and temperature. The temperature dependence measurements correspond to the Korringa relation [18, p. 363].
- Finally in chapter 8, an introduction to NMR and adiabatic pulses will be given. This chapter can also be read first when not familiar with this subject.

Chapter 2

Experimental setup and methods

In this chapter, we will provide a basic description of the principle of mechanical detection of nuclear or electron spins by magnetic resonance force microscopy.

In section 2.1 we will explain that the interaction can be measured as a force, which results in a displacement of the cantilever, or as a force gradient, which results in a frequency shift. In section 2.2 we will give a basic overview of the experimental setup, while in section 2.3 we pay special attention to the SQUID detection mechanism, which is different from the conventional laser interferometry used in other laboratories. In section 2.4 and section 2.5, the characterization and fabrication of the sample will be discussed. Finally in sections 2.6 and 2.7 we discuss the basic experimental protocol and the experimental limitations that one runs into, when performing this complex experiment.

2.1 Measuring forces and force gradients in magnetic resonance force microscopy

In figure 2.1 we present a simple setup consisting of a cantilever plus magnet and a sample containing spins with magnetic moment μ and an RF wire to generate the necessary oscillating B_1 fields to manipulate the spins.

The simplest model describes the interaction of a spin with magnetic moment μ with a magnetic cantilever starting from the Zeeman splitting Energy E of a spin in a high magnetic field and calculating the force or force gradient experienced in the sensitive direction of the magnetic cantilever by taking the derivative [19, 20]:

$$E = -\boldsymbol{\mu} \cdot \mathbf{B} \quad (2.1)$$

$$F_{xspin} = -\nabla E = \boldsymbol{\mu} \cdot \frac{\partial \mathbf{B}}{\partial x} \quad (2.2)$$

$$k_{xspin} = \frac{\partial F_{xspin}}{\partial x} = \boldsymbol{\mu} \cdot \frac{\partial^2 \mathbf{B}}{\partial x^2} \quad (2.3)$$

Where \mathbf{B} is the experienced magnetic field by the spin. The sensitive direction of the cantilever is taken in the x-direction. In these equations, we assumed that the magnetic moment is fixed by the large external magnetic field. For spins in a low external magnetic field, there are two ingredients missing in these equations. First of all, the spin might react to a motion of the magnetic sensor, changing the interaction, and secondly the spin interacts with its environment which is characterized by a T_1 time and a T_2 time and which has an effect on its effective motion. This was recently worked out in a Lagrangian formalism by de Voogd et al. [21]:

$$k_{xspin} = \Re(F_1 + F_2 + F_{34}) \quad (2.4)$$

$$F_{xspin} = \Re(F_1 + F_2 + F_{34})x \quad (2.5)$$

$$F_1 = -\mu_s \tanh\left(\frac{\mu_s B_0}{k_B T}\right) \left| \hat{\mathbf{B}} \cdot \frac{\partial^2 \mathbf{B}}{\partial x^2} \right| \quad (2.6)$$

$$F_2 = -\frac{\mu_s}{B_0} \frac{\frac{\mu_s B_0}{k_B T}}{\cosh^2\left(\frac{\mu_s B_0}{k_B T}\right)} \left| \hat{\mathbf{B}} \cdot \frac{\partial \mathbf{B}}{\partial x} \right|^2 \frac{1}{1 + i\omega T_1}. \quad (2.7)$$

$$F_{34} = -\frac{\mu_s}{B_0} \tanh\left(\frac{\mu_s B_0}{k_B T}\right) \left| \hat{\mathbf{B}} \times \frac{\partial \mathbf{B}}{\partial x} \right|^2 \cdot \left(1 - \frac{(\omega T_2)^2 + i\omega T_2}{(1 + i\omega T_2)^2 + (\omega_L T_2)^2} \right). \quad (2.8)$$

Where $\mu_s = |\boldsymbol{\mu}|$ is the magnetic moment of the spin, B_0 is the magnitude of the magnetic field \mathbf{B} from the magnetic tip on the cantilever, k_B is the Boltzmann constant, T is the temperature, ω is the angular eigenfrequency of the cantilever, $\omega_L \equiv \gamma B_0$ is the Larmor frequency and T_1 and T_2 the spin lattice relaxation and the spin-spin relaxation, respectively. In these equations the Boltzmann polarization is taken into account.

The forces due to a single nuclear spin or electron spin are very small. For a magnet with a diameter of $3 \mu\text{m}$ at a distance of $1 \mu\text{m}$ from the surface (Gradient field of $1 \cdot 10^5 \text{ T/m}$) this force is $1.5 \cdot 10^{-21} \text{ N}$ for a nuclear spin or $1 \cdot 10^{-18} \text{ N}$ for an electron spin. These forces need to be compared to the noise forces acting on the cantilever due to thermal fluctuations inside the cantilever or due to tip-surface interactions. According to the fluctuation dissipation theorem [22], the power spectral

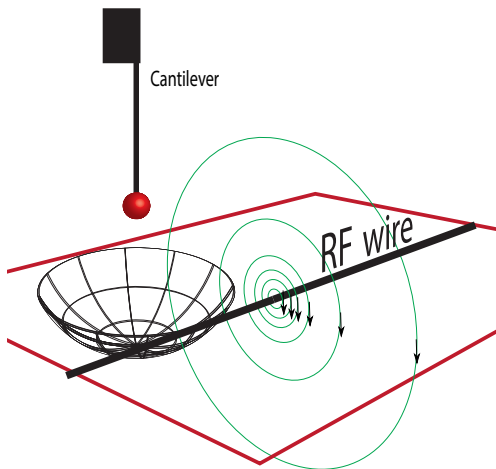


Figure 2.1: Cantilever above a sample with an RF-wire. The MRFM cantilever consists of a cantilever beam and a magnetic particle attached to its end. In the dipolar field of the magnetic particle, a selection of spins forming a bowl-shaped region are excited when the RF-wire generates an oscillating magnetic field (represented by green circles).

density of thermal force noise (in units $\text{N}/\sqrt{\text{Hz}}$) is proportional to the square root of the dissipation of the cantilever (Γ):

$$F_n = \sqrt{4k_B T \Gamma} \quad (2.9)$$

where $\Gamma = \frac{\sqrt{km}}{Q}$ is the damping of the cantilever, k_B is Boltzmann's constant and T is the temperature. The equation is valid for a single sided spectrum, i.e. only positive frequencies. Because the force noise goes down with temperature, and because there is a lot of interesting spin physics to explore there, we perform our experiments at millikelvin temperatures.

In chapter 3 we will discuss that measuring the force gradient k_x usually has a lower signal to noise ratio than measuring F_x . However, in many cases it is more straight forward to measure k_x because the requirements on the relaxation times and on the magnitude of the oscillating B_1 field necessary to manipulate the spins are more stringent for force measurements.

2.2 Overview of the experimental setup

In figure 2.2, a schematic overview of the experimental setup that we use is shown. The setup consists of a cantilever beam with a magnetic NdFeB^1 particle (tip) attached to its end which is vibrating above a pick-up coil, where the long direction of the cantilever is oriented perpendicular to the surface. Using a piezo-electric element, the cantilever can be driven. The motion of the magnetic particle creates a varying magnetic flux which is detected by a superconducting pick-up coil coupled into a superconducting quantum interference device (SQUID)² via transformers. A 3D positioning system, consisting of piezoknobs³ and capacitance sensors, is used for

¹Spherical particle from neodymium-alloy powder of type MQP-S-11-9-20001-070 by Magnequench, Singapore

²Quantum Design, Inc., USA

³Janssen Precision Engineering B.V., The Netherlands

the alignment of the cantilever above the pick-up coil and the sample. The piezoknob consists of a threaded spindle, which rotates inside a platform to which the cantilever is connected. This platform is pulled against the box containing the sample and precision positioning system (finestage), by springs. By placing three piezoknobs inside the platform, the tip of the cantilever can be moved in every 3D position in a range of several millimeters with tens of nanometers precision. The piezoknobs are turned by applying short electric pulses to piezo-electric elements oriented perpendicular to the radial direction. The torque generated by these piezo-elements cause a rotation by means of a stick-slip action at the spindle.

The readout of the position is performed by measuring the height near the piezoknobs through the capacitance measurement of three capacitance sensors, using a capacitance bridge⁴. By using a transformation algorithm (see appendix B), the three heights near the piezoknobs can be transformed to an xyz position of the tip of the cantilever. The reverse transformation can be performed by inversion after a linear approximation of the transformation algorithm.

Furthermore, a finestage with limited micrometer ($2.3 \mu\text{m}$) range is used for precise positioning of the sample in comparison with the cantilever tip, which enable scan and imaging applications. In figure 2.3a and figure 2.3b, the 3D positioning system with piezoknobs and the finestage are shown respectively.

This complete setup is shielded with niobium foil to shield varying magnetic fields and is cooled to millikelvin temperatures (10 mK - 1 K) in a cryogenfree dilution refrigerator⁵. A picture of the cryostat can be found in chapter 5, figure 5.1.

In figure 2.4, the cantilever with magnetic particle (tip) and the attachment of the magnetic particle is shown. For our experiments, we use a single-crystalline silicon cantilever beam, which was fabricated by Chui et al. at IBM [23, 24]. Special attention was paid to increase the force sensitivity in designing these cantilevers. In section 3.1, a description on the issue of cantilever improvement will be provided. The attachment of a different magnetic particle made from iron platinum (FePt) [25] is discussed in chapter 4.

2.3 Detecting the cantilever motion with a SQUID

The special feature of this setup is the SQUID detection mechanism. The choice for this detection system is based on the demand of working at millikelvin temperatures. The conventional way of detecting the motion of a cantilever is by using laser interferometry [16, 27] or laser deflection. However, at millikelvin temperatures, a downside of laser detection is cantilever heating due to absorption of the laser power on the cantilever, which decreases the force sensitivity of the cantilever. Another issue is the diffraction limit of the laser, which makes detection of smaller (nanoscale) cantilevers challenging. One of the solutions compatible with low temperatures is the SQUID detection mechanism [28], which will not heat up the cantilever directly.

Possibly, the effective temperature of the cantilever may be increased by noise generated in the detection circuit via outside sources. This may drive the cantilever

⁴2500A, Andeen Hagerling, Inc., USA

⁵CF-650, Leiden Cryogenics, The Netherlands

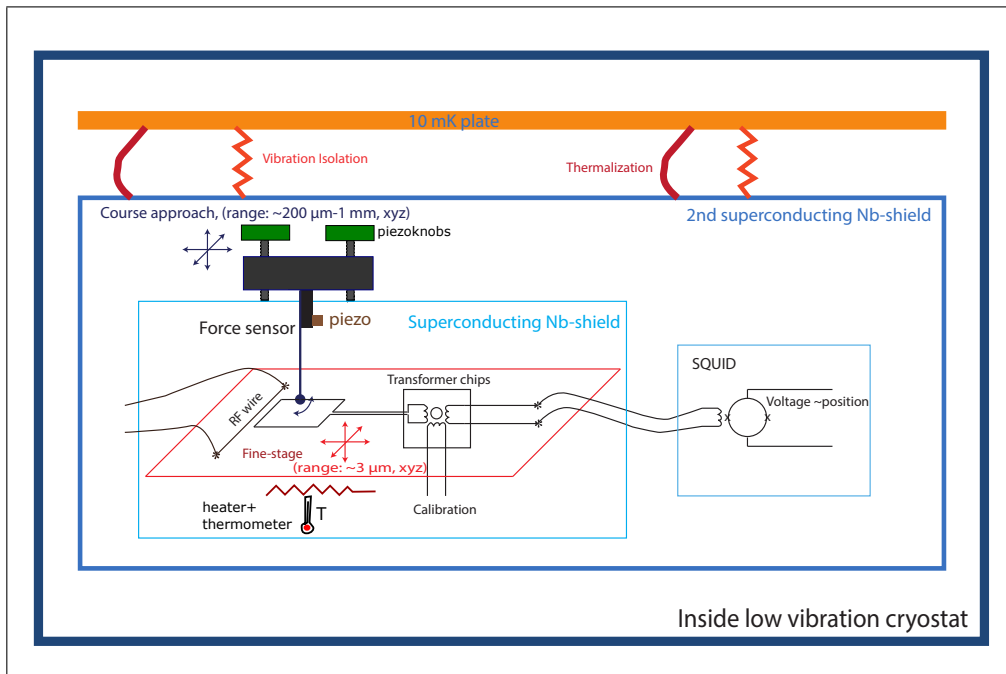


Figure 2.2: Schematic overview of the MRFM-setup inside the cryostat, with a cantilever, which can be driven by a piezo. A pick-up coil is attached via transformers to the SQUID. The pick-up coil and transformers are shielded by a niobium foil and can be moved by the finestage in a $3 \mu\text{m}$ range. The cantilever can be positioned by piezoknobs in millimeter range. The position can be read out by capacitance sensors via a capacitance bridge. The whole setup including the 10 mK plate is again shielded with niobium foil. Copper thermalization strips and vibration isolation separate the 10 mK plate from the experiment. Temperature control of the sample is obtained by using a heater and a RuO_2 thermometer with a PID control

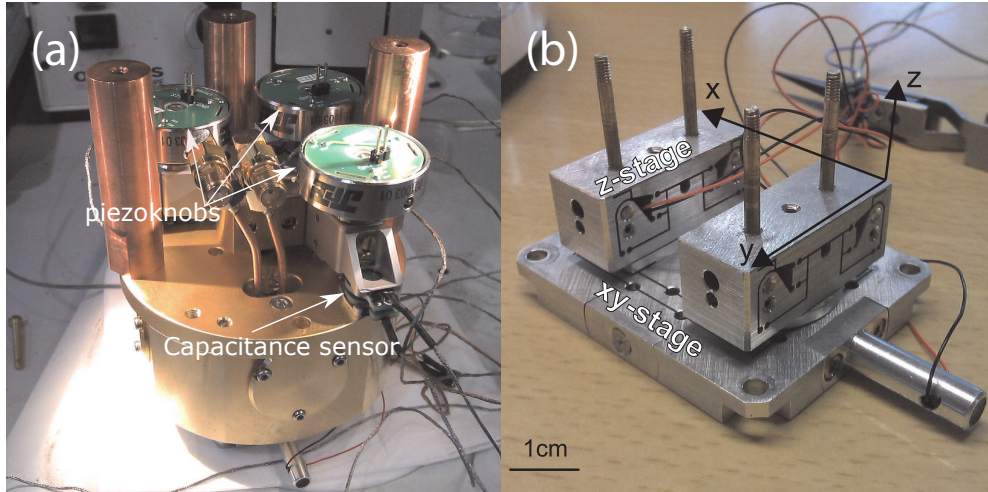


Figure 2.3: Course and fine positioning system for the MRFM. (a) 3D positioning system of the cantilever by piezoknobs and Capacitance sensors with a range of 1 mm and less than $1 \mu\text{m}$ precision. (b) The finestage for scanning the sample in x, y and z with a range of 2-3 μm . Images reproduced with permission of Dr. G. H. C. J. Wijts [26, p. 31]

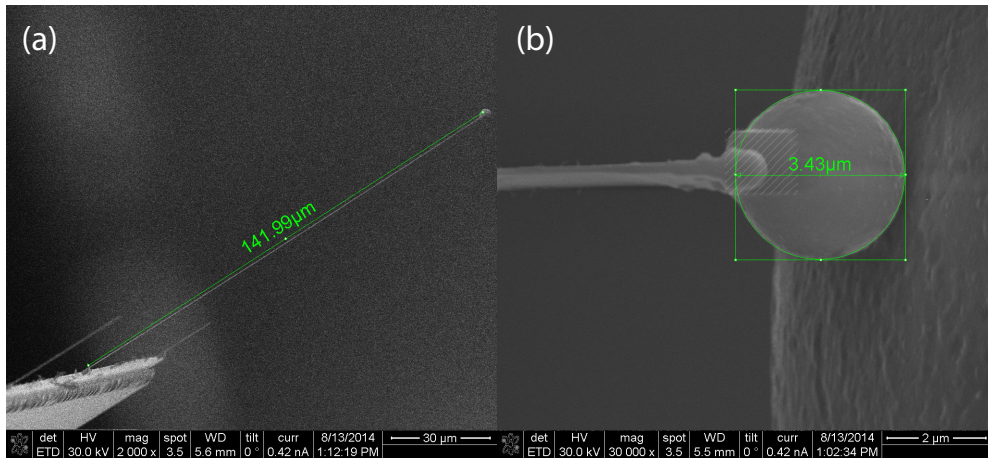


Figure 2.4: Scanning Electron Micrograph (SEM) of an MRFM cantilever. (a) Cantilever with dimensions $(l \times w \times h) = 145 \mu\text{m}, \times 5 \mu\text{m} \times 0.1 \mu\text{m}$. (b) Gluing of the magnetic particle, the hashed square indicates the area illuminated with the electron beam for electron-beam induced deposition of platinum.

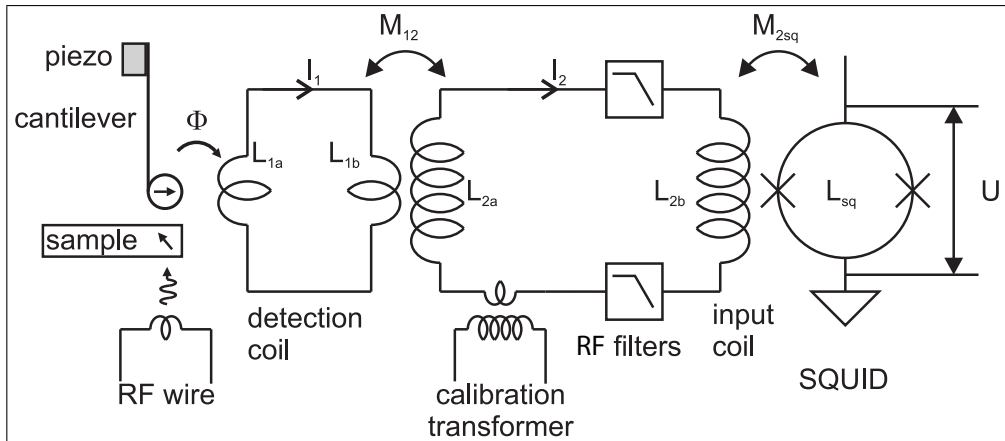


Figure 2.5: SQUID detection mechanism. The movement of the magnetic particle is coupled to the pick-up coil which is connected to a transformer. The other side of the transformer is connected via the calibration transformer and filters to the input coil of the SQUID. Image reproduced with permission of Dr. G. H. C. J. Wijts [26, p. 13].

via the pick-up coil. Superconducting shielding of the experiment lowers interference from outside sources.

In figure 2.5 an overview of the SQUID detection mechanism is shown. The pick-up coil is connected via a transformer and a calibration transformer to the SQUID⁶. This intermediate circuitry is added to decouple the SQUID from the oscillating high frequency (GHz) B_1 fields and to shield it from strong static magnetic fields, which we hope to apply in the future. Moreover, it enables the use of a calibration transformer, which calibrates the movement of the cantilever to a voltage. The signal in the SQUID can be maximized by proper choice of the transformers in which the inductances are matched. The inductance of the pick-up coil ($30 \mu\text{m} \times 30 \mu\text{m}$) is roughly 60 pH while the input inductance of the SQUID is ($1.6 \mu\text{H}$).

A detailed description of the SQUID detection mechanism and the overall setup can be found in the PhD thesis of Dr. G. H. C. J. Wijts [26, p. 13-39].

The sample under investigation is fabricated near the pick-up coil at maximum coupling, both on the same chip. The fabrication procedure will be discussed in sections 2.4 and 2.5.

2.4 Sample characterization

In chapter 7, results of nuclear magnetic resonance force measurements on a copper sample are shown. For this experiment, we used a silicon chip with a detection coil and a small copper structure. In this section and the subsequent section we will discuss the design and fabrication process of this chip.

In figure 2.6, the layout including the pick-up coil, pads, and copper sample is shown. The size of the pick-up coil is chosen to be $30 \mu\text{m}$, which provides a decent

⁶Quantum Design, Inc., USA

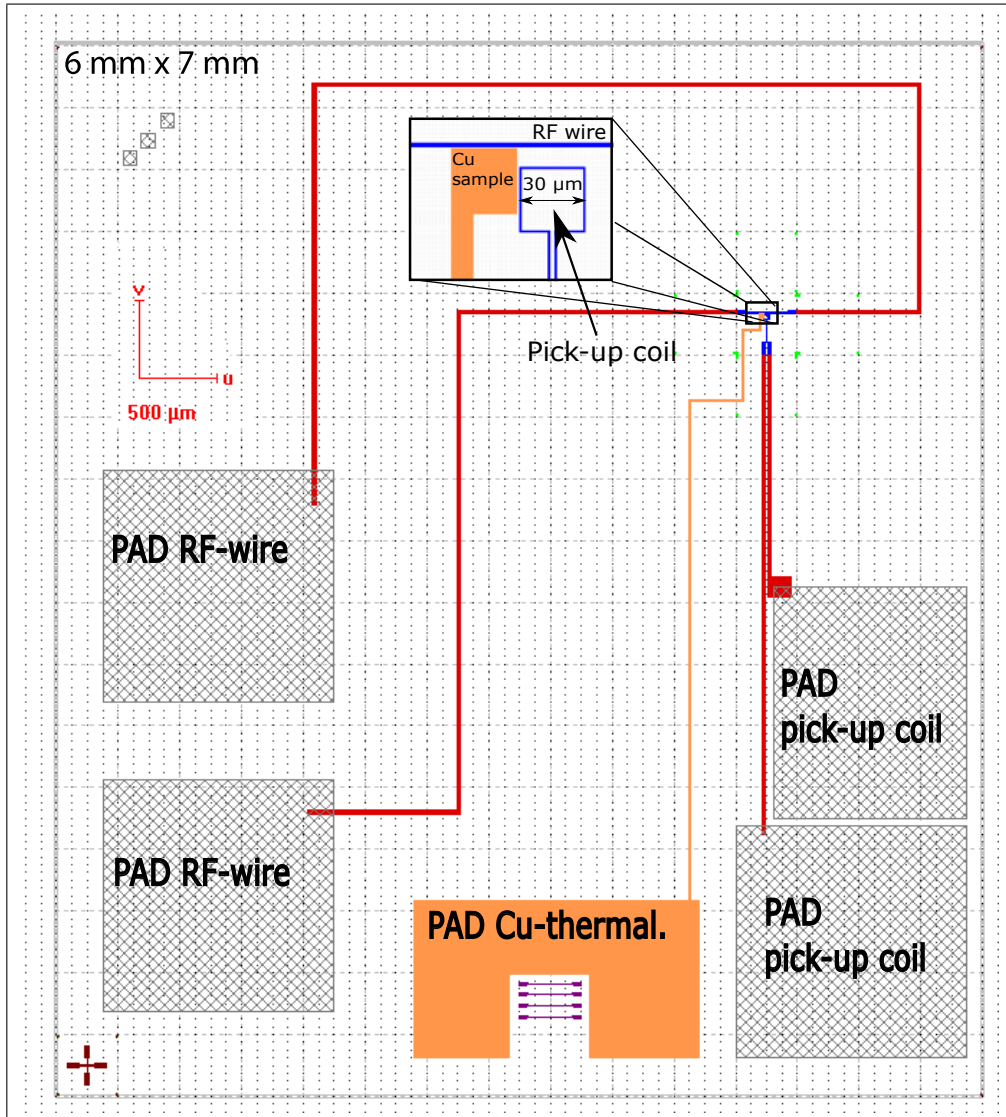


Figure 2.6: Design of the detection chip with RF wire and copper sample. A zoom-in of the pick-up coil, RF wire and copper sample is shown. The position of these structures on the chip is chosen such that the cantilever is aligned above the pick-up coil, while the pads are close to the connection points. The copper is thermalized via a copper pad, which is wire bonded to a brass sample holder. This brass sample holder is temperature controlled and connected to the 10 mK plate via a silver wire. The pick-up coil and RF wire are fabricated from a niobium titanium nitride (NbTiN) film.

coupling of the cantilever movement to the pick-up coil at large ($100\ \mu\text{m}$) and small ($2\text{-}10\ \mu\text{m}$) distances. An optimal coupling at small distances would be obtained if the coil size approaches the size of the magnetic particle (micrometer size). However, the coupling strength would then only be high on a local scale, and it would be difficult to find the pick-up coil during initial approach.

The copper sample is designed to be as close to the RF wire ($500\ \text{nm}$ gap) as possible and having still enough cantilever-coupling to the pick-up coil at that position. This coupling depends on the orientation of the magnetic moment of the tip and the direction of movement of the cantilever. It is favorable to orient the direction of movement to be parallel to the RF-wire (x-direction), such that electrostatic interactions and magnetic fields from the RF wire do not significantly influence the sensitive mode of the cantilever. In the presence of an external magnetic field, maximum signal is obtained when the orientation of the magnet is in the y-direction, perpendicular to the vibration direction of the cantilever [29]. The coupling strength for these orientations as a function of position above the coil is shown in figure 2.7a and figure 2.7b. Taking these considerations into account, we see that a high coupling at the place of the copper sample can be achieved, while a large B_1 -field can be generated by the RF-wire. In addition, cross-talk with RF and external field can be minimized in this configuration. A downside to having a y-polarized magnetic particle is that the range of high coupling is smaller than for an x-polarized particle. In the experiment described in chapter 7, the polarization of the magnetic particle is in the x-direction because the experiment was yet without external magnetic field. If we look at the coupling strength for the x-polarized particle, we see that the maximum coupling is achieved near the lines along the y-direction of the pick-up coil. The copper square ($30\ \mu\text{m} \times 30\ \mu\text{m}$) is placed close to the pick-up coil ($1\ \mu\text{m}$) and the RF wire ($500\ \mu\text{m}$), giving a high coupling above the copper near the RF-wire, both for an x-polarized and y-polarized magnetic particle.

In the design (see figure 2.6), a thermalization line was added, which is connected from the copper sample to a wire bond pad (thermalization bath). This pad is connected via gold wire bonds to a brass sample holder which is temperature controlled and thermalized. This sample holder in turn was thermalized via a silver wire ($1\ \text{mm}$ diameter) to the $10\ \text{mK}$ plate. This thermalization is necessary to transport the heat generated in the copper due to eddy currents originating from the B_1 field of the RF wire.

The (NbTiN) pads which are connected to the pick-up coil and the RF line are positioned such that the wire bonds to the transformer chips and RF leads can be made as short as possible.

2.5 Sample fabrication

The basic fabrication procedure of the copper sample and the pick-up coil is depicted in figure 2.8. A detailed description of the fabrication procedure can be found in appendix A. The fabrication was performed on a slice from a silicon wafer covered with a niobium titanium nitride (NbTiN) film with an average thickness of $378\ \text{nm}$. This film was developed and provided by the group of T.M. Klapwijk. In section

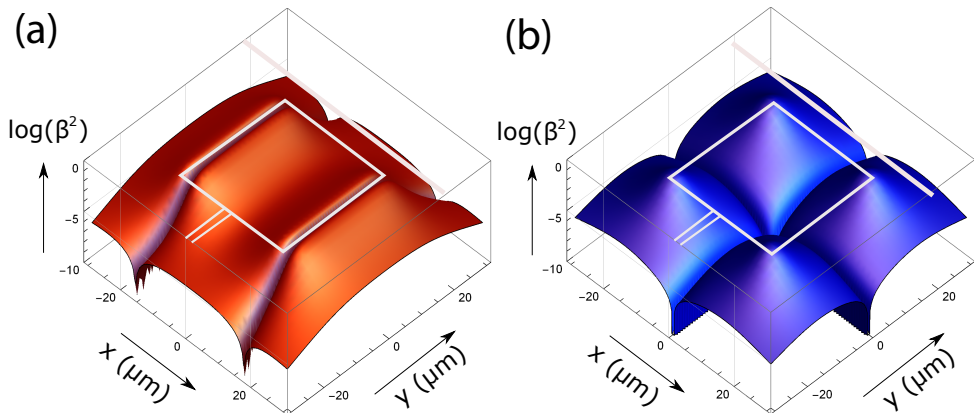


Figure 2.7: Energy coupling for two polarization configurations of the magnetic particle of the cantilever with its vibration direction in the x-direction. The maximum coupling in x- and y-direction are the same. The area of high coupling is larger when the particle is polarized in the x-direction. (a) Magnetic particle polarization in the x-direction. (b) Magnetic particle polarization in the y-direction.

3.5, more details will be discussed about this superconducting film (NbTiN), as well as the reason for choosing this film. We used negative chemically enhanced E-beam resist AR-N 7700 for the patterning of the pick-up coil, which is highly resistant to reactive ion etching (RIE). The slice was patterned⁷ with four equal structures of 6 mm x 7 mm) according to the design of figure 2.6. After patterning the pick-up coil, the RF wire, and the pads into the resist, we etched the film with negative resist by using reactive ion etching (RIE) with sulfur hexafluoride (SF_6) and oxygen (O_2) together with D. Thoen⁸. For the second layer with the copper sample, we used a lift-off procedure by a combination of two layers Polymethylmethacrylate (PMMA); a high density PMMA on top of a low density PMMA. Since the low density layer is more sensitive to E-beam exposure, an undercut is realized after exposure and development. This undercut prevents copper (or the to be deposited material) to stick to the PMMA. After these processing steps, we sputtered a 300 nm layer of copper with a gold capping layer of 16 nm to prevent oxidation of the copper. By putting the chip in an ultrasonic acetone bath at 50 °C temperature, the PMMA with copper on top dissolves. The final structure with pick-up coil, RF-wire and copper sample is shown in figure 2.9.

⁷Raith E-line lithography system

⁸from the group of T.M. Klapwijk in the Kavli institute

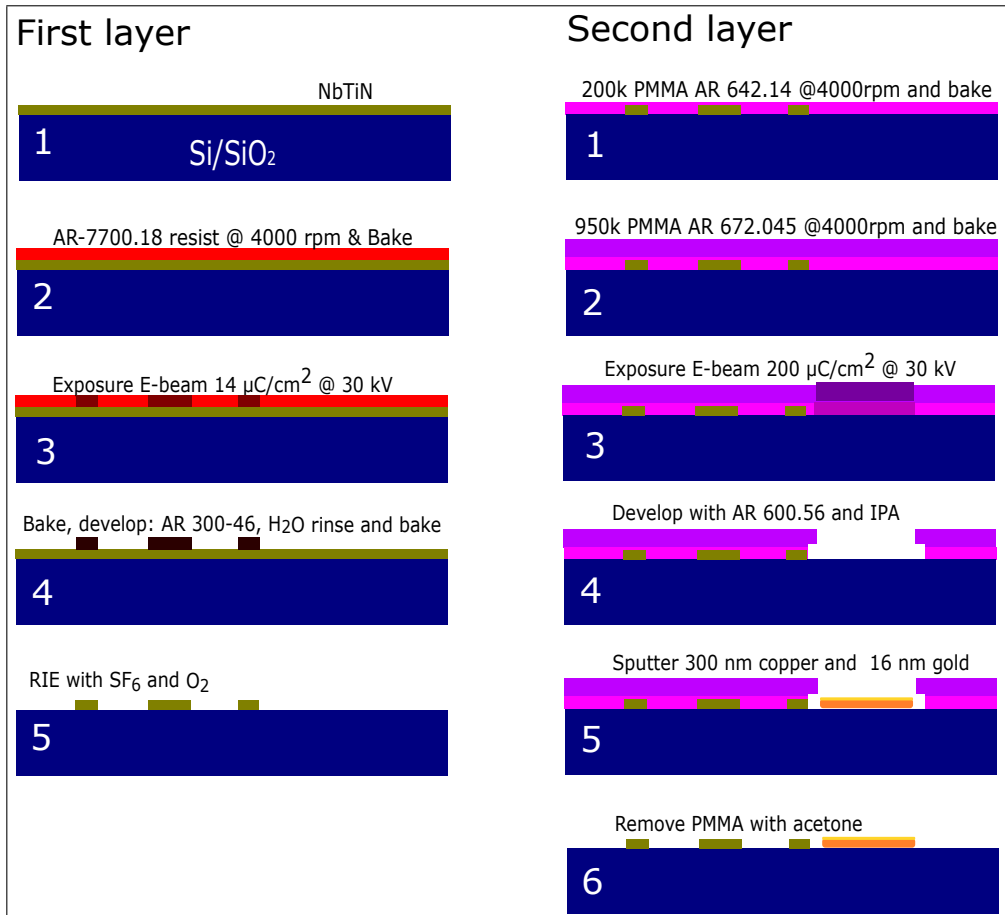


Figure 2.8: Fabrication process.

First layer process: (1) The starting configuration as provided by T.M. Klapwijk and D. Thoen, (2) Spin coated resist at 4000 rotations per minute (rpm) and baked at 85 °C for 1 min. (3) E-beam exposure. (4) Baked at 105°C for 2 min and developed for 60 sec. and finally baked (to be etch resistant) at 120°C for 2 min. (5) Reactive Ion Etching (RIE).

Second layer process: (1) Applied low density PMMA and baked at 160°C for 3 min. (2) High density PMMA and 3 min. 160°C bake. (3) E-beam exposure. (4) 3 min. developer and isopropanol stopper. (5) Copper and gold sputtering. (6) Lift-off in ultrasonic bath of acetone at 50°C.

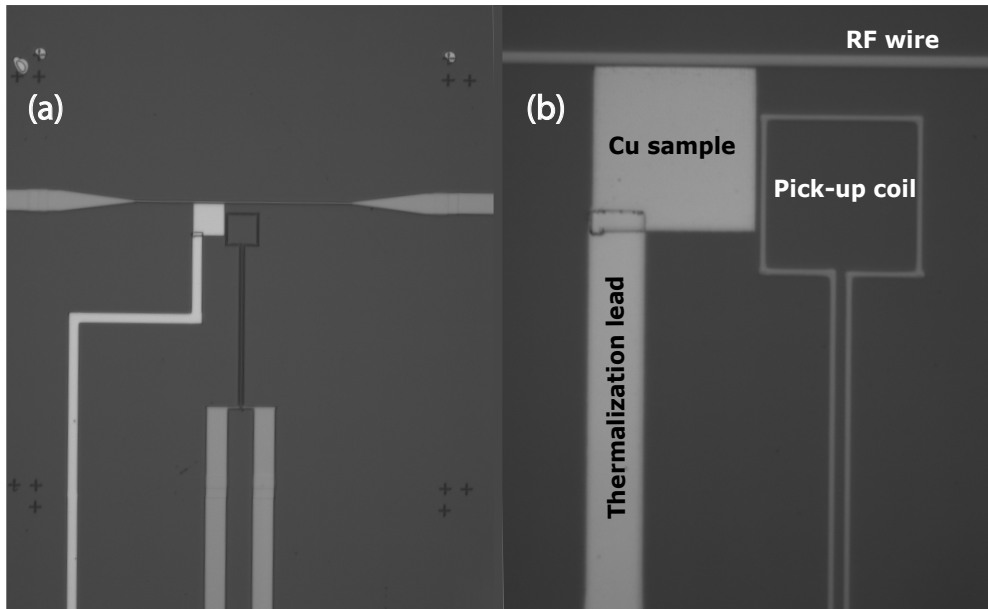


Figure 2.9: Detection chip with copper structure. The pads are outside the view of this image. Markers are visible at the corners, which were necessary for the precise alignment of the second copper layer. (a) Markers, pick-up coil, RF wire and sample. (b) Zoom in.

2.6 Basic protocol of the experiment

The actual experiment roughly consists of the following steps:

- Wire bonding of the detector chip, transformer chip and calibration coil, such that the entire circuit from pick-up coil to SQUID is superconducting at low temperatures. We used aluminum bonding wires for this purpose, which have a critical temperature T_c around 1 K. This means that experiments cannot be performed above 1 K, because the noise rises and sensitivity goes down when the circuit is not superconducting. Higher T_c bonding wire materials such as niobium are difficult to wire bond.
- A manual course alignment of the magnetized cantilever above the pick-up coil, using an optical microscope.
- Correcting for the expected drift, which is approximately the same for each run. When cooling down, the cantilever is back at the intended position within $50 \mu\text{m}$.
- Checking the connections to all piezoelectric elements, heaters and temperature sensors and subsequently grounding the piezoelectric elements.
- Cooling down the refrigerator.

- Tuning the SQUID for optimal sensitivity and driving the cantilever to see whether a detectable signal due to the cantilever motion can be observed.
- Moving the cantilever using the coarse approach motors (piezoknobs) and measuring the coupling with the pick-up coil for each location and compare to theory. This facilitates the localization of the center of the pick-up coil. An example of the coupling as a function of position above a coil is shown in figure 2.10.
- From there it is possible to find the sample and start an experiment.

2.7 Experimental limitations

In practice, there are some bottlenecks that limit the experiment. In this section we briefly describe the main limitations to the sensitivity as well as the limits to the total time or effort needed for the experiment.

In order to start a measurement, the cantilever has to be sufficiently close to the pick-up coil so that a signal due to its motion can be detected. With our current magnet, magnetization, and SQUID noise, we need the cantilever to be within $\approx 200 \mu\text{m}$ of the pick-up coil in order to be able to start optimizing the position of the cantilever. Because the coarse motor in our setup dissipates a considerable amount of energy, we can typically move the sensor for about 30 micrometer at a time, during which the setup warms up to approximately 1 Kelvin (and the mixing chamber warms up to 200 mK), and after which we need to wait for 2 hours for the setup to cool down to the starting temperature of 200 mK.

When the cantilever has reached a position where the coupling to the pick-up coil is sufficient to detect the thermal motion of the cantilever, and is sufficiently close to the sample that is to be studied, the actual experiment can be performed. In some cases, the damping of the cantilever depends very strongly on the distance to the sample surface. This is the case if the sample is a good conductor as is the case for the copper sample studied in chapter 7. In chapter 6 we study the damping of our cantilever near an oxidized silicon surface, where the damping is determined by the paramagnetic surface spins which couple to the magnet on the cantilever.

Even though the dilution refrigerator is at 10 or 15 mK, it remains to be seen in practice whether the thermodynamic temperature of the cantilever also reaches this temperature. In the past we have seen that the temperature of the fundamental mode of the cantilever does not go down anymore when the refrigerator temperature goes below 25 mK [28]. However, this was in a simplified geometry, without a coarse approach motor and without an RF line. In our first experiments with a complete MRFM experiment the lowest temperature of the fundamental mode of the cantilever was limited to 56 mK [26, p. 87], for an experiment where electrons were excited. In our experiments in which we excite nuclei we have achieved a mode temperature of 139 mK, because the higher RF currents needed to excite the nuclei precluded the use of the filtering we designed for the RF line. This can still be improved in the future.

The material choice of the magnetic particle on the cantilever is quite important. Since we work without an externally applied magnetic field, we need a material with a large remanent magnetization and a large coercive field. After magnetizing the

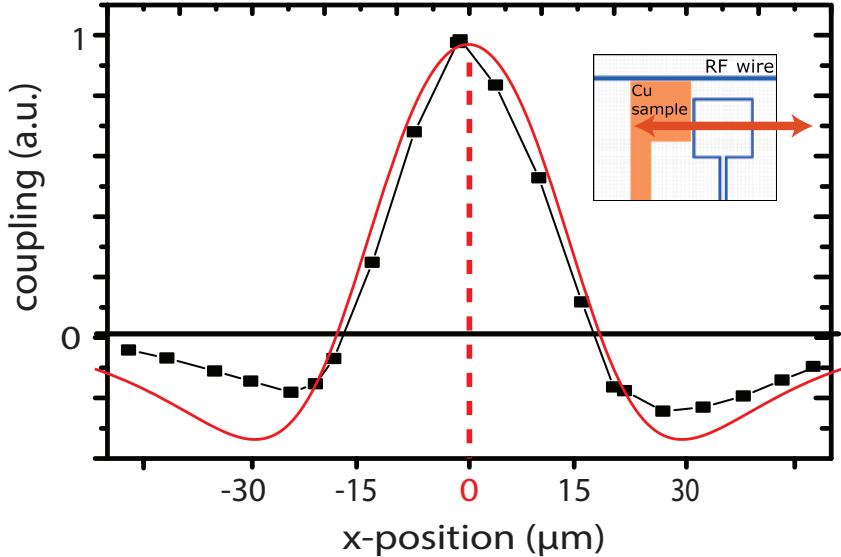


Figure 2.10: Measured and simulated coupling to the SQUID as a function of the x-position. The red solid line is the calculated flux change in a square loop due to the cantilever with a magnetic dipole. The magnetic moment and vibration direction are oriented along the x-axis. The inset shows the scan over the pick-up coil.

magnet, we would like to obtain a large magnetic moment, but also we hope to avoid magnetic fluctuations coming from the magnet. In chapter 5 of this thesis we have developed a cantilever with an FePt tip, which hopefully provides these material properties. However, we did not yet test this tip in a complete MRFM experiment.

When applying an RF pulse to manipulate the spins, an oscillating B_1 field needs to be generated. This B_1 field can be generated by a coil or a micron-sized RF wire. In order to obtain high signal to noise ratio MRFM experiments, such as described in chapter 8, high B_1 fields of approximately 4 mT are needed. These high fields close to the RF wire can only be obtained if the currents are in the order of 20-40 mA. Therefore, RF heat dissipation at low temperatures plays a crucial role. We use a superconducting RF line, which lowers the dissipation in comparison with copper [30], but still shows considerable heat-dissipation at NMR frequencies [31, p. 32-33]. Another limitation of using a superconductor is the Meissner effect which repels the cantilever and therefore creates so called ‘forbidden areas’ in which the effect of the repulsive forces exceed the spring constant of the cantilever. In chapter 3, sections 3.5 and 3.6, RF dissipation and repulsion will be discussed in more detail.

Chapter 3

Theory and experimental improvements

Improving the sensitivity of an MRFM system to enable fast measurements of single nuclear spins opens paths to new imaging methods of biological samples and condensed matter research. However, improving this sensitivity is one of the difficulties in MRFM. In this chapter we will discuss the limiting factors and requirements for a successful MRFM experiment.

In section 3.1, we discuss the main noise source and the resulting sensitivity. Since many of the experiments are performed by measuring a frequency shift, we discuss in section 3.2 the noise present in these frequency measurements. Then in section 3.3, we compare the signal to noise ratio for a force measurement and a frequency measurement. In section 3.4, we discuss the requirement of the spin lattice relaxation time (T_1 time) of spins, which needs to be in a certain range in order to measure it. Another more technical requirement is to reduce the heat which is produced when applying a B_1 field. This will be described in section 3.5. Finally, in section 3.6 the issue of repulsion between the magnetic particle and the superconducting structures will be discussed.

3.1 Sensitivity and force noise

Thermal force noise is one of the fundamental noise sources limiting the sensitivity of MRFM. In chapter 2, we already introduced the thermal force noise (Eq. 2.9). One has to minimize this force noise in order to increase the force sensitivity. As mentioned in section 2.1, one of our strategies is to lower the temperature to millikelvin temperatures. The other factor is the damping $\Gamma = \frac{\sqrt{km}}{Q}$, which sets the design parameters for the cantilever. For a rectangular cantilever, the damping is given by:

$$\Gamma = \frac{\sqrt{E\rho}wt^2}{QL} \quad (3.1)$$

Where we used $k_0 = \frac{Ewt^3}{4L^3}$, in which E is the Young's modulus, ρ is the density of the material and w, t , and L are the width, thickness and length of the cantilever respectively. From this equation, one could argue that a long, very thin and narrow cantilever with low density material leads to low damping. However, the Quality factor Q can vary with each of these parameters (dimensions, Young's modulus and material). The main dissipation channels are via impurities, defects, surface dissipation, and clamping losses [32, 33, 34]. Significant effort has been undertaken to improve on these properties [16, 35, 36, 37, 24]. When surface dissipation is dominant, we can assume that Quality factor is linearly dependent on the thickness, as can be seen in reference [16]. In this case, a specific mechanical dissipation factor α can be defined, which is independent of geometry [16]:

$$\alpha = \frac{\sqrt{E\rho}}{Q/t} \quad (3.2)$$

Hence,

$$\Gamma = \frac{\alpha wt}{L} \quad (3.3)$$

It then follows that the damping is still lowered by decreasing the width and thickness, and increasing the length.

If we compare the force noise Eq. 2.9 to the minimum detectable force from a single spin: $F_{min} = G\mu_{min}$, we see that the minimum magnetic moment which can be detected is [19]:

$$\mu_{min} = \frac{1}{G} \sqrt{4\Gamma k_B T \Delta f} \quad (3.4)$$

Where $G = \frac{\partial B}{\partial x}$ is the gradient field. From this equation we see that the size of the particle is an important factor, since the gradient field is inversely proportional to the distance (r) to the fourth power $G \propto r^{-4}$. Therefore it is useful to put effort into downsizing the magnetic particle. In chapter 4, the fabrication of a micron sized high gradient magnet will be discussed.

For typical values of the cantilever as shown in figure 2.4 in our cryostat, with eigenfrequency $f_0 = 3$ kHz, quality factor $Q = 10000$, and a spring constant $k_0 = 8 \cdot 10^{-5}$, the spectral density of the force noise is: $S_F = 1$ aN/ $\sqrt{\text{Hz}}$ at a temperature of 50 mK. For a gradient field of 10^5 T/m (for a $3 \mu\text{m}$ diameter NdFeB magnet of remanent magnetization $\mu_0 M = 1.3T$ at $1 \mu\text{m}$ distance from the surface) and using the typical values for the MRFM cantilever, the minimum magnetic moment in a 1 Hz bandwidth is $\frac{1 \text{ aN}}{10^5 \text{ T/m}} = 1 \cdot 10^{-23}$ J/T. This is in the order of 1 electron spin or 100 nuclear spins.

Recent development of low dissipation in cantilevers has resulted in diamond cantilevers with a quality factor of 6 Million at 100 mK [16]. With an optimized cantilever of this type, it is possible to obtain a force noise sensitivity of $45 \text{ zN}/\sqrt{\text{Hz}}$ at 100 mK. Assuming that no dissipative noise is present from the sample, this force noise sensitivity enables measurements of single nuclear spins in a measurement time of one second with a gradient field of $1 \cdot 10^6$ T/m. The minimum magnetic moment is in this case $4.5 \cdot 10^{-26}$ J/T.

3.2 Frequency noise

Frequency modulation of a cantilever is widely used in atomic force microscopy to measure spring constant changes due to gradient forces on the cantilever [38, 39]. In MRFM we use the same technique to measure the interaction of the nuclear spins on the MRFM cantilever. Frequency shift is measured due to reorientation of nuclear spins which change the gradient force. The method of using frequency shift is used in many MRFM experiments, such as in Cantilever Enabled Readout of Magnetization Inversion Transients (CERMIT) and saturation experiments [40, 41].

In chapter 7, a saturation experiment on copper is described in detail for which frequency shifts are used to detect spins in copper. In this section we will provide a basic description of the noise present in a frequency shift measurement. In many cases, the frequency shift is measured by using a phase locked loop, which keeps track of the cantilever frequency by keeping the phase at a fixed value by means of a PID controller and a voltage controlled oscillator. Another way is to self-oscillate the cantilever at its resonance frequency in which the cantilever is driven by the detected cantilever motion itself. In the latter case, the frequency of the cantilever is detected by a frequency counter [42]. Measurements in this section and in chapter 7 are obtained by using a phase locked loop (PLL).

The frequency noise of a cantilever setup is given by two contributing factors, which are the thermal frequency noise and the noise due to the detector.

Thermal frequency noise This noise originates from the power spectral density (PSD) of the thermal force noise on the cantilever, which is given by Eq. 2.9. This force noise is assumed to be constant over the frequency range relevant for each mode of the cantilever. The power spectral density of the stiffness shift (change in spring constant) is dependent on the spectral force noise and the cantilever driving amplitude (A) [43, 42]:

$$S_k = \frac{S_F}{A^2} \quad (3.5)$$

The corresponding power spectral density of the thermal frequency noise in units Hz^2/Hz can be approximated by:

$$S_f = \frac{S_k f_0^2}{4k_0^2} \quad S_k \ll k^2 \quad (3.6)$$

Combining Eq. 2.9, Eq. 3.5 and Eq. 3.6, results in:

$$S_{fT} = \frac{f_0 k_B T}{2A^2 \pi Q k_0} \quad (3.7)$$

Typical values that are used in our MRFM experiment are: Temperature $T = 50$ mK, eigenfrequency $f_0 = 3$ kHz, driving amplitude $A = 1$ nm, quality factor $Q = 10000$ and spring constant $k = 8 \cdot 10^{-5}$ N/m. This results in a spectral frequency shift due to thermal force noise $\sqrt{S_{fT}}$ of 0.4 mHz/ $\sqrt{\text{Hz}}$.

Detector noise When measuring the movement of the cantilever, noise will be introduced by the sensor detecting the motion, which can be a combination of several noise sources. In the case of our MRFM setup, the major noise is originating from the SQUID. The SQUID-noise is partly generated by shunt resistors [44, p. 37-42] and is composed of white noise with a $1/f$ component. Usually, the frequency of the cantilever is high enough to discard the $1/f$ component. The power spectral density of the detector noise ($S_{x_{det}}$) can be transformed to a force power spectral density $S_F(f)$ as if it would have been generated by the cantilever:

$$S_F(f) = \frac{S_{x_{det}}}{|H(f)|^2} \quad (3.8)$$

Where $H(f)$ is the transfer function of the cantilever:

$$H(f) = \frac{1}{1 - (f/f_0)^2 + if/(f_0Q)k} \quad (3.9)$$

Since the transfer function (Eq. 3.9) is a peaked function, the spectral function of the effective force noise (Eq. 3.8) increases rapidly when moving away from the resonance frequency of the resonator. Using Eq. 3.5 and 3.6, the frequency power spectral density becomes [43]:

$$S_f(f) = \frac{S_{x_{det}}f_0^2}{4A^2} \left(\left(1 - \frac{f^2}{f_0^2}\right)^2 + \frac{f^2}{f_0^2Q^2} \right) \quad (3.10)$$

Noise with PLL The phase locked loop corrects the driving frequency of the cantilever using a PID feedback system in which the phase is used as setpoint. Within the bandwidth of the PID system and the PLL, the output of the PLL is frequency-modulated equal to the frequency noise present at [45, p. 20-26]:

$$f = f_0 \pm f_m \quad (3.11)$$

Where f_m is the modulation frequency. Then, combining the detector noise PSD Eq. 3.10 and the thermal frequency noise PSD Eq. 3.7, we find for the total frequency noise power spectral density for small modulation frequencies ($f_m \ll f_0$) [42]:

$$S_f = \frac{f_0k_B T}{A^2\pi Qk_0} + \frac{2S_{x_{det}}}{A^2} \left(f_m^2 + \frac{f_0^2}{4Q^2} \right) \quad (3.12)$$

A factor 2 is introduced in this equation since the modulation is two sided around the eigenfrequency of the cantilever.

In figure 3.1, the spectral density of the frequency noise as a function of modulation frequency for different driving amplitudes (by piezo-electric driving) is shown. The measurement is performed by using the setup as described in chapter 2. The center of the magnetic particle on the cantilever is positioned above the copper at a distance of $4.5 \mu\text{m}$. Eddy currents are present at this distance, which cause the quality factor of the cantilever to drop ($Q = 1767$ at this distance), which will be discussed in chapter 7. The amplitude, as shown in the legend of the graph, is measured by the output of

the SQUID using a lock-in amplifier. This output is proportional to the displacement of the cantilever. From Eq. 3.12 we see that properties of the cantilever can be found. This may be a useful way to compare parameters such as cantilever temperature and detector noise. In 3.1 is fitted by equation 3.12, in which all parameters are known.

The movement of the cantilever is calibrated to the SQUID output voltage (Vs_q) by using the equipartition theorem (far from the surface, where $Q = 30000$) at 500 mK, yielding 11 nm/Vs_q. The temperature at the copper sample was 50 mK, but we observed a saturation of the thermodynamic mode temperature of the cantilever at 139 mK. The quality factor Q ($Q = 1767$) was measured by Lorentzian-fitting the response of the cantilever movement to a piezoelectric actuation which is frequency swept around the eigenfrequency of the cantilever. According to the calibration, the detector noise would be 55 pm/ $\sqrt{\text{Hz}}$ (corresponding to $5 \cdot 10^{-6}$ V/ $\sqrt{\text{Hz}}$). Further, it is clearly visible that the 1/f component is present.

The origin of this 1/f component is visible in figure 3.2, where the spectral density of the frequency noise at different distances is shown. The quality factor is measured at each distance by Lorentzian fitting. The same parameters as in fig 3.1 were used, with $T = 139$ mK, $A = 110$ nm (at 10 mV detected amplitude) and a detector noise of 55 pm/ $\sqrt{\text{Hz}}$. It is clearly visible that the 1/f component is dependent on the distance to the sample. The 1/f component is fitted in proportion to the dissipation ($1/Q$), with a proportionality factor of 1 Hz $\sqrt{\text{Hz}}$. Therefore probably the eddy currents cause low frequency gradient force fluctuations.

In other experiments on different surfaces, 1/f noise is also present [19]. The origin of these fluctuations is not yet completely understood.

3.3 Comparison of a force measurement and a frequency measurement

Different ways of detecting spins in a sample may result in different signal to noise ratios. In this section, we hope to give some clarity in the signal to noise ratio (SNR) and requirements for a force detection on the one hand and a frequency measurement on the other hand.

Signal to noise ratio for a force measurement and frequency shift measurement The frequency shift Δf is proportional to the stiffness shift Δk of the cantilever for small spring constant changes:

$$\Delta f = f_0 \frac{\Delta k}{k_0} \quad \Delta k \ll k_0 \quad (3.13)$$

Therefore, using Eqs. 2.9, 3.5, and 2.3, the signal to noise ratio of a frequency shift measurement is equal to:

$$SNR_{\Delta f} = \Delta k / k_{noise} \quad (3.14)$$

$$= \mu \frac{\partial^2 B}{\partial x^2} \frac{A}{4k_B T \Gamma} \quad (3.15)$$

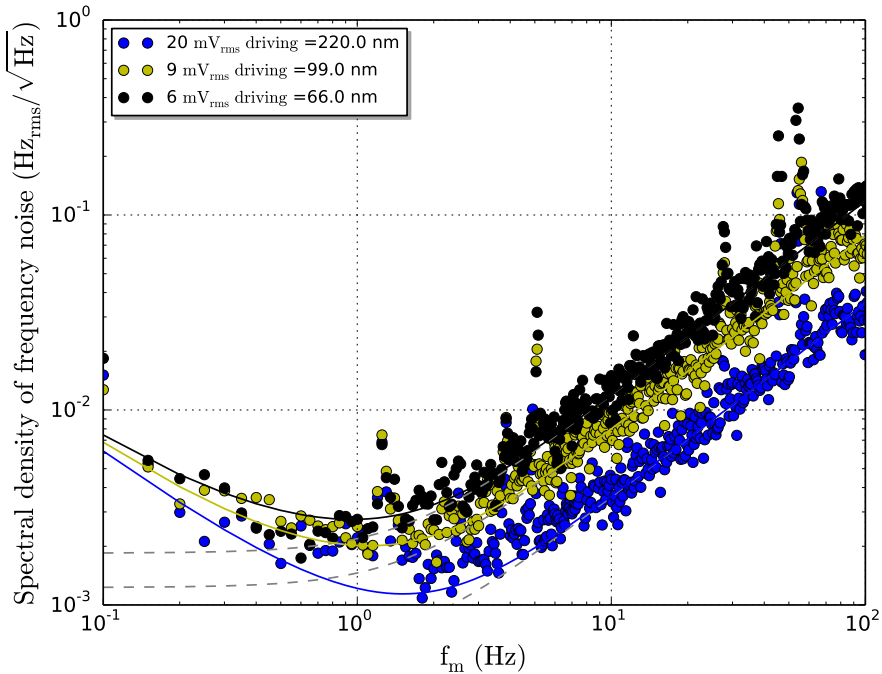


Figure 3.1: Power spectral density of the frequency noise as a function of modulation frequency for different amplitudes of an MRFM cantilever above a copper sample. Cantilever parameters: eigenfrequency $f_0 = 3000$ Hz, spring constant $k_0 = 8 \cdot 10^{-5}$ N/m, Quality factor $Q = 1767$ and thermodynamic mode temperature $T = 139$ mK. The data are fitted with Eq. 3.12. The amplitude of the cantilever motion is measured by a lock-in amplifier. The measured voltage and motion in nm is shown in the legend (with calibration 11 nm / 1 mV_{rms}). The detector noise is measured to be $5 \mu\text{V}/\sqrt{\text{Hz}}$, corresponding to 55 pm/ $\sqrt{\text{Hz}}$. The $1/f$ component is fitted with a factor $a/Q = 0.6 \cdot 10^{-3}$ Hz $\sqrt{\text{Hz}}$, with $a = 1$ Hz $\sqrt{\text{Hz}}$. The segmented gray lines represent the fits without the added $1/f$ noise component.

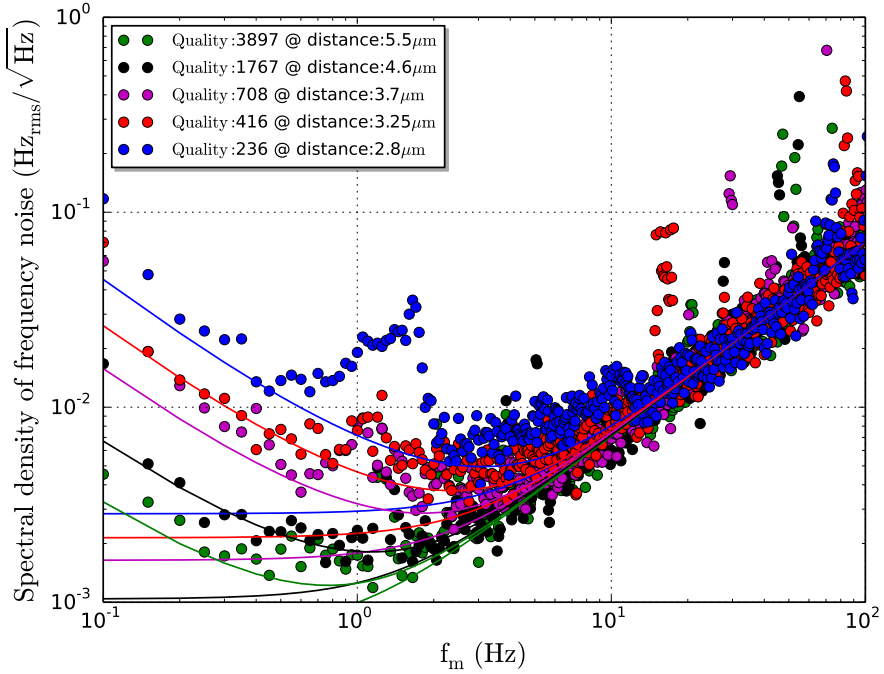


Figure 3.2: Power spectral density of the frequency noise as a function of modulation frequency for different distances of an MRFM cantilever above a copper sample at a temperature of $T = 139$ mK. At each height, the piezo-driving amplitude was set to a value such that the measured SQUID voltage was 10 mV (corresponding to a cantilever amplitude of 110 nm). The quality factor was measured by Lorentzian fitting. The cantilever parameters are the same as in figure 3.1, except that the quality factor changes with height. Likewise, the fitting parameters (amplitude = 110 nm at 10 mV and detector noise of $55 \text{ pm}/\sqrt{\text{Hz}}$) are the same. The $1/f$ noise is fitted with the function $\sqrt{S_{1/f}} = \frac{a}{Qf}$ with $a = 1 \text{ Hz}\sqrt{\text{Hz}}$

Where A is the amplitude of the cantilever motion. The signal to noise ratio of a force measurement is given by:

$$SNR_F = \Delta F / F_{noise} \quad (3.16)$$

$$= \mu \frac{\partial B}{\partial x} \frac{1}{4k_B T \Gamma} \quad (3.17)$$

Using these two signal to noise ratios, we can compare the signal to noise ratios of the frequency measurement and force measurement:

$$\text{Improvement} = \frac{SNR_F}{SNR_{\Delta f}} \quad (3.18)$$

$$= \frac{\frac{\partial B}{\partial x}}{\frac{\partial^2 B}{\partial x^2} A} \quad (3.19)$$

$$\propto \frac{d_m}{A} \quad (3.20)$$

Where d_m is the distance to the center of the magnet. For the last proportionality, we assumed a dipole magnet, which has a magnetic field proportional to the inverse cube of the distance.

From this equation, we see that it is favorable in terms of sensitivity to use the force sensing measurement when the distance is larger than the driving amplitude, which is normally the case. In our experiments, we avoid using amplitudes larger than 10 nm and our magnet is typically 4 μm in diameter. Unfortunately, a force measurement requires a larger B_1 field to manipulate spins quickly enough (see chapter 8).

3.4 T_1 requirements of spins

The spin lattice relaxation time (T_1) sets the time in which the spin returns to its equilibrium value with lowest energy, limiting the detection bandwidth. Therefore, the signal to noise ratio of an MRFM measurement may also depend on the relaxation time of the spins. For saturation experiments in which the frequency shift is measured, a large bandwidth is required when materials with short T_1 times are investigated. As visible in figure 3.1, the noise increases at higher modulation frequencies. Although more averages can be applied for shorter T_1 , this reduces the noise only by the square root of the number of measurements. The signal may also be masked by spurious cross-talk signals, appearing during B_1 pulses. The recovery time of the signal may then take longer than the relaxation time of the spins. In the case of the experiment on copper as described in chapter 7, relaxation times below 100 ms would be very challenging to measure. On the other hand, when the relaxation time is very long (more than 100 sec), 1/f noise and the required patience may be limiting.

3.5 RF wire: dissipation

In chapter 8 we discuss adiabatic rapid passage, which is a method to flip a spin in an efficient way in inhomogeneous B_1 fields. In order to apply adiabatic rapid passage to

nuclear spins, sufficient radio frequent oscillating magnetic fields (B_1 fields) need to be generated. These need to be in the order of 4 mT, because the adiabatic condition has to be fulfilled, see chapter 8:

$$\frac{(\gamma B_1)^2}{\omega_a A} \gg 1 \quad (3.21)$$

Where $\omega_a = 2\pi/T_p$ is the angular pulse frequency, with T_p the pulse length, A is the modulation frequency amplitude around the larmor frequency and γ is the gyromagnetic ratio. For cyclic adiabatic cantilever driving, usually the angular pulse frequency equals two times the angular eigenfrequency ω_0 of the cantilever ($\omega_a = 2\omega_0$).

The difficulty with MRFM at millikelvin temperatures is to generate these B_1 fields (or RF fields) while minimizing the dissipation by the RF source, because cooling powers at very low temperatures (10 mK) are limited to approximately 1 μW at the mixing chamber and to even smaller values at the sample. By using a micro wire with high current-densities, one can minimize the dissipation. As a reference, the use of a copper micro wire to produce a B_1 field of 4 mT (M. Poggio et. al.) results in 350 μW power dissipation at 300 mK temperature at the mixing chamber of a dilution refrigerator [30]. The temperature at the sample is likely to be higher, since the RF-source is located closer to the sample than to the mixing chamber.

In order to even further lower the dissipation, we used a superconducting RF micro wire. The design of the micro wire together with sample and detection circuit is shown in figures 2.6 and 2.9. We used niobium titanium nitride (NbTiN) as superconducting material, since this material is known to have a large bandgap and very low dissipation at high frequencies in the sub-mm range [46]. We studied the dissipation mechanisms for alternating currents in a NbTiN superconductor. A detailed explanation of the experiments and the dissipation mechanisms is described in the Master thesis of K.M. Bastiaans [31]. In this study, a similar sample as shown in figure 2.9 was used, in which the critical current of the RF wire was measured to be 18 mA. Consequently, using the Biot-Savart-law, a constant magnetic field of 4 mT at 1 μm distance can be generated. Despite the large DC current and constant magnetic fields, the dissipation turned out to be significant already at 100 kHz and increasing at higher frequencies. The dissipation as well at low temperatures (10-100 mK) as at higher temperatures (4K) showed a quadratic behavior as a function of frequency. Similarly, a quadratic dissipative behavior was seen as a function of current. Three possible reasons for this dissipation mechanism were proposed; dissipation through quasiparticles, vortex dynamics, and dielectric losses in the substrate [31, p. 9-19]. Using the Usadel equations, an estimate of the quasiparticle density of states could be made at different temperatures for the NbTiN micro wire. This shows, despite a quadratic frequency behavior, that no (or negligible) quasiparticles are formed at 10-100 mK temperatures. The dissipation due to dielectric losses would show a linear frequency dependence, leaving dissipation through vortex dynamics. For large current densities, the Lorentz-force for vortices may be larger than the pinning force of the vortices, causing movement (depinning) of vortices. As a consequence, a dissipation channel is created. Another dissipation channel could be created by vortex oscillations in the potential well of a pinning site due to the oscillating current. In contrast with a quadratic behavior of the former, the latter shows a linear dissipa-

tion as a function of frequency. Therefore, in conclusion, the most feasible dominant dissipation channel in this superconductor (NbTiN) is the depinning of vortices [31, p. 37]. The measurements show that a dissipation of 150 nW is generated at a current of 2 mA at a frequency of 100 kHz.

3.6 NbTiN RF wire: reduced repulsion

The RF wire and the pick-up coil are superconducting. Due to the Meissner effect, supercurrents which counteract the magnetic field from the magnetic particle, are created. As a result, the magnetic particle on the cantilever is repelled. However, in a superconductor, the magnetic field can only penetrate until a certain depth, called the penetration depth. This repelling force decreases for larger penetration depths, especially if the size of the superconducting structures approaches this depth. This is the case for the superconducting NbTiN pick-up coil and RF wire as shown in figure 2.9. The wire dimensions are $0.3 \mu\text{m} \times 2 \mu\text{m}$ for the RF wire and $0.3 \mu\text{m} \times 1 \mu\text{m}$ for the pick-up coil, while the penetration depth for the NbTiN film is measured to be 280-300 nm and. Because of this large penetration depth (also called London penetration depth), we would expect less repulsion from the NbTiN superconductor.

To show this experimentally, the frequency shift at $8.5 \mu\text{m} \pm 0.5 \mu\text{m}$ distance from the surface as a function of x position above the pick-up coil is shown in figure 3.3. In addition, a simulation, assuming no penetration depth, is shown in the same figure. This simulation is also used in the thesis of G. Wijts, in which it fits the data of a magnetic particle above a niobium superconductor well [26, p. 49-56]. The position path is shown in the inset of the figure.

We indeed see that the repulsion above the NbTiN superconductor is significantly less (more than a factor four) than in a type I superconductor with small penetration depths. The uncertainty in the simulation, represented by solid gray lines from the upper and lower limit in figure 3.3, is due to the uncertainty in film-thickness. This thickness has been influenced by the etching procedure, where after observing a short in the circuit an extra over-etching time corresponding to 20% of the total RIE etch time was set. The film thickness before etching was 378 nm, which would be reduced to 300 nm with 20% over-etch time. A possible further reduction in size may be present from a faster etching speed of small, micrometer structures. Therefore to be in a safe limit, the gray lines in figure 3.3 restrict the thickness between 150 nm and 350 nm. The blue line corresponds to 250 nm thickness. In future, the thickness could be measured by atomic force microscopy (AFM). One also has to take care that at small distances between the superconducting wire and the magnetic particle, the first critical field at 8mT for NbTiN is passed, allowing vortices to enter, which complicates the interpretation. These vortices may also lower the quality factor of the cantilever. This is not an issue for the measurements shown in figure 3.3, because the magnetic field from the magnetic particle at $8.5 \mu\text{m}$ distance is 3-5 mT.

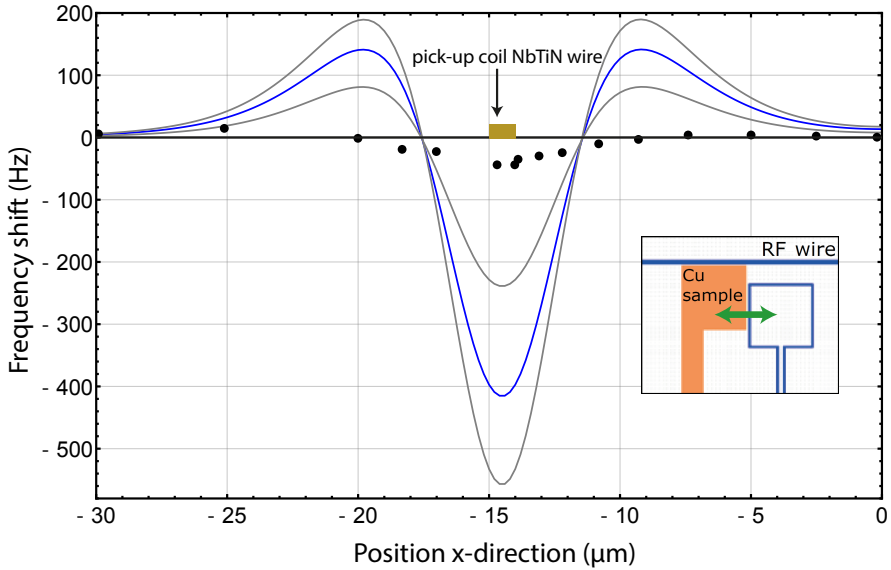


Figure 3.3: Repulsion of the magnetic particle on the cantilever due to the superconducting pick-up coil wire at a distance of $8.5 \mu\text{m} \pm 0.5 \mu\text{m}$. The black dots represent the data and the blue and gray curves represent the simulation. We find that the repulsion is at least four times lower than a calculation which indicates that the large London penetration depth of NbTiN $\lambda = 280 - 300 \text{ nm}$ significantly reduces the magnet. The gray lines form an upper and lower bound for the simulated repulsion, calculated with two different film thicknesses (150 nm and 350 nm). This uncertainty in film thickness is due to the etching procedure. The blue line represents the intermediate simulation, which corresponds to 250 nm thickness.

Chapter 4

Probing the magnetic moment of FePt micromagnets prepared by Focused Ion Beam milling

This chapter has been published as: H. C. Overweg, A. M. J. den Haan, H. J. Eerkens, P. F. A. Alkemade, A. L. La Rooij, R. J. C. Spreeuw, L. Bossoni, and T. H. Oosterkamp. Probing the magnetic moment of fept micromagnets prepared by focused ion beam milling. *Applied Physics Letters*, 107(7), 2015.

We investigate the degradation of the magnetic moment of a 300 nm thick FePt film induced by Focused Ion Beam (FIB) milling. A $1\ \mu\text{m} \times 8\ \mu\text{m}$ rod is milled out of a film by a FIB process and is attached to a cantilever by electron beam induced deposition. Its magnetic moment is determined by frequency-shift cantilever magnetometry. We find that the magnetic moment of the rod is $\mu = 1.1 \pm 0.1 \times 10^{-12} \text{Am}^2$, which implies that 70 % of the magnetic moment is preserved during the FIB milling process. This result has important implications for atom trapping and magnetic resonance force microscopy (MRFM), that are addressed in this chapter.

4.1 Introduction

The fabrication and characterization of micron sized permanent magnets is necessary for a broad range of applications, such as magnetic tweezers, [47, 48] magnetic imaging, [1, 49] and atom trapping with chips [50].

These chips are planar structures that generate magnetic fields, which are widely used to control ultra-cold atoms [51]. The incorporation of permanent magnets in atom chips offers several advantages over the use of current carrying wires: [50, 52] they dissipate no heat and allow more complex trap shapes. Moreover, permanent

magnets can create larger field gradients, which facilitates tighter confinement of atoms, [53] resulting in shorter time scales in trapping experiments. This does require the magnets to be patterned on small length scales. One of the materials currently under investigation is FePt in its $L1_0$ phase, a corrosion resistant material with high magnetocrystalline anisotropy [53, 54, 55]. FePt atom traps that are currently in use are made by optical lithography and plasma etching [55, 56]. The currently used patterns have length scales on the order of $10 \mu\text{m}$ [57].

Micron sized magnets can also be used as a field gradient source for magnetic resonance force microscopy (MRFM) [1]. This is a technique that uses a small magnet mounted on an ultrasoft cantilever to measure the magnetic interaction with spins in a sample underneath the cantilever. It thereby combines the advantage of elemental specificity of conventional Magnetic Resonance Imaging (MRI) techniques with the local and very sensitive probing techniques of Atomic Force Microscopy (AFM) [2, 58]. Required properties for MRFM magnets are high magnetocrystalline anisotropy and a large remanent field [59]. Small dimensions of the magnet are beneficial too, as they result in large magnetic field gradients, which increase the sensitivity of measurements [60, 30]. These requirements are similar to the requirements for atom traps and are all fulfilled by the aforementioned FePt.

One of the techniques to pattern FePt films is to use a Focused Ion Beam (FIB). However, FIB milling can damage the film, possibly degrading the magnetic properties. Examples of such damage include implantation of ions and other ion beam induced alterations to the crystal structure [61, 62]. Determining the magnetic moment after FIB exposure is crucial for applications in both atom trapping and MRFM experiments.

In this chapter, the damage caused by FIB milling on an FePt film is quantified by measuring the magnetic moment of a micron sized rod, which has been milled out of the film, and comparing it to the expected magnetic moment calculated from its volume and its remanent field. The rod is attached to a cantilever and its magnetic moment is determined by cantilever magnetometry, a sensitive technique to determine small magnetic moments [59, 63]. We demonstrate that FIB milling is a suitable way to shape magnetic films for atom trapping experiments and to prepare probes for MRFM.

4.2 Fabrication

The $300 \pm 10\text{nm}$ thick FePt film has been made at the Almaden Research Center of Hitachi. Films of FePt have been sputtered on a Si substrate with a thin RuAl underlayer and a Pt interlayer at a temperature of 400°C . This growth process leads to FePt in its $L1_0$ phase, which has a particularly high out-of-plane magnetization [64].

As a first step to create rods, an indentation in the edge of the film is made with a FIB (Ga^+ -ions, 30 keV, 7 nA ion current, Strata 235 Dual Beam from FEI). The edge is then crenelated (Fig. 4.1(a)) (ion current 500 pA) and rods are created in the sides of the crenels (figure 4.1(b)). The dimension of the rods is $8.1 \mu\text{m}$ in length, $1 \mu\text{m}$ in width and $1 \mu\text{m}$ in height (consisting of 300 nm FePt and 700 nm substrate). The

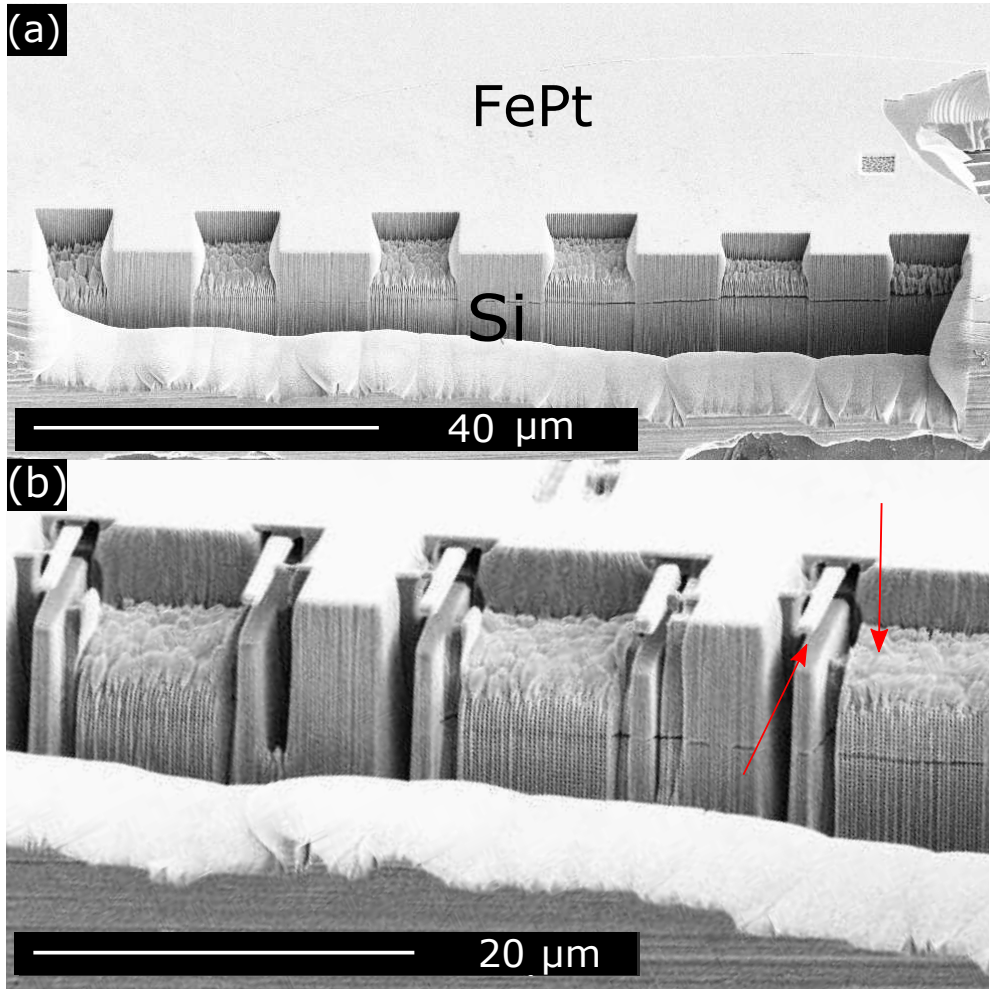


Figure 4.1: Fabrication of rods at the edge of an FePt film sputtered on a Si wafer: (a) crenelation of the edge (b) five rods at the end of the FIB process. The material has been milled from two perpendicular directions, see arrows.

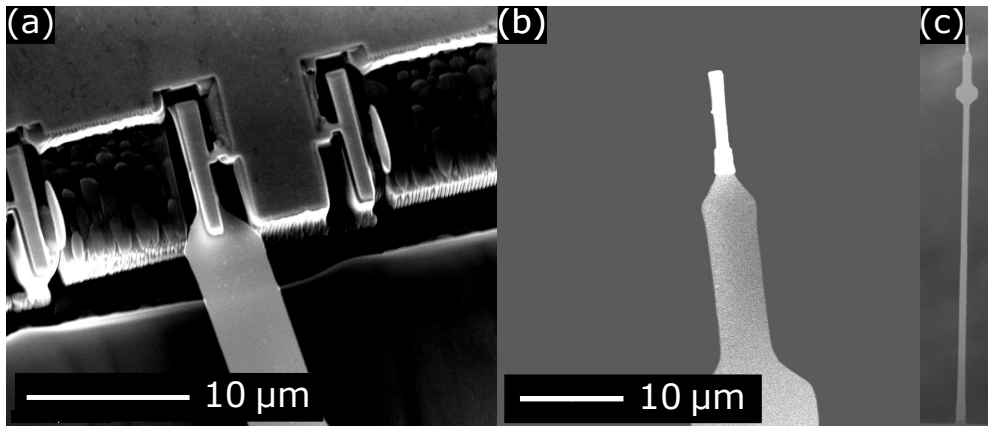


Figure 4.2: Fixation of a rod to a cantilever: (a) the cantilever is brought in position using a nanomanipulator. After an electron beam induced deposition (EBID) process to fix the rod to the cantilever, the connection to the film is broken by retracting the cantilever (b). The widening on the cantilever works as a mirror for laser interferometry. (c) the cantilever-magnet assembly.

sample is rotated by 90° to remove the material underneath the rods. The geometry facilitates the access necessary to mount a rod onto a cantilever.

The FePt film and a cantilever (a single-crystalline silicon beam [24]) are then placed on two stages of an in-house developed nanomanipulator [65] inside a Scanning Electron Microscope (NanoSEM 200 from FEI, USA). Using the nanomanipulator, we bring the cantilever in contact with an FePt rod (figure 4.2(a)). Subsequently, fixation is achieved by an electron beam induced deposition process with $\text{Pt}(\text{PF}_3)_4$ as a precursor gas. The last connection between the rod and the film is broken by suddenly retracting the cantilever. The finished assembly of the cantilever and the rod is shown in figure 4.2(b) and 4.2(c).

4.3 Characterization

Prior to the fabrication of the rods, the magnetization loop has been measured for a film of size $3 \text{ mm} \times 3 \text{ mm} \times 300 \text{ nm}$ in a SQUID magnetometer (Quantum Design MPMS-5S). The measurement has been performed at room temperature in two different geometries (figure 4.3): with an in-plane and an out-of-plane external field \mathbf{H} . The remanent magnetization is $\mu_0 M = 0.76 \pm 0.03 \text{ T}$ for the out-of-plane geometry, while it is $\mu_0 M = 0.50 \pm 0.03 \text{ T}$ for the in-plane geometry. In figure 4.3, the remanent magnetic moment shows negligible dependence on the external magnetic field. This is expected for FePt, as the coercivity increases when the lateral size decreases [66]. Therefore, the external field used in the cantilever magnetometry experiment should not affect the magnetic moment of the rod.

The rods are magnetized in a 3 T field at room temperature along the out-of-plane direction (i.e. along the direction of motion of the cantilever), to achieve a higher remanent field.

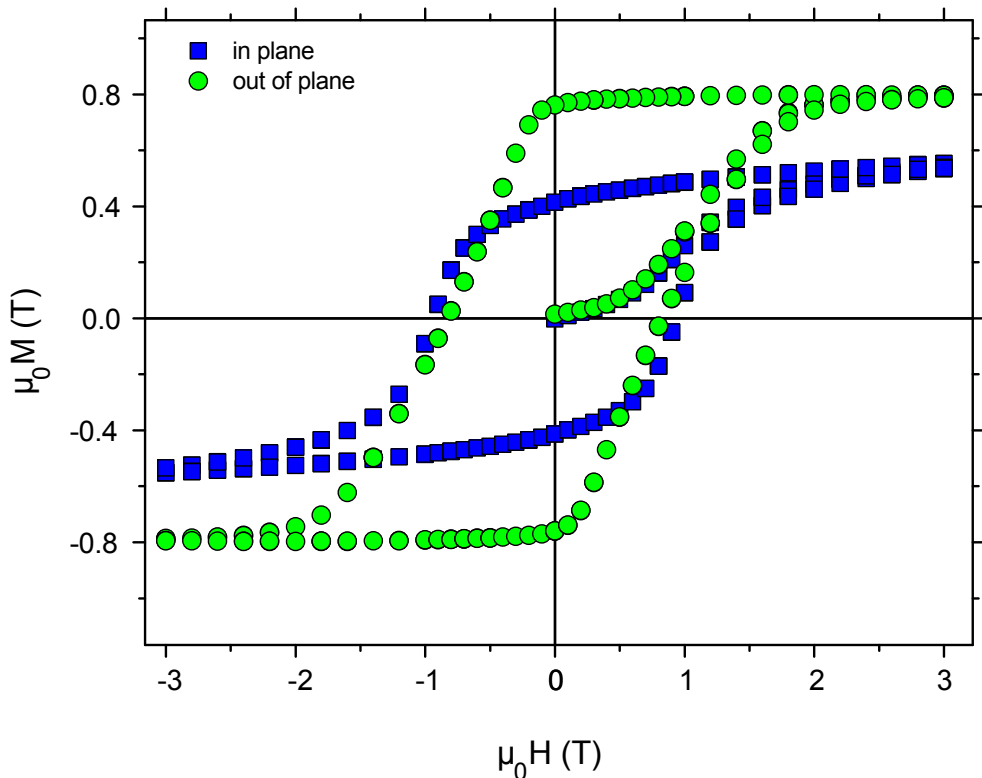


Figure 4.3: Magnetization of the film as a function of external magnetic field strength for two different orientations of the sample. For the out-of-plane orientation the remanent field $\mu_0 M = 0.76 \pm 0.03$ T and for the in-plane orientation it is $\mu_0 M = 0.50 \pm 0.03$ T.

Subsequently, dynamic-mode cantilever magnetometry is performed at room temperature at a pressure of 10^{-5} mbar. The external magnetic field is provided by a Helmholtz coil of approximately 300 turns, generating magnetic fields up to 2 mT. The external magnetic field points along the direction of motion of the cantilever. To determine the magnetic moment μ of the rod, the resonance frequency is measured as a function of magnetic field strength. A fiber optic interferometer working at a wavelength of 1550 nm is used to detect the cantilever motion. The resonance frequency is determined by fitting the thermal motion of the cantilever's fundamental mode to a Lorentzian curve. A ring-down measurement, shown in figure 4.4(b), provides a more accurate measure of the quality factor Q .

The resonance frequency as a function of magnetic field is shown in figure 4.4(a). For the low magnetic field regime, the frequency shift Δf as a function of magnetic field \mathbf{H} is given by:[29]

$$\Delta f = \frac{f_0}{2k} \left(\frac{\alpha}{l} \right)^2 \mu \mu_0 H \quad (4.1)$$

where f_0 is the resonance frequency in the absence of a magnetic field, $l = 200 \mu\text{m}$ is the length of the cantilever, $\alpha = 1.377$ is a constant factor derived for beam can-

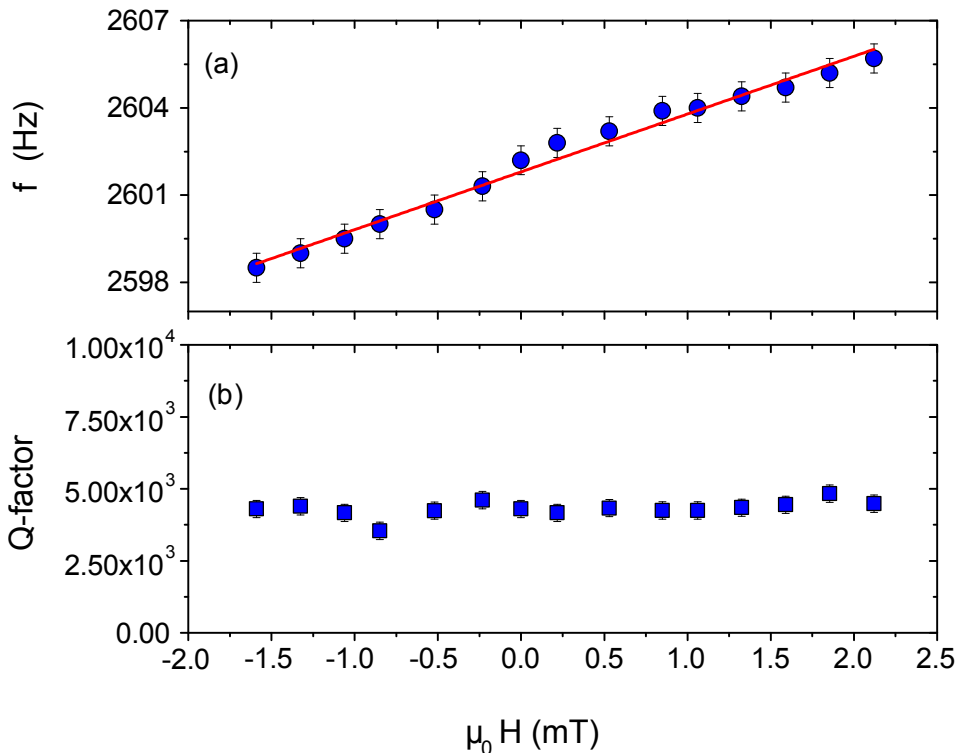


Figure 4.4: (a) Resonance frequency as a function of the external magnetic field determined from the cantilever's thermal spectrum. The slope of the curve implies a magnetic moment of $1.1 \pm 0.1 \times 10^{-12} \text{ Am}^2$, which means a volume of $0.8 \pm 0.1 \mu\text{m}^3$ has been damaged by the FIB. (b) The quality factor as a function of the external magnetic field as determined by a ring-down measurement.

tilevers, and $k = 3.3 \pm 0.2 \times 10^{-5} \text{ N/m}$ is the stiffness of the cantilever, determined by the added-mass method [67].

Making use of equation 4.1, the magnetic moment of the cantilever is deduced to be $\mu = 1.1 \pm 0.1 \times 10^{-12} \text{ Am}^2$. Given the remanent magnetization of the FePt film and the volume of the magnet of $(1.00 \pm 0.02) \mu\text{m} \times (8.10 \pm 0.02) \mu\text{m} \times (0.30 \pm 0.01) \mu\text{m}$, we would have expected a magnetic moment of $\mu = 1.5 \pm 0.1 \times 10^{-12} \text{ Am}^2$, if the magnet had been unaffected by the FIB process. The comparison shows that roughly 60 to 80 % of the magnetic moment is preserved during the FIB process. As both SQUID magnetometry and cantilever magnetometry allow only for the determination of the overall magnetic moment, we cannot precisely determine the damage profile.

The quality factor seems not to depend on the magnetic field strength. Ng et al. [68] did report on a decrease of the quality factor in a magnetic field ranging up to 6 T. This change is negligible in the 2 mT magnetic field range we studied.

More FePt magnets have been attached to cantilevers by the procedure described above. However, the orientation of the out-of-plane direction of the FePt film with respect to the direction of motion of these cantilevers was different. Though benefi-

cial for MRFM experiments, [29] these probes are unfit for cantilever magnetometry experiments.

4.4 Discussion

We believe MRFM would benefit from the described force sensor. Since the force exerted by a spin in the sample on the cantilever is proportional to the gradient of the magnetic field, it is beneficial to use small magnets. In our previous work, we employed NdFeB spheres with a diameter of $3\ \mu\text{m}$ [17]. The field gradient cannot be increased by using smaller NdFeB particles, because they seem to lose their magnetization when scaled down further [69]. Even though FePt has a remanant magnetization which is roughly half as large as that of NdFeB, the possibility to create smaller magnets is promising for the sensitivity of MRFM experiments. The larger magnetic field gradient is not the only improvement that small FePt magnets would yield. It has been observed that the quality factor of MRFM cantilevers can drop drastically when approaching the sample surface [20]. This is most likely due to a dissipative interaction of spins in the sample with the magnet. A smaller magnet interacts with fewer spins and therefore suffers less from this unwanted damping. A forthcoming experiment will enable us to quantify the improvement in the resolution provided by the FePt rods.

Concerning atom trapping, the factor limiting the resolution of FePt traps created by optical lithography and plasma etching is the redeposition of the etched material, the magnetic properties of which are unknown [70]. SEM images show that this redeposition can be of the order of several hundreds of nanometers. From SEM images made after FIB milling, we conclude that for the FePt rods described in this paper redeposition of FePt is negligible compared to the loss of magnetic volume caused by the FIB milling process. Furthermore, the damage induced can possibly be reduced by using a helium FIB. Hence FIB milled patterns could have an advantage over patterns created by optical lithography and plasma etching, when aiming for trap sizes on the order of a micrometer [71, 72]. For the formation of such traps a better understanding of the shape of the damaged region of magnetic films would be needed. FIB milling of FePt will probably not suffice to go to an atom trap scale of the order of 100 nm. Electron beam lithography is the most suitable technique when aiming for submicrometer sizes [71]. This method is currently used in various groups.

4.5 Conclusion

We have shown a fabrication process for micrometer size FePt magnets by FIB milling and a way to attach these magnets to ultrasoft cantilevers by electron beam induced deposition. This technique could in principle be used for any magnetic film. From cantilever magnetometry measurements we conclude that 60 to 80 % of the magnetic moment is preserved during the FIB milling process. FIB milled magnets could therefore be used in atomic trapping experiments when aiming for a trap size on the order of a micrometer. The magnet attached to the cantilever can be used as a

probe in MRFM experiments. The small dimensions of the magnet are expected to improve the sensitivity of MRFM.

Chapter 5

Atomic resolution scanning tunneling microscopy in a cryogen free dilution refrigerator at 15 mK

This chapter has been published as: A. M. J. Den Haan, G. H. C. J. Wijts, F. Galli, O. Usenko, G. J. C. Van Baarle, D. J. Van Der Zalm, and T. H. Oosterkamp. Atomic resolution scanning tunneling microscopy in a cryogen free dilution refrigerator at 15 mK. *Rev. Sci. Instrum.*, 85(3):035112, 2014.

Pulse tube refrigerators are becoming more common, because they are cost efficient and demand less handling than conventional (wet) refrigerators. However, a downside of a pulse tube system is the vibration level at the cold-head, which is in most designs several micrometers. We implemented vibration isolation techniques which significantly reduced vibration levels at the experiment. These optimizations were necessary for the vibration sensitive Magnetic Resonance Force Microscopy experiments (MRFM) at millikelvin temperatures for which the cryostat is intended. With these modifications we show atomic resolution STM on graphite. This is promising for scanning probe microscopy applications at very low temperatures.

5.1 Introduction

Pulse tube (PT) refrigerators have become the standard for many low temperature applications [73]. The main advantages of a PT-cooler are the significant reduction of labor intensity of precooling the dilution refrigerator or experiment as compared to cryogen cooled (dilution) refrigerators, where helium needs to be refilled regularly. These liquid helium transfers from storage dewar to experimental dewar often require that the running experiments are interrupted. This is in particular the case for very

sensitive techniques, like scanning probes. In addition, considering the steep global increase of helium scarcity [74], running the pulse tube is much less costly and does not depend on the quality or quantity of the helium supply.

Even though PT refrigerator systems become more available, most of the low temperature vibration sensitive measurements like low temperature atomic force microscopy (AFM) and scanning tunneling microscopy (STM) are still performed in conventional (wet) (dilution) refrigerators [75, 76, 77, 78]. The reason is that the pulse tube relies on a varying pressure between 7 and 22 bars [79, 80], resulting on the one hand in square wave-like, low frequency, kilonewton forces acting on the top parts of the cryostat, and on the other hand in kilohertz range acoustical vibrations due to the gas flow through the pulse tube regenerator and the flexible hoses connected to the rotary valve and expansion vessels. Recently, a vibration level of 2 nm in a bandwidth of 1 Hz to 1 kHz was reported in a cryogen free dilution refrigerator which was intended for scanning gate microscopy applications [81]. For scanning probe microscopy applications on the atomic scale, the vibration level has to be lower than 1 angstrom.

This paper describes vibration isolation techniques as well as STM measurements in a commercially available cryogen free dilution refrigerator [82, 83] (cryostat). The cryostat has a base temperature of less than 10 mK and a specified cooling power of 650 μ W at 120 mK, which translates to 5 μ W at 10 mK [84]. The vibration isolation is optimized for ultra-sensitive SQUID-based magnetic resonance force microscopy (MRFM) experiments [20]. To test the performance of the vibration isolation, we replaced the MRFM-setup with an STM-setup. To our knowledge, we show for the first time atomic resolution STM in a pulse tube cooled (cryogen free) dilution refrigerator.

5.2 Vibration isolation of the cryostat

In Fig. 5.1, various modifications [26, p. 32-39] to the factory default setup are shown that will be discussed in this paragraph.

The pressure variation in the pulse-tube (PT) is realized though a rotary valve that switches the PT-inlet between the 7 and 22 bar outputs of a compressor at a frequency of 1.4 Hz. In order to reduce the horizontal forces acting on the cryostat, we have lengthened the hose which connects the PT and the rotary valve, implementing a flexible “swan-neck” shape, and placed the rotary valve on a flexible platform inside an acoustic isolation box. The hoses between the rotary valve and the compressor are loosely suspended with ropes from the ceiling of an adjacent hallway. In this way, the expansion of the hose between PT and rotary valve results in an acceleration of the rotary valve and the hoses to the compressor, rather than that of the PT head [26].

In the default configuration, the PT is rigidly connected to the plates at the room temperature-, 50 K-, and 3 K- stages. The periodic expansion of the PT due to the pressure variations is reported to be 25 μ m [85]. In order to reduce the forces acting between the top three cryostat stages, caused by this expansion, we have lifted the PT a few cm, so that it is resting on support rods and a rubber ring on the room temperature plate. The PT is thermalized to the 50 K and 3 K stages with soft copper braids [26].

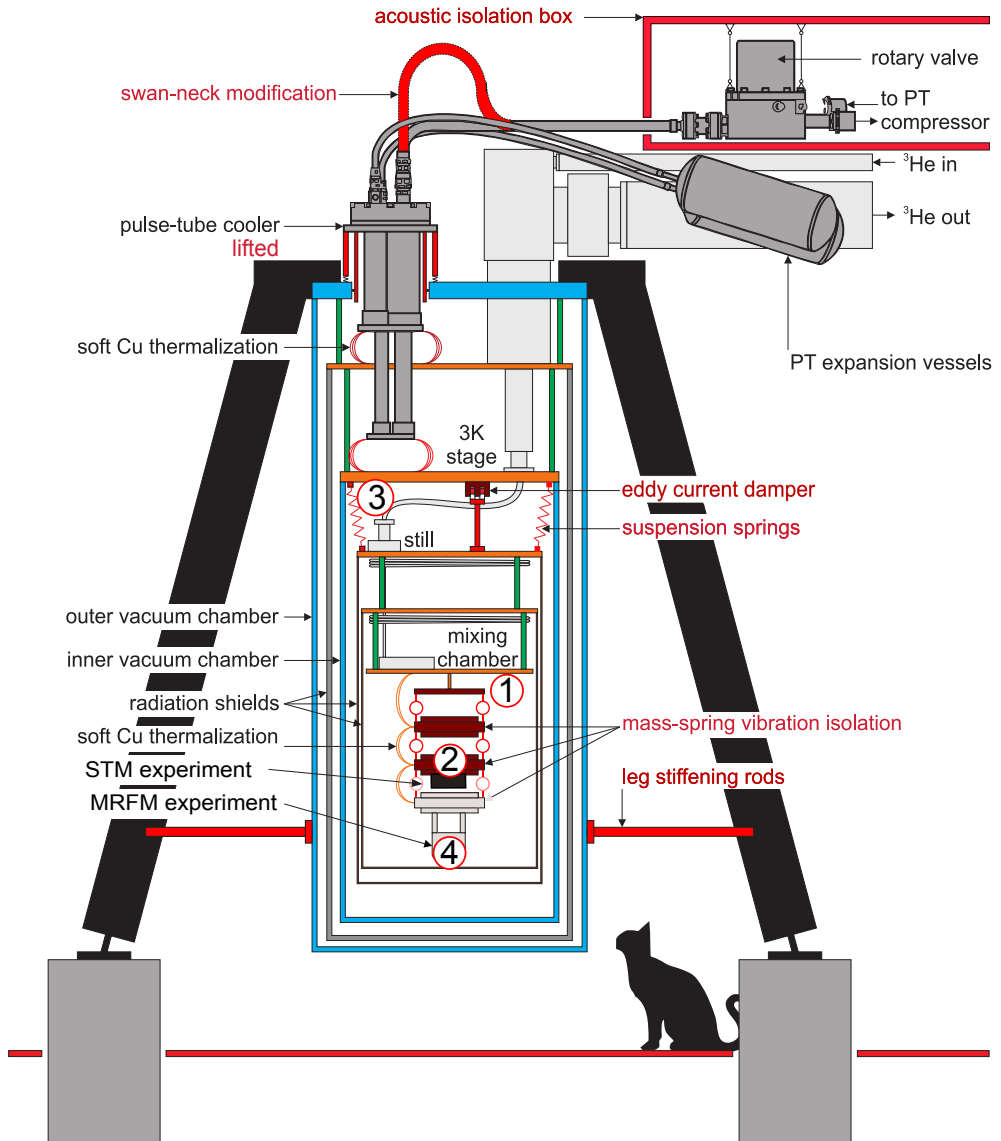


Figure 5.1: Schematic representation of the commercial cryogen-free dilution refrigerator [82] with the implementation of vibration-reducing modifications, which are indicated by a red color. The various vibration measurements are performed at the positions indicated by the numbers 1 to 4 inside the red circles. Position 1: SQUID at the mixing chamber plate. Position 2: SQUID at the second mass. Position 3: Geophones at the 3 K plate. Position 4: MRFM vibration measurement inside MRFM-setup (aluminum box in the order of $10 \times 10 \times 10$ cm) [26].

The three support legs of the cryostat are placed on a concrete block that is separated from the foundation of the surrounding building. We have stiffened the connection between the legs and the outer vacuum chamber (OVC) by making the leg connection to the room temperature plate more bulky as well as by adding rods between the bottom of the OVC and the legs, thus creating triangular support structures.

The default connection between the 3 K plate and the still plate is provided by rigid poles. We have removed these poles and suspended the lower three stages of the cryostat from the 3 K plate with tension springs [86]. The total mass of the suspended part is 55 kg. We use 5 pairs of springs with a stiffness of 1.31 N/m, which leads to an estimated vertical resonant frequency of 3 Hz. In order to reduce the vibration amplitude at this frequency, which is uncomfortably close to the second harmonic of the PT excitation, we implemented an eddy current damper that is thermalized at the 3 K plate [26].

Furthermore, we added a mass-spring vibration isolation system below the mixing chamber plate, consisting of three 5 kg brass masses, suspended from tool steel ring springs, which was designed to provide a 100 dB vibration isolation in a frequency range between 1 kHz and 5 kHz [87]. The mass-spring vibration isolation is especially suitable for the MRFM cantilevers which have their natural resonance frequencies in this frequency range. The masses are thermalized to the mixing chamber with commercial soft Cu tape, clamped with brass bolts. The MRFM experiments were always mounted on the lowest or second-to-lowest mass of this mass-spring system. In the case of the STM measurement described in section 5.3, the STM setup was mounted on the second mass, removing the third (lowest) mass, since vibration isolation in this frequency range (1 kHz to 5 kHz) is not necessary for STM. In order to measure the vibrations, we used a Superconducting QUantum Interference Device- (SQUID) based readout from our MRFM setup, which measures tiny magnetic flux changes [28]. The signals are resulting from the motion of the detection coil in the ambient magnetic field gradient that exists inside the cryostat [26].

Fig. 5.2a shows the improvement in SQUID noise due to the suspension of the still plate and the implementation of the mass-spring vibration isolation. This was an early modification, before lifting the PT and adding the leg stiffening rods. The red curve in Fig. 5.2a shows the Power Spectral Density (PSD) of the SQUID voltage noise with the SQUID on the mixing chamber plate (position 1 in Fig. 5.1) in the cryostat as delivered (but with the rotary valve suspension and the cryostat placement already as drawn in Fig. 5.1). The black curve was measured with the SQUID on the second suspension mass (position 2 in Fig. 5.1), after implementation of the still suspension (suspension springs and eddy current damper). Although we did not calibrate for a displacement measurement, it becomes clear from the spectra that the suspension systems lead to a tremendous reduction of the vibrations over the whole measurement bandwidth. Above 200 Hz, the noise floor is now determined by the intrinsic detection SQUID flux noise instead of experimental vibrations. Below 10 Hz, the harmonics of the PT modulation ($n \cdot 1.4$ Hz) emerge that were first obscured by low frequency background noise. Taking the square root of the integrated spectra, we obtain the root mean square (rms) output in Volt, which is shown in Fig. 5.2b. The spectra are integrated from 1 Hz to the given bandwidth (horizontal axis). The data below 1 Hz

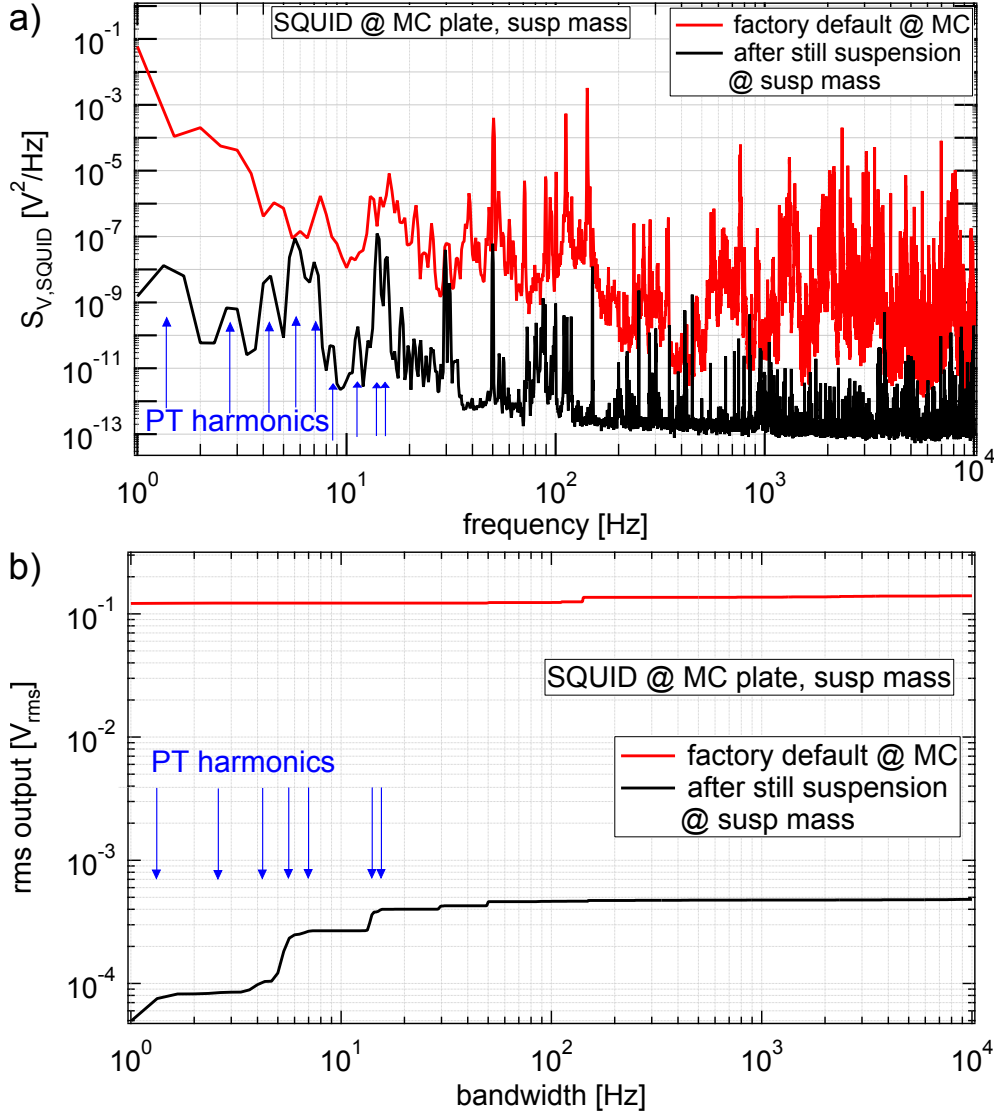


Figure 5.2: Vibration reduction after suspension of the still plate from the 3 K plate and adding a mass-spring system below the mixing chamber. The SQUID vibration measurements were performed at position 1 (factory default) and position 2 (after still suspension) in Fig. 5.1. (a) PSD spectra of the SQUID noise [26] (b) The rms output: $SQUIDoutput_{rms}(\Delta f) = \sqrt{\int_1^{\Delta f} S_V(f) df}$. A significant vibration reduction over the whole spectrum is visible. The low frequency background noise is reduced to such a level that the harmonics of the PT modulation (n·1.4 Hz) appear (peaks in the PSD spectrum and jumps in the integrated spectrum).

is influenced by the DC offset of the SQUID output, which is therefore not integrated. We find a relative improvement of a factor 291 in a bandwidth from 1 Hz to 10 kHz by dividing the last point from the red curve (factory default) by the last point of the black curve (after suspension).

The effect of lifting the PT cooler was quantified by measuring the vibrations at the 3 K plate (position 3 in Fig. 5.1) with rotating-coil geophones [88]. The geophones are calibrated for vertical displacements in a frequency range between 1 Hz and 100 Hz. In Fig. 5.3a we show the PSD of the displacement noise before and after lifting the PT. The vibration peaks at multiples of the PT modulation frequency are clearly reduced up to the 8th harmonic. Taking the square root of the integral of these spectra, we obtain the displacement noise, shown in 5.3b. From this figure, we see that the total root mean square (rms) displacement noise before and after lifting the pulse tube is $1.65 \mu\text{m}$ and $0.71 \mu\text{m}$ respectively. Therefore, the full-bandwidth relative improvement is a factor 2.3 [26]. Considering the 300 times improvement at the mixing chamber plate and the $0.71 \mu\text{m}$ displacement noise at the 3 K plate, we estimate a displacement noise of roughly 3 nm at the second mass (position 1 in Fig. 5.1) after lifting the pulse tube and still suspension.

The latest modification was to add rods between the OVC and the cryostat support legs in order to make the construction stiffer. In the original design, the connection between the support legs and the room temperature plate was quite floppy. The stiff cylindrical OVC connected to this plate acted like a vibration antenna that seemed to resonate with the 3rd harmonic of the PT modulation at 4.2 Hz. If we compare the PSDs of the displacement of a detection coil at the bottom suspension mass, with and without the extra rods, we observe that the peak at 4.2 Hz is reduced by a factor 2.5 (figure not shown) [26]. This increases however some vibrations at some other frequencies, most clearly at 1 Hz and at 342 Hz, but that still results in an improvement of a factor 1.2 when integrated over the whole measurement bandwidth [26].

In Fig 5.4, we have plotted the rms displacement noise of the detection coil with respect to the MRFM setup [17] (position 4 in Fig. 5.1) versus the integration bandwidth after the implementation of all modifications. The total rms displacement noise inside the MRFM setup is only 61 pm, which is more than sufficient to enable atomic-scale imaging. This value depends on the particular chosen setup, corresponding to different mechanical loops.

5.3 STM setup and experimental preparation

For these experiments we used an STM head built in-house similar to other setups used previously at low temperatures [89, 77]. The STM is based on the Pan walker design [75, 90]. The coarse approach motor consists of a hexagonal cross-section prism made of titanium, covered by a hard coating (TiCN). The prism is held by three pairs of shear mode piezoelectric actuators. Two pairs are rigidly glued to the STM body, while the remaining pair is glued to a plate and pressed against the prism with a phosphor-bronze leaf spring. The normal force (and therefore the friction) between the actuators and the prism is regulated by adjusting the spring. The latter will also

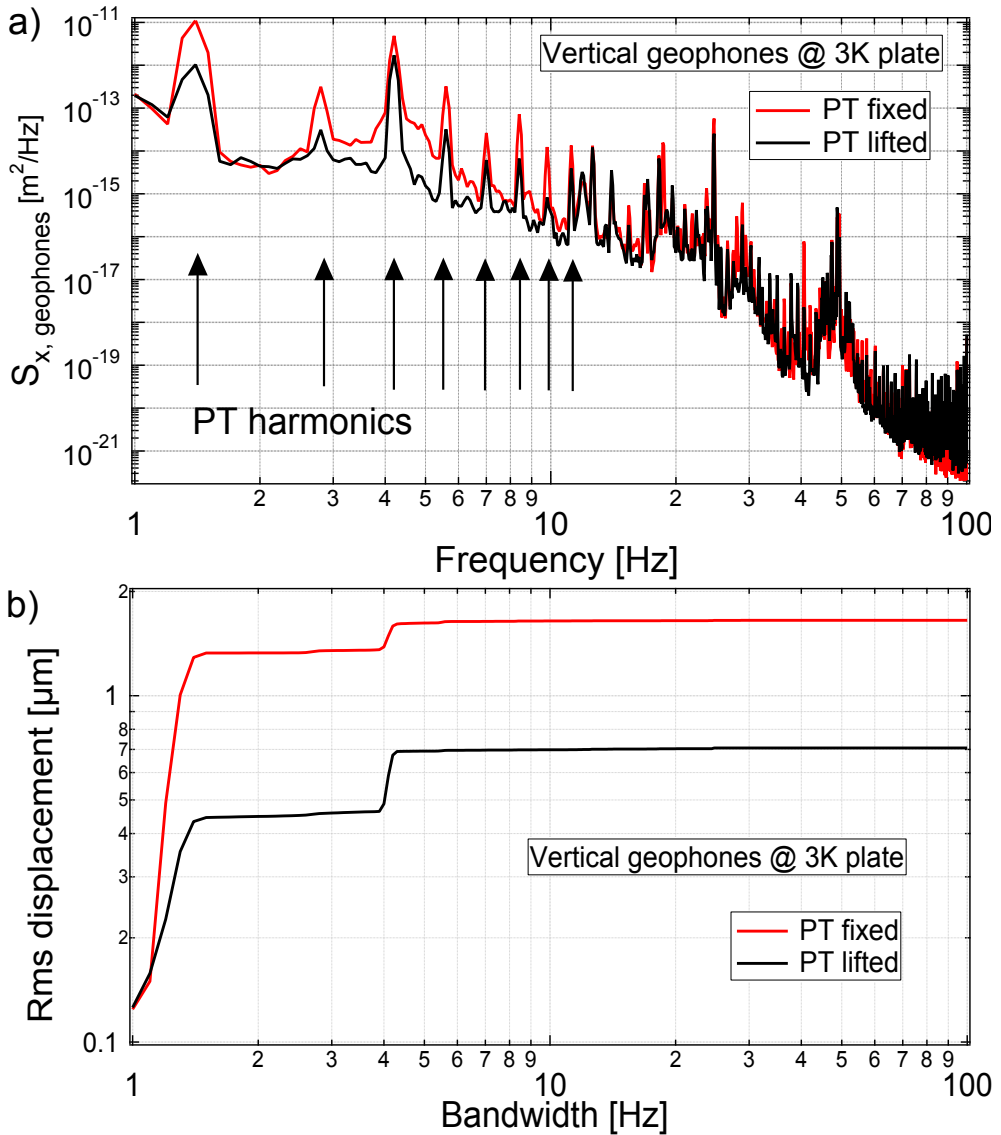


Figure 5.3: Vibration reduction after lifting the pulse-tube cooler [26], measured at position 3 (3 K plate). (a) PSD spectra of geophone signals. (b) The rms displacement noise: $\text{displacement}_{\text{rms}}(\Delta f) = \sqrt{\int_1^{\Delta f} S_x(f) df}$. A significant vibration reduction at the base frequency of the PT (1.4 Hz) is visible. The vibration level at the 3rd harmonic (4.2 Hz) of the PT is less influenced by the lifting.

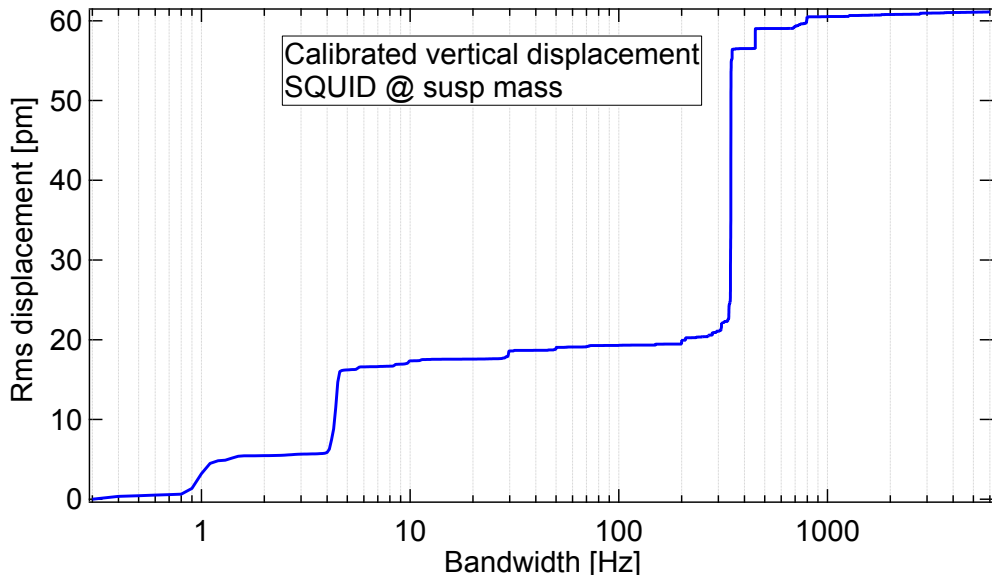


Figure 5.4: Net relative motion of tip versus sample in aluminum box at position 4 (inside the MRFM) after all modifications [26].

provide constant normal force if the size of the STM assembly changes because of thermal shrinkage at low temperatures. The motor is driven by sending de-phased voltage signals to the pairs independently (walker mode) as described in ref.

The scan is performed by XY shear- and Z thickness mode piezoelectric elements with an estimated maximum range of $2\ \mu\text{m} \times 2\ \mu\text{m}$ and 400 nm at low temperatures, respectively [91]. The feedback control and image acquisition are done by Leiden Probe Microscopy [92] control electronics. Images were acquired in constant current- and constant height mode.

For the STM benchmark experiment, we used Highly Ordered Pyrolytic Graphite (HOPG), a standard STM sample for atomic resolution performance tests. The sample was glued on a 1 cm circular copper plate using low temperature compatible silver paint. The copper plate was mounted on an equivalent copper plate, using electrically isolating black Stycast, which served as a ground plate. Graphite was cleaved using scotch tape until a smooth surface was visible with the naked eye. Furthermore, we used a platinum iridium tip, which was cut from a wire under a 45 degree angle. The sample and tip were thermalized to the 10 mK plate by using silver coaxial wiring. The total length of the wire from the tip to the current to voltage converter (gain 10^9) was 3 meter, with a capacitance of 240 pF.

The STM body was thermally anchored at the 2nd mass below the mixing chamber plate (see, Fig. 5.1) in a horizontal direction. In this direction, the STM is less sensitive to the Z (vertical) vibrations, which is the dominant vibration of the cryostat. The masses were thermalized by connecting copper strips to the mixing chamber plate. Furthermore, the sample and tip were thermalized to the mixing chamber plate by using silver coaxial wiring. A cerium magnesium nitrate (CMN) thermometer [93],

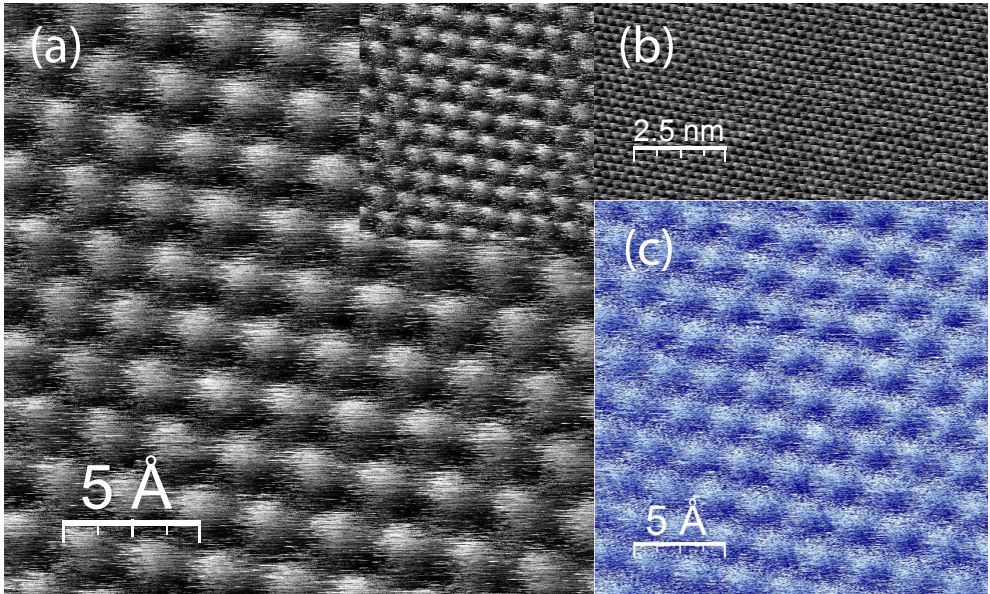


Figure 5.5: (a) constant current STM image (2.14 nm x 2.14 nm), showing atomic resolution on HOPG (left to right scan), the right to left scan image is shown in the inset. Frame time $T_f = 1049$ seconds (1024x1024 pixels), tunneling current $I_c = 400$ pA and bias voltage $V_b = 0.5$ V (b) constant current STM image (10.7 nm x 5.35 nm). $T_f = 262$ seconds (512x256 pixels), $I_c = 400$ pA and $V_b = 0.5$ V. (c) constant height image (2.14 nm x 2.14 nm). $T_f = 262$ seconds (1024 x 1024 pixels), $I_c = 400$ pA and bias voltage $V_b = 0.5$ V.

calibrated to a superconducting fixed point device (SRD1000) [93] was used to monitor the temperature at the mixing chamber plate. Close to the STM-body a carbon thermometer was used to monitor the temperature of the 2nd mass.

5.4 Results

In this section, we show several results, which serve as a benchmark for the vibration isolation of the pulse tube cooled dilution refrigerator described in section 5.2. All data presented in this section is acquired with a running PT, with a temperature of 9 mK at the mixing chamber of the dilution refrigerator and at temperatures below 15 mK at mass 2, close to the STM setup. It is among our future plans to measure the electron temperature by measuring thermal broadening of tunneling spectroscopy with a superconducting tip on a sample in the normal state, to get a precise number for the effective electron temperature in the sample.

Fig. 5.5a and Fig. 5.5b show images in constant current mode. The triangular atomic structure is clearly visible [94], showing that high resolution scanning probe microscopy (SPM) measurements are possible in cryogen free (dilution) refrigerators. The piezo-electric actuators (X, Y and Z) were otherwise not calibrated, but the scale of the atom separation from literature corresponds to the scale derived from the maximum displacement of the X,Y shear piezos at low temperatures. Furthermore,

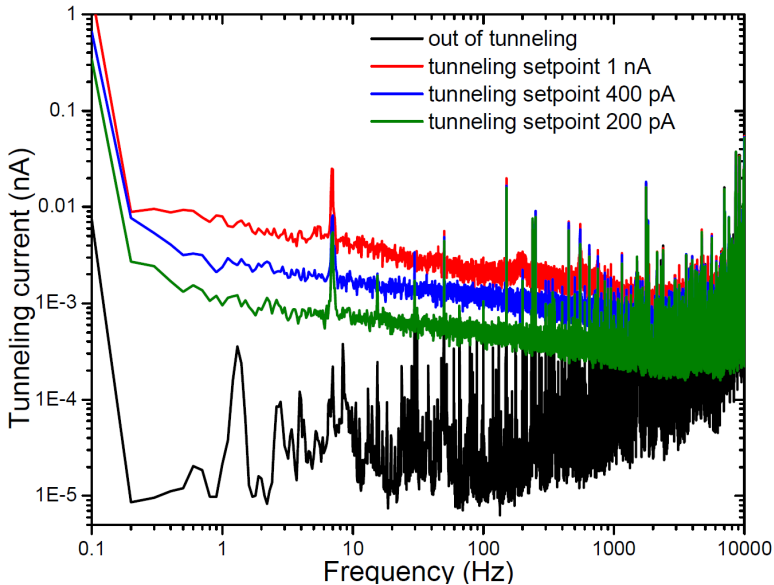


Figure 5.6: Tunnel-spectrum for several tunneling current setpoints. Most of the noise (peaks) visible in the out of tunneling spectrum are due to microphonics.

the image of the left to right scan is the same as the right to left scan (see the inset of Fig. 5.5a).

We also measured at constant height, in which the current variations are measured while the voltage on the Z-piezo is kept constant to a certain extent. In the frozen state, the voltage drifted away from its initial value due to droop in the electronics, but this droop was slow enough to capture at least 2 images in 524 sec. The voltage drift resulted in a tip movement pointing away from the surface. In Fig. 5.5c, an atomic resolution image in constant height mode is shown. This image is a clear demonstration of stable tip surface situation, because present vibrations are not compensated by the feedback system in constant height mode.

In order to monitor the movement of the sample in comparison to the tip (thermal/piezo drift), we took several images in constant current mode of the same spot in 3 hours time, with a frame time of 1049 seconds. The frames of these measurements are compiled into a video, which is available via the supplementary files of the published article [95]. One of the frames is shown in Fig. 5.5a. From the displacement of the last frame compared to the first frame, we find a (X,Y)-drift of less than 1 Å per 3 hours. This small drift and stable tip surface situation is promising for application in Scanning Tunneling Spectroscopy (STS) experiments.

In Fig. 5.6, the spectra of the tunneling current at several tunneling current setpoints are shown in constant height mode. In the spectrum of the out of tunneling signal, several peaks are visible which in part corresponds to the pumps (30 Hz) and the pulse tube (1.4 Hz and higher order). These frequencies couple into the circuit due to microphonics. Using headphones to monitor the output of the current to voltage

converter, the pulse tube, pumps and dilution refrigerator are very audible. Note that the noise level increases when the current setpoint is raised in constant height mode, which is more dominant at lower frequencies. We attribute this effect to the voltage noise of a voltage source, connected to the Z-piezo, resulting in an excess piezo motion of an estimated 10^{-12} m/ $\sqrt{\text{Hz}}$. In all of the spectra, a dominant peak at 6.9 Hz is clearly visible, which is the 5th harmonic of the pulse tube.

5.5 Conclusion

We significantly reduced the vibration level of a commercially available cryogen free pulse tube dilution refrigerator. The results show that future scanning probe microscopy experiments and other vibration sensitive experiments inside a cryogen free PT (dilution) refrigerators have become more accessible. Further vibration isolation will be implemented in the future [96].

Chapter 6

Spin-mediated dissipation and frequency shifts of a cantilever at millikelvin temperatures

This chapter has been published as: A. M. J. den Haan*, J. J. T. Wagenaar*, J. M. de Voogd, G. Koning, and T. H. Oosterkamp. Spin-mediated dissipation and frequency shifts of a cantilever at milliKelvin temperatures. *Phys. Rev. B*, 92:235441, Dec 2015. [97]

*These authors contributed equally

We measure the dissipation and frequency shift of a magnetically coupled cantilever in the vicinity of a silicon chip, down to 25 mK. The dissipation and frequency shift originates from the interaction with the unpaired electrons, associated with the dangling bonds in the native oxide layer of the silicon, which form a two dimensional system of electron spins. We approach the sample with a 3.43 μm -diameter magnetic particle attached to an ultrasoft cantilever, and measure the frequency shift and quality factor as a function of temperature and the distance. Using a recent theoretical analysis [J. M. de Voogd et al., arXiv:1508.07972 (2015)] of the dynamics of a system consisting of a spin and a magnetic resonator, we are able to fit the data and extract the relaxation time $T_1 = 0.20 \pm 0.04$ ms and spin density $\sigma = 0.15 \pm 0.01$ spins per nm^2 . Our analysis shows that at temperatures ≤ 500 mK magnetic dissipation is an important source of non-contact friction.

6.1 Introduction

Understanding the dissipation and frequency shifts in magnetic force experiments is crucial for the development of magnetic imaging techniques, e.g. Magnetic Resonance Force Microscopy (MRFM). The sensitivity of such techniques depends on the friction of the cantilevers, which therefore has increased the interest in high-quality cantilevers with quality factors exceeding a million [16]. However, the quality factor reduces due to non-contact friction with the scanned sample which is explained by dielectric fluctuations [98]. Far from the surface, magnetic dissipation from paramagnetic spins or nanomagnets on the cantilever have been observed to have a large effect on the friction [99, 100]. Our report quantitatively analyzes the magnetic dissipation of a cantilever in the vicinity of a silicon chip, showing that this is the most significant non-contact friction at low temperatures for a magnet on cantilever geometry.

Magnetic Force Microscopy (MFM) measures the forces resulting from stray fields of a sample that is being scanned. The coupling of the tip with the magnetic field manifests itself as a shift in the resonance frequency of the cantilever and as additional dissipation which reduces its quality factor Q . For magnetic moments that do not change due to the magnetic tip itself, the frequency shifts are well understood. However, a more complicated model is required when the spins in the sample are paramagnetic, because the motion of the tip changes the direction of their magnetic moments [101].

In this chapter, we show frequency shifts and dissipation resulting from the dangling electron bonds at the surface of a silicon substrate. We are able to extract the relaxation time T_1 of the electron spins, without using electron spin resonance techniques. Furthermore, we use our analysis to calculate the maximum possible dissipation for a state-of-the-art MRFM setup and diamond cantilever. We show that magnetic dissipation can cause a drop in quality factor, thereby decreasing the sensitivity of an MRFM experiment. We calculate that this dissipation is suppressed when using large external magnetic fields at low temperatures.

6.2 Theory

In our experiment, a magnet attached to a cantilever (Fig. 6.1a) couples via its magnetic field $\mathbf{B}(\mathbf{r})$ to magnetic moments $\boldsymbol{\mu}$ originating from localized electron spins with near-negligible interactions. The coupling with a single spin can be associated with a stiffness k_s , which results in a shift Δf of the natural resonance frequency f_0 of the cantilever, according to $\Delta f = \frac{1}{2} \frac{k_s}{k_0} f_0$, with k_0 the natural stiffness of the cantilever.

Commonly, the analysis of magnetic interaction [27] begins with the interaction energy $E = -\boldsymbol{\mu} \cdot \mathbf{B}(\mathbf{r})$. And one calculates the force and stiffness acting on the cantilever by taking the first and second derivative with respect to x , the direction of the fundamental mode of the cantilever. Assuming that $\boldsymbol{\mu}$ is fixed by a large external field, one obtains in this approach a stiffness in the form of $k_s = \boldsymbol{\mu} \cdot \frac{\partial^2 \mathbf{B}(\mathbf{r})}{\partial x^2}$.

A recent detailed analysis by De Voogd et al. [21], which starts with the Lagrangian of the full system, taking into account the spin's dynamics as well as the

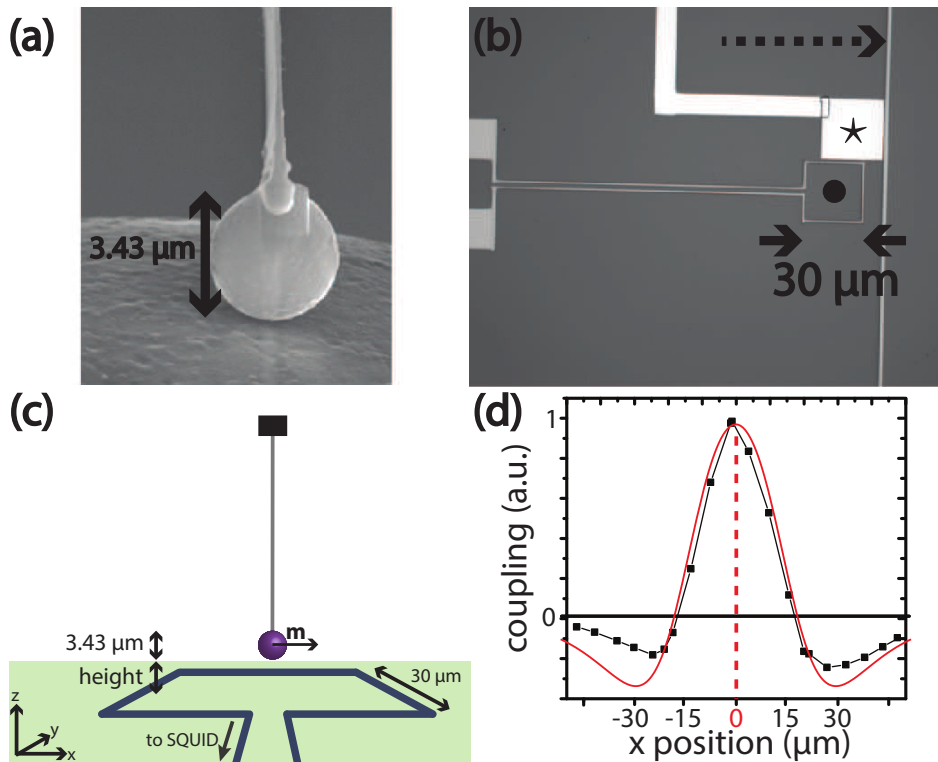


Figure 6.1: (a) Scanning Electron Microscope image of the magnetic particle after it is glued to the cantilever. (b) Optical microscope image of the detection chip. The cantilever is positioned above the center of the pickup coil (\bullet). The pickup coil is used for SQUID based detection of the cantilever's motion. The vertical wire (dotted arrow) and the copper sample (\star) are used in other experiments. (c) Sketch of the setup. The height is measured from the bottom of the magnetic particle, which has a diameter of $3.43 \mu\text{m}$. (d) The coupling with the pickup coil as function of the x-position of the cantilever. The red solid line is the calculated flux change in a square loop due to a magnetic dipole μ on a moving resonator. The maximum (scaled to 1) of the curve is at the center of the pick-up coil, which can be determined with μm precision.

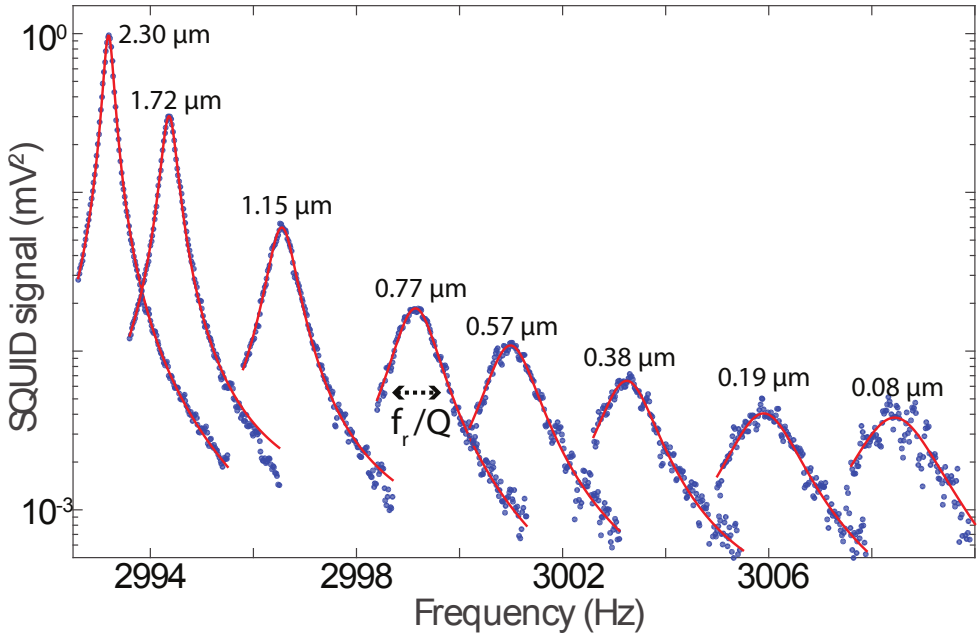


Figure 6.2: Frequency sweeps of the cantilever at a temperature of 70 mK. When moving towards the sample, the resonance frequency f_r increases, while Q decreases due to an increasing coupling with the surface electron spins. We extract f_r and Q by fitting the data to a Lorentzian (red solid line).

influence of the mechanical resonator on the spin, suggests that the commonly employed model is not the correct approach for paramagnetic spins. For paramagnetic spins, the relaxation and the exact dynamics of the spin in the cantilever's magnetic field determine the frequency shifts and dissipation. In the case of a two-dimensional system of paramagnetic spins, uniformly distributed over an infinite surface, the frequency shift Δf and shift in the inverse quality factor $\Delta \frac{1}{Q}$ can be written as:

$$\frac{\Delta f}{f_0} = \frac{1}{2} C \cdot \frac{(2\pi f_0 T_1)^2}{1 + (2\pi f_0 T_1)^2}, \quad (6.1)$$

$$\Delta \frac{1}{Q} = C \cdot \frac{2\pi f_0 T_1}{1 + (2\pi f_0 T_1)^2}, \quad (6.2)$$

$$C = \frac{\sigma \mu^2}{k_0 k_B T} \iint_S \frac{\left(\hat{\mathbf{B}}(\mathbf{r}) \cdot \frac{\partial \mathbf{B}(\mathbf{r})}{\partial x} \right)^2}{\cosh^2 \left(\frac{\mu \mathbf{B}(\mathbf{r})}{k_B T} \right)} d\mathbf{r}. \quad (6.3)$$

Where T is the temperature, k_B is the Boltzmann constant and T_1 is the spin's longitudinal relaxation time. The integral is performed over the infinite surface assuming a constant spin density σ . We have assumed $\Delta f \ll f_0$, $Q \gg 1$, and that the inverse of the transverse relaxation time T_2^{-1} is much smaller than the Larmor frequency, which is already the case when T_2 is larger than 1 μ s.

In this chapter, we detect the dangling bonds that are present on the surface of a silicon substrate of the detection chip using MFM down to 25 mK. We use a commercial cryogen-free dilution refrigerator, in which we implemented several vibration isolation measures [95]. We are able to coarse approach towards the sample in three dimensions, with a range of 1 mm in x, y and z. For this we employ three ‘Piezo-Knobs’, from Janssen Precision Engineering B.V., while reading out the position using three capacitive sensors.

6.3 Experimental setup

The experimental setup and sample fabrication is described in chapter 2, sections 2.2, 2.3, and 2.4. A summary, with the relevant details of the experimental setup and sample fabrication, is written below.

The cantilever is a silicon micro-machined IBM-type with length, width and thickness of 145 μm , 5 μm and 100 nm, respectively [24, 23]. The magnetic particle is a spherical particle from a commercial neodymium-alloy powder ¹. We used platinum electron beam induced deposition using an in-house developed nanomanipulator [65] in a Scanning Electron Microscope (SEM) to attach the small magnetic particle on the free end of the cantilever and measured the diameter to be 3.43 μm (Fig. 6.1a). Subsequently, we magnetized the magnet in the x-direction at room temperature in a field of 5 T.

The substrate is high resistivity ($> 1 \text{ k}\Omega\text{cm}$) (100)-oriented n-type (phosphorus doped) silicon. The substrate is cleaned with acetone and DI water, which leaves an interface of silicon with its native oxide. To create the superconducting structures on the chip, NbTiN is grown on the silicon substrate with a thickness of roughly 300 nm. Patterning is done using standard nano-lithographic techniques and reactive ion etching in a SF_6/O_2 plasma. For the experiment described in chapter 7, we added a wire for radio-frequency currents and a $250 \pm 50 \text{ nm}$ thick copper layer capped with gold. The copper is connected via golden wire bonds to the sample holder, which itself is connected via a silver welded wire to the mixing chamber, ensuring good thermalization of the sample. Figure 6.1b shows an optical microscope image of the obtained structure.

6.4 Methods

We drive the cantilever using a small piezo element glued to the cantilever holder. We sweep the drive frequency using a function generator around the resonance frequency f_r while measuring the SQUID’s response using a Lock-In amplifier. We fitted the square of the SQUID’s signal with a Lorentzian curve in order to extract f_r and Q . The amplitude of the Lorentzian is determined by the coupling between the magnet and the pickup coil, which is proportional to the energy coupling, and can be used to determine the position of the cantilever by scanning the cantilever in the xy-plane, see figure 6.1d.

¹The neodymium-alloy powder is of type MQP-S-11-9-20001-070 by Magnequench, Singapore

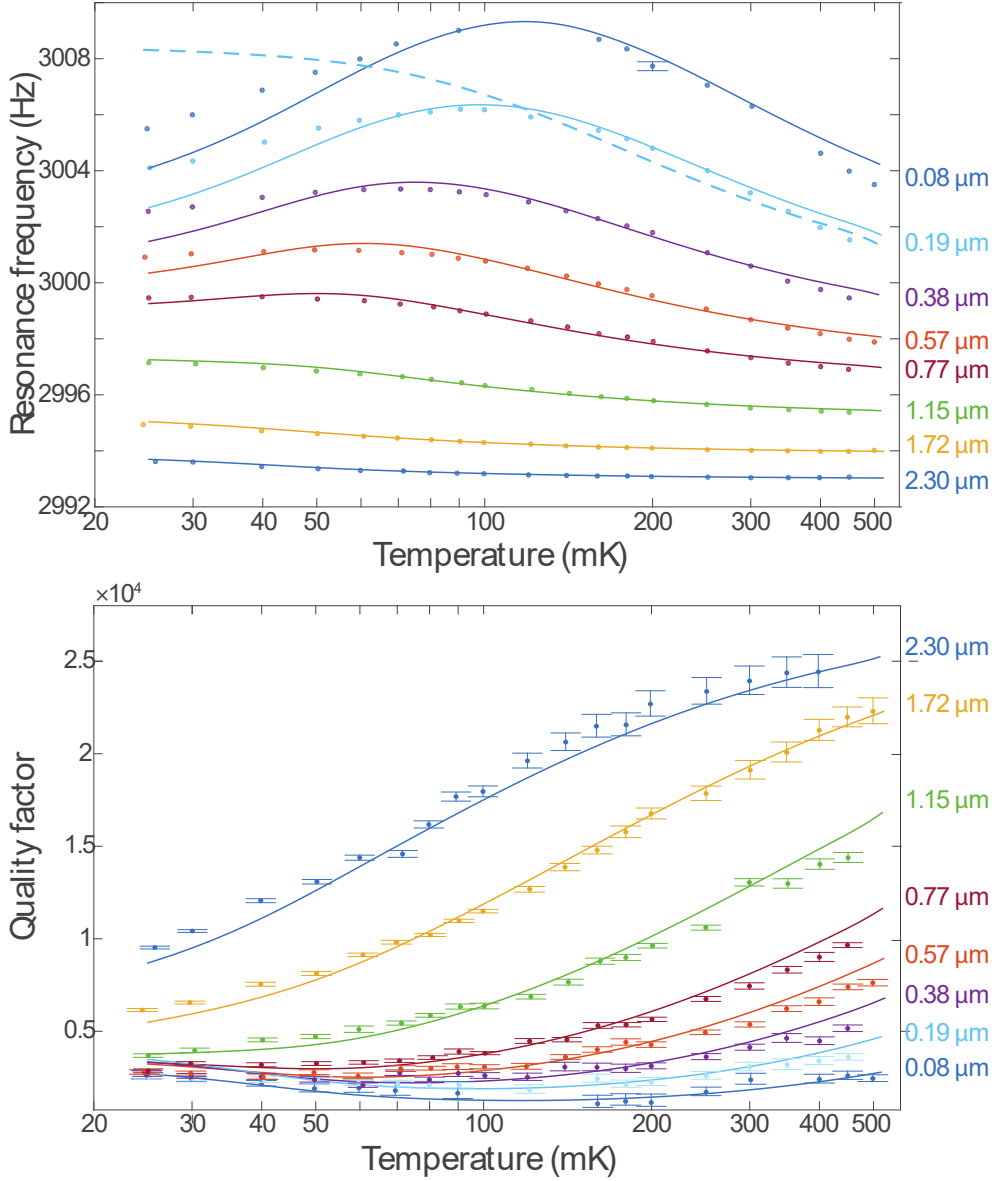


Figure 6.3: Resonance frequency f_r and quality factor Q versus temperature for different heights of the cantilever with respect to the sample. For the quality factor, the error bars indicate the 95 % confidence intervals of the Lorentzian fit. For the frequencies the average error was 0.01 Hz, which is smaller than the point size, except for one data point. The solid lines are fits to the data with the spin density σ , spin relaxation time T_1 and frequency offset f_0 as fitting parameters. f_r and Q are simultaneously fitted for each height. The results of the fit can be found in table 6.1. The dashed line is the frequency shift calculated with the commonly used expression $k_s = p\mu \cdot \frac{d^2 B}{dx^2}$, with $p = \tanh\left(\frac{\mu B(r)}{k_B T}\right)$ and with σ ten times smaller than we find in our analysis.

For the experiment presented in this chapter, we positioned the cantilever above the center of the pickup coil, to minimize possible repulsive forces from the superconducting wires. By gently decreasing the height of the cantilever until the signal is completely lost, we determine the relative height of the magnetic particle with respect to the surface. The sample holder is placed on a finestage, machined out of aluminum, which can be moved in all spatial directions by actuating laminated piezoelectric extension stacks. Using this, we can now have good control of the height up to the full range of the finestage of $2.3 \mu\text{m}^2$.

We swept the drive frequency at a drive amplitude small enough to avoid non-linear responses of the cantilever's motion, while measuring the SQUID signal. We measured with a sampling time of 2 s every 0.02 Hz. Fitting the data with a Lorentzian, we obtain f_r and $Q = \frac{f_r}{FWHM}$. At each height, the temperature was varied from the lowest achievable temperature ≈ 25 mK, up to 500 mK. Above 500 mK, the aluminum shielding of the experiment starts to become non-superconducting. An example of the data with the Lorentzian fits at all used heights at 70 mK is shown in figure 6.2.

The results of our measurements described above are shown in figure 6.3 together with the fits according to equations (6.1) and (6.2). At every height z and temperature T we calculate the value for C according to equation (6.3). The quality factor far from the surface $Q_0 = 2.8 \cdot 10^4$. The stiffness $k_0 = 7.0 \cdot 10^{-5} \text{ Nm}^{-1}$ of the cantilever is calculated using $k_0 = m_{eff} (2\pi f_0)^2$ with $f_0 = 3.0$ kHz and $m_{eff} = 2.0 \cdot 10^{-13}$ kg. The effective mass m_{eff} is calculated using the geometry of the cantilever and the magnetic particle. The magnetic particle is taken as a spherical dipole with magnetic moment \mathbf{m} . According to the model, the temperature at which the resonance frequency close to the sample has a maximum, is independent of σ and T_1 , but is dependent on the absolute value of \mathbf{m} and the distance to the sample. We find $m = 1.9 \cdot 10^{-11} \text{ JT}^{-1}$. From this we find an effective saturation magnetization of 1.15 T for a sphere that is fully magnetic. Alternatively we can assume $\mu_0 M_{sat} = 1.3$ T and an outer layer

²The piezoelectric extension stacks are of type P-883.51 by Physik Instrumente GmbH and Co. KG. Germany. To determine the range of the finestage, we extrapolated data from reference [102] for the actuator constant from 20 K to 0 K.

Table 6.1: Obtained values for the spin density σ and relaxation time T_1 for every height z above the sample. See 6.3 for the individual fits figure. The bottom row shows the average value and the standard deviation.

Height (μm)	spin density (nm^{-2})	Relaxation time (ms)
0.08	0.142	0.42
0.19	0.137	0.52
0.38	0.140	0.48
0.57	0.142	0.42
0.77	0.136	0.38
1.15	0.130	0.32
1.72	0.133	0.28
2.30	0.168	0.33
mean:	0.14 ± 0.01	0.39 ± 0.08

of 200 nm which is magnetically dead. The magnetic moment of the dangling bonds [103] is equal to the Bohr magneton $\mu = 9.274 \cdot 10^{-24} \text{JT}^{-1}$.

The solid lines in figure 6.3 are fits to the data according to equations (6.1) and (6.2) with σ , T_1 and f_0 as the only fitting parameters. All fitting parameters are separately fitted for each height, for both the frequency data and the quality factor data. f_0 is a temperature independent parameter different for each height, which we attribute to an unknown mechanism, since the coupling to the SQUID is too small of an effect at these distances and has a height dependence with opposite sign to the one observed. The results of the fits for T_1 and σ can be found in table 6.1. We left σ as fitting parameter for each height, to verify the correctness of our analysis, since this number should be the same for each height. We see that T_1 slightly increases when the magnetic particle approached the surface, as is also observed for bulk spins in electron spin resonance experiments [59]. T_1 could depend on temperature, but by taking the ratio of equation (6.1) with equation (6.2) we extract T_1 for each measurement, and we find that T_1 is constant with temperature to within 20%. The average values of all individual fits are $\sigma = 0.15 \pm 0.01$ spins per nm^2 and $T_1 = 0.20 \pm 0.04$ ms. The found value for σ is similar to values measured using Electron Paramagnetic Resonance [103, 104].

The dashed line in figure 6.3 is the frequency shift calculated with the commonly used expression $k_s = p\mu \cdot \frac{d^2 B}{dx^2}$, with $p = \tanh\left(\frac{\mu B(\mathbf{r})}{k_B T}\right)$. Important is that for this curve, the spin density is ten times smaller than we find with our analysis.

6.5 Discussion

The deviation of the data from the fit for low temperatures and small values for z can be understood by considering that we do not have only spins at the surface. Electron spins inside the bulk will cause deviations to the fits, already when the density is in the order of 10^4 spins per μm^3 which is less than 1 ppm of the silicon atoms. Considering the nuclear spins, the 4.7% natural abundance of the ^{29}Si isotope can only account for less than 1 percent deviation.

Note that in electron spin resonance studies with our MRFM setup, a value for T_1 in the order of seconds was reported [20]. With our new analysis we believe that it is possible that the reported long lived frequency shifts could be caused by nuclei polarized by interactions with these electron spins, and that these electron spins were actually much shorter lived, as is reported for nitroxide-doped perdeuterated polystyrene films [41].

Our analysis suggests that the spin mediated dissipation is the main mechanism leading to a significant reduction in the quality factor of the cantilever. Previous work at higher temperatures [98] reports dielectric fluctuations as the main non-contact dissipation mechanism. We do not see any evidence in our measurements for this. Possibly, the use of a laser in the setup to read out the cantilever causes extra charge fluctuations. Furthermore, we work at lower temperatures, where the large spin polarization enhances the magnetic dissipation and possibly reduce fluctuating charges.

Table 6.2: Calculated quality factor Q for three different temperatures and external magnetic fields assuming magnetic dissipation as the only source for non-contact friction. Calculations are based on a state-of-the art MRFM apparatus with a ‘sample on cantilever’ geometry [2] and a cantilever [16] with an internal quality factor $Q_0 = 1.5 \cdot 10^6$.

Calculated quality factors ($\cdot 10^6$)			
	$T = 10$ mK	$T = 300$ mK	$T = 4.2$ K
$B_{ext} = 0$ T	0.49	0.20	0.98
$B_{ext} = 0.1$ T	1.50	0.19	0.91
$B_{ext} = 6$ T	1.50	1.50	1.17

6.6 Conclusion

We calculated the magnetic dissipation for a magnetic imaging experiments at higher temperature and a different tip-sample geometry. The results can be found in table 6.2. We used the experimental parameters for a state-of-the-art MRFM [2]. In this apparatus, the bare non-magnetic cantilever is centered approximately 50 nm above a magnetic particle on the substrate, which is assumed for simplicity to be a spherical particle with a radius of 100 nm. This setup is equivalent to a magnetic dipole attached to the cantilever itself approaching a surface with the shape of the cantilever. The magnetic dipole and external field are oriented in the z-direction while the fundamental mode of the cantilever is in the x-direction. For the cantilever, we used the parameters of a recently developed diamond cantilever [16] which is shown to have at low temperatures an intrinsic quality factor $Q_0 = 1.5 \cdot 10^6$, resonance frequency $f_0 = 32$ kHz and stiffness $k_0 = 6.7 \cdot 10^{-2}$ Nm⁻¹. A spin density $\sigma = 0.15$ nm⁻² is used, which is found in this report to be the density for the silicon surface, but it is also close to the typical values found for diamond surfaces [105]. Only spins at the very end of the cantilever are considered since this surface contributes most to the dissipation, which is 0.66 μ m thick and 12 μ m wide. Although equation (6.1) cannot be used since we do not have a uniform infinite surface anymore, according to the original expressions [21] one can continue to use equation (6.2) for the dissipation replacing the integral in equation (6.3) over the end of the cantilever. The relaxation time is chosen such that the dissipation is maximum: $T_1 = (2\pi f_0)^{-1} = 5.0$ μ s.

The values in table 6.2 show that the magnetic dissipation could be an important source of non-contact friction. Furthermore we see that applying external fields can reduce the magnetic dissipation. Considering these calculations we believe that the magnetic dissipation we find at low temperatures can be avoided with the correct choice for the substrate and the use of large external magnetic fields.

To summarize, we have shown how the dissipation and frequency shift mediated by spins in magnetic force experiments can be fully understood. The new analysis suggest that in order to achieve higher sensitivity in magnetic imaging techniques, one should not only focus on improving the intrinsic losses of the micro-mechanical cantilever, but also on the reduction of electron spins in the sample. Furthermore we have shown how the spin’s relaxation time can be extracted without the use of resonance techniques. For silicon substrates with native oxides, we find a relaxation time of $T_1 = 0.20 \pm 0.04$ ms and a spin density of $\sigma = 0.15 \pm 0.01$ per nm². The

understanding of the spin mediated dissipation is important to further improve the mechanical resonators in magnetic imaging experiments.

Chapter 7

Nuclear magnetic resonance force microscopy at millikelvin temperatures

This chapter is in preparation to be published with the following authors: J. J. T. Wagenaar*, A. M. J. den Haan*, J. M. de Voogd, K. M. Bastiaans, T. de Jong, D. J. Thoen, A. Endo, T. M. Klapwijk and T.H. Oosterkamp

*These authors have contributed equally

We report nuclear magnetic resonance force microscopy experiments down to temperatures of 42 mK, in which we measure nuclear spin relaxation times. We measured the Korringa relation between the nuclear relaxation time and temperature for a 300 nm thick copper sample. Performing local nuclear magnetic resonance experiments at such low temperatures enables an improvement in the microscope's sensitivity and opens up possibilities for future investigations of condensed matter systems at very low temperatures.

7.1 Introduction

During the last decade, a lot of progress has been made in understanding novel quantum materials and unresolved problems in high-Tc superconductors. Nuclear Magnetic Resonance has helped to study local magnetic fields and their inhomogeneities. A tool that could provide such information *on a local scale* would be very useful. State of the art Magnetic Resonance Force Microscopy (MRFM) has demonstrated a resolution smaller than 10 nm, by detecting proton spins in a virus particle [2]. MRFM has also shown to be able to measure relaxation times down to 4.8 K of nuclear spins in GaAs [106]. We demonstrate that MRFM can also be used to study the temperature

dependence of the relaxation time T_1 in copper, the so-called ‘Korringa relation’¹, at low temperatures between 42 and 240 mK. We believe this opens up the possibility to use nanoscale NMR investigations of various materials, where electronic properties are inhomogeneous, such as in Topological Insulators in which bulk conductivity and surface conductivity can vary by orders of magnitude.

In most MRFM apparatus, the use of a laser in the readout of the motion of the cantilever, combined with RF currents that are applied using a copper or gold wire [30], prevent experiments at temperatures below 300 mK. We make use of a superconducting readout of the motion, combined with a superconducting RF-wire. We show that with this, we can reach local temperatures down to 42 mK, currently limited only by the performance of our dilution refrigerator. The local temperatures during magnetic resonance experiments are verified by measuring the Korringa law $T_1 T = \kappa$ of a copper sample, with T_1 the relaxation time of the copper nuclei and T the (electron) temperature. κ is the Korringa constant, which is expected to be 1.2 sK [84, p. 225].

7.2 Experimental setup

The experimental setup is described in chapter 2 and closely resembles the setup described in chapter 6. A summary, with the relevant details of the experimental setup, is written below.

The cantilever’s natural resonance frequency is 3.0 kHz with a mechanical quality factor $Q = 3 \cdot 10^4$, when far away from the surface. The sample under study can be approached coarsely in a range of 1 mm in x,y and z while reading out the position using three capacitive sensors. The sample holder is placed on a finestage which is used to control the z-position in a range of 2.3 μm . The fabrication of the sample is described in detail in section 2.4.

7.3 Methods

We positioned the cantilever above the copper, sufficiently close to the pick-up coil for a good coupling and close to the RF wire (as indicated by a small black dot in figure 7.1). Using the position of the center of the pick-up coil, which is found by maximizing the coupling of the magnetic particle with the pick-up coil, we determined the position to be $5 \pm 1 \mu\text{m}$ from the pick-up coil and $7 \pm 1 \mu\text{m}$ from the center of the RF wire. While approaching the copper, we measured an enormous drop in quality factor of the cantilever towards below $Q < 1000$. This is caused by the eddy currents of the copper induced by the magnetic fields of the magnetic particle attached to the cantilever. Due to this drop in quality factor, we were not able to determine the initial height above the copper with more than 0.5 μm precision.

¹Korringa relation: A relation for metals in which $\frac{1}{T_1}$ is proportional to the temperature. The relaxation process is induced by a simultaneous flip of the free electron spins and the nuclear spins. The energy for this process is provided by the scattering of the electrons (change in kinetic energy of the electron), with energy $\hbar(\omega_e - \omega_n)$, where ω_e and ω_n are the larmor frequency of the electron spin and the nuclear spin respectively [107, p. 363][108, p. 121].

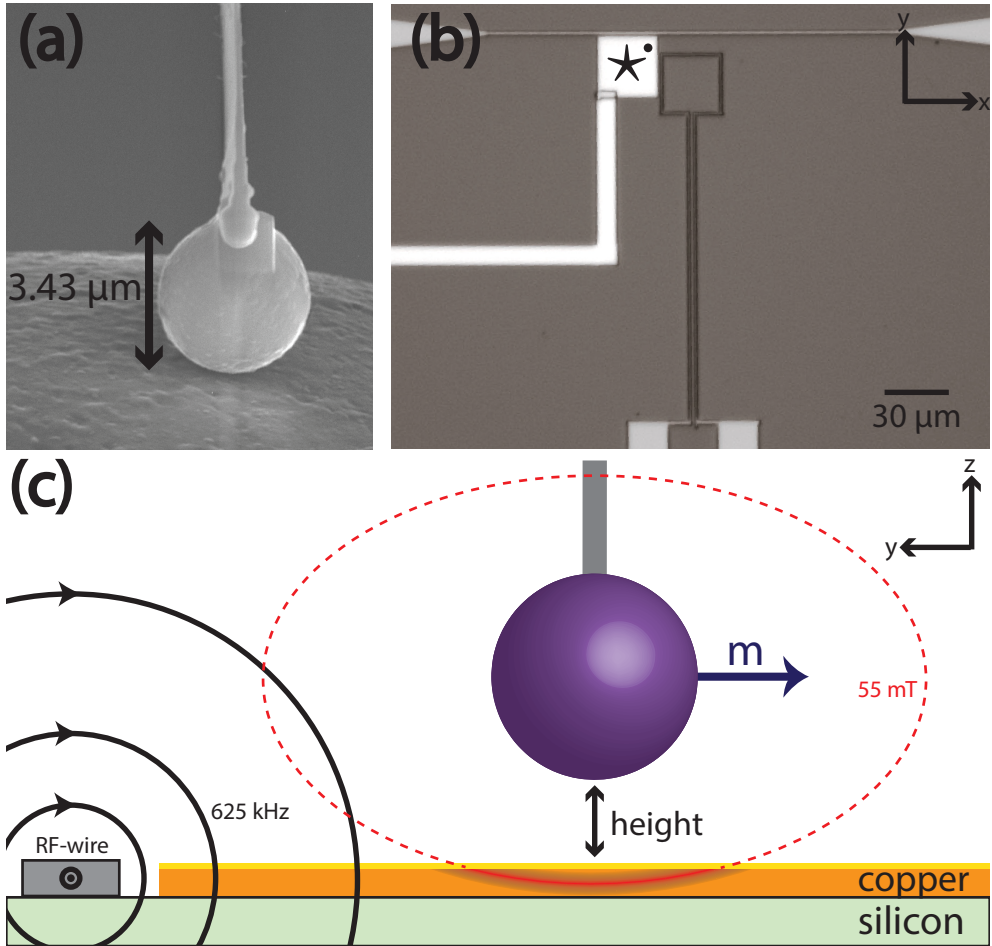


Figure 7.1: **a)** Scanning electron microscope image of the magnetic particle after it is glued to the cantilever using electron beam induced deposition from a platinum containing precursor gas. **b)** Optical microscope image of the detection chip. The horizontal wire at the top is the NbTiN RF wire. The \star indicates the gold capped copper sample which is connected to a wire used for thermalization. The small black dot is where we perform the MRFM experiments presented in this chapter. Next to the sample and below the RF wire is the pick-up coil for detection of the cantilever's motion. **c)** Schematic drawing of a side view of the local NMR experiment.

Nuclei close to the magnetic particle experience a magnetic field $\mathbf{B}(\mathbf{r})$ and the gradients of the magnetic field provide a coupling with the magnetic cantilever, which results in an effective frequency shift per spin on the natural frequency f_0 of the cantilever [109, 97]. The alignment of the nuclear spins will be perturbed when a radio-frequent pulse with frequency f_{RF} is applied to the sample. We call the volume containing the spins that meet the resonance condition $hf_{RF} = \gamma B(\mathbf{r})$ the resonance slice. When the spins are inverted, the cantilever will experience a frequency shift $-2\Delta f_0$, while for ensembles of spins that lose their net Boltzmann polarization the

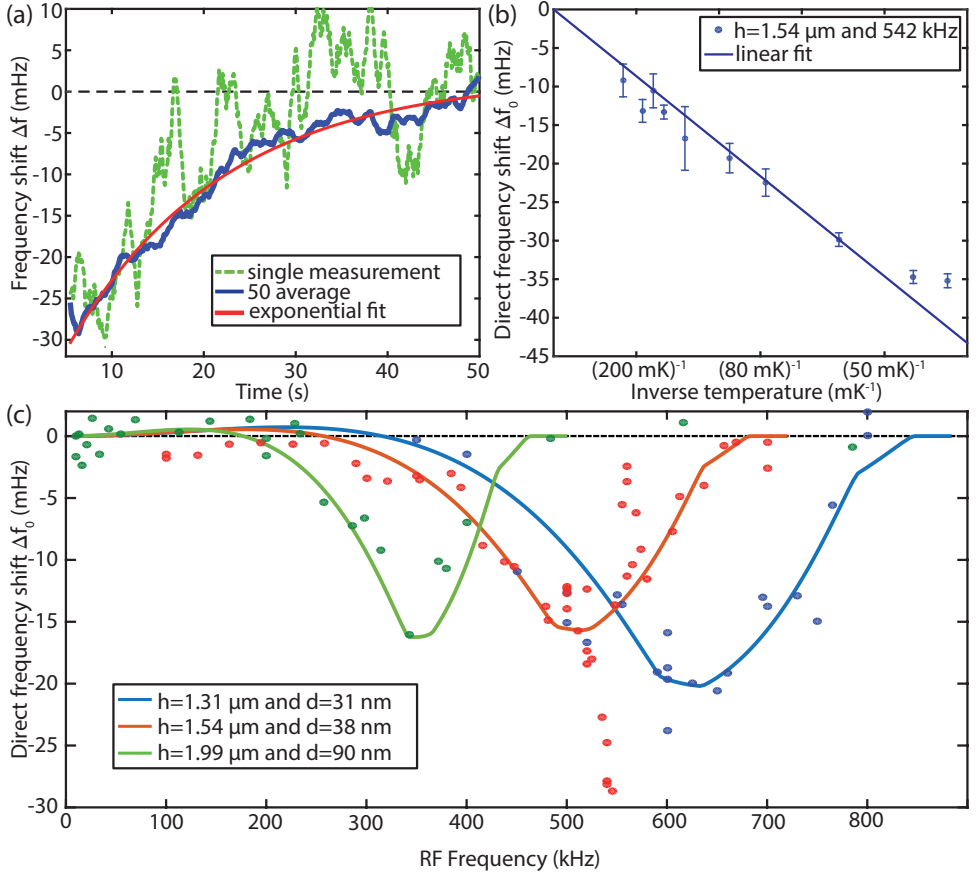


Figure 7.2: **a)** At $t = 3$ s a RF-pulse with a pulse width of one second saturates all spins within a resonance slice resulting in a direct frequency shift Δf_0 of the cantilever's resonance frequency. The shift relaxes with the nuclear spin's relaxation time T_1 . The dashed green line shows a single measurement of the frequency shift (with a moving average of 1 second), the solid blue line shows 50 averages. The red solid line is an exponential fit according to equation 7.1. From the fit we extract the direct shift Δf_0 , extrapolated at $t = 4$ s directly after the pulse, and relaxation time T_1 . **b)** The direct frequency shift Δf_0 versus temperature. The linear fit is expected according to Curie's law $M \propto T^{-1}$. **c)** Δf_0 as function of RF frequency f_{RF} for three different cantilever heights. The solid line is a simulation with the cantilever height z and resonance slice width d as the only fitting parameters.

frequency shift will be $-\Delta f_0$. The latter effect can easily be obtained at very low radio frequent magnetic fields in a saturation experiment, ensuring no heating of the sample at very low temperatures.

Taking the approximation of a circular wire, we estimate the typical field strength $B_1 = \frac{\mu_0 I}{4\pi r} \approx 2.8 \mu\text{T}$, for a current of 0.2 mA. We assumed that the RF field is perpendicular to the static field B_m , even though this is not always the case (see figure 7.1c). With this, we can calculate the saturation parameter $s \equiv \gamma^2 H_1^2 T_1 T_2$. We see that for the expected relaxation times $T_1 > 5$ s and $T_2 = 0.15$ ms we obtain a saturation

parameter in the order of 1, showing that the spins will be at least 50 % saturated. Note that this only holds for spins exactly at the resonance condition, and since we work with field gradients, we always have spins that do not fully saturate. For the sake of simplicity, we assume that we have a resonance slice thickness d , within which the spins are fully saturated. Since we apply pulses of 1 second, we expect a full saturation of all levels (in pure copper, no quadruple interaction is expected), and according to Suter et al. [110], we expect that after the pulse the magnetization will restore according to a single-exponential, with a decay time equal to the spin lattice relaxation time T_1 . Since our frequency shift of the cantilever is proportional to the magnetization, we can fit our data with:

$$\Delta f(t) = f_0 + \Delta f_0 \cdot e^{-(t-t_0)/T_1} \quad (7.1)$$

We use the Phase Locked Loop (PLL) of a Zurich Instruments Lock-in amplifier to measure the shifts in resonance frequency of the cantilever at a bandwidth of 40 Hz. The measurement scheme is as follows: Between $t = 0$ s and $t = 3$ s the resonance frequency of the cantilever f_0 is measured using a PLL. At $t = 3$ s the PLL is turned off and the RF current is turned on. At $t = 4$ s the RF current is turned off. Around $t = 5$ s the PLL is turned on and measures the frequency shift relative to f_0 . The reason we switch off the PLL during the RF pulse and turn it back on one second after the RF pulse, is to avoid crosstalk.

The RF current of 0.2 mA is applied using a function generator. The current is chosen in such a way that the saturation parameter is much larger than 1. For currents larger than 1 mA we observe a temperature increase at frequencies larger than 1 MHz. The dissipation of our RF wire will be subject of further study. In this report we stay away from the maximum currents at the applied frequencies before heating.

7.4 Results

In figure 7.2a, a measurement is shown at a temperature of 42 mK and a RF-frequency of 542 kHz while the cantilever was at the position used for the red curve in figure 7.2c). At the frequency of 542 kHz, the frequency shifts were larger than at other frequencies, probably due to the broadening of the resonance slice due to the excitation of a higher cantilever mode. We measured the frequency shift until $t = 50$ s. We averaged every measurement 50 times and fit it with equation 7.1. From the fit, we extracted Δf_0 and T_1 . Δf_0 is plotted against temperature in figure 7.2b) and fit with a straight line according to the expected Curie's law $\Delta f_0 \propto \langle \mu \rangle \propto \frac{1}{T}$. At the lowest temperature we may see the onset of saturation of the frequency shift effect, indicating that the (electron) spins are difficult to cool, although the saturation may also have been reached because the minimum temperature of the refrigerator was reached. For every temperature we collected at least three sets of 50 curves, and the error bars are the standard deviations calculated from the three separate fits.

In figure 7.2c) the direct frequency shift is plotted versus RF frequency for three different cantilever heights. The height is controlled by changing the voltage of the

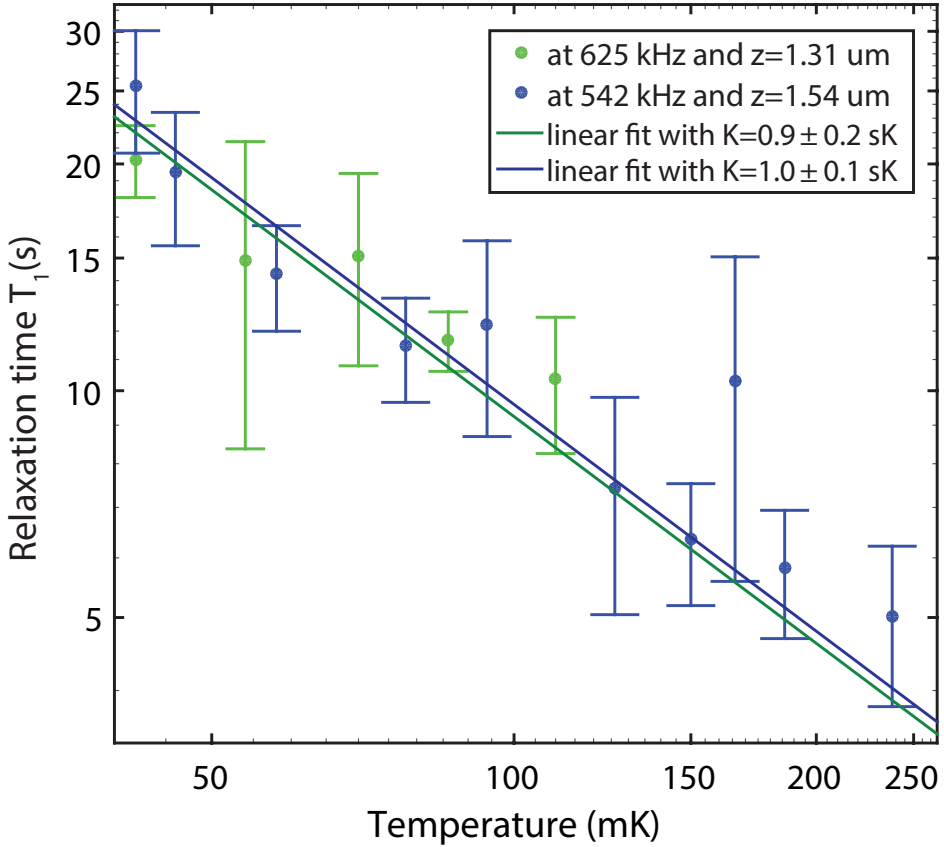


Figure 7.3: The inverse of the relaxation time of the copper nuclei measured by applying saturation pulses versus temperature. We find the same linear dependence with temperature as is found in bulk copper samples, the so called Korringa relation. In blue, the data is measured at a height of $1.54 \mu\text{m}$ at 542 kHz . In green, the data is recorded at $1.31 \mu\text{m}$ and at a frequency of 625 kHz . We find $\kappa = 1.0 \pm 0.1 \text{ sK}$ and $\kappa = 0.9 \pm 0.2 \text{ sK}$ respectively with a linear fit with the error indicating the 95 % confidence intervals. Every data point is an average of at least three sets of averaged data. The error bars give the standard deviation of the relaxation times for the averaged data sets.

finestage below the sample. Every data point resembles a dataset of 50 averaged single measurements. The solid line is a fit to the data, with the only fitting parameters the resonance slice width and height of the cantilever. The stiffness and magnetization of the cantilever is extracted from previous measurements [97]. The height of the cantilever is left as a fitting parameter, because the absolute height is not known with sufficient accuracy, since the piezo-stack in the finestage behaves nonlinear.

For two different RF frequencies, 542 kHz and 625 kHz , at two different heights of the cantilever, $1.54 \mu\text{m}$ and $1.31 \mu\text{m}$, we measured the relaxation time T_1 as a function of temperature to verify the local temperature. The results are shown in figure 7.3. From the straight fits we extract the Korringa constant $\kappa = 1.0 \pm 0.1 \text{ sK}$ and $\kappa = 0.9 \pm 0.2 \text{ sK}$, which is close to the expected value of the combined ^{63}Cu and

Table 7.1: NMR constants and parameters for copper [111, 112, 113, 84].

parameter	variable	Value
Radius magnet	R_0	3.43/2 μm
Magnetization	RMT	1.15 T
Copper layer thickness	d_{Cu}	300 nm
Gyromagnetic ratio ^{63}Cu	γ_{63}	11.3 MHz/T
Gyromagnetic ratio ^{65}Cu	γ_{65}	12.1 MHz/T
Natural abundance ^{63}Cu		69 %
Natural abundance ^{65}Cu		31 %
Spin-Spin relaxation time	T_2	0.15 ms
Korringa constant ^{63}Cu	κ_{63}	1.27 sK
Korringa constant ^{65}Cu	κ_{65}	1.09 sK
Local field	B_{loc}	0.34 mT

^{65}Cu Korringa constants which is $\kappa = 1.2$ sK [84, p. 225].

In the simulations (solid lines in Figure 2c), we have employed the formula's for the frequency shifts as they were calculated by De Voogd et al. in reference [109] with the parameters for copper (Table 7.1). Several things contribute to the width of the resonance slice, as will be described below. This leads to the resonant slice thickness not being the same everywhere in the slice. For the simulations of this experiment we have taken the resonant slice thickness to be uniform over the resonant slice.

7.5 Discussion

7.5.1 The Korringa constant

Let us first discuss the comparison between the Korringa constants we found, $\kappa = 1.0 \pm 0.1$ sK and $\kappa = 0.9 \pm 0.2$ sK, and the expected value based on the natural abundances and Korringa constants of the two copper isotopes (Table 7.1) of $\kappa = 1.2$ sK for bulk NMR measurements. We see a possible small deviation, which we may or may not attribute to the different mechanisms enumerated below.

First, there is the effect of flip-flop processes between nuclear spins which gives diffusion of the saturated magnetization. if the diffusion after several seconds is larger than the typical length scales at which the coupling with the cantilever decays, this can be a considerable effect. To explore this possibility, we first need to calculate the spin diffusion constant.

For poly-crystalline copper, we find a transition rate of $W = \frac{1}{30T_2}$ [107, p. 138-139] [114]. We use $T_2 = 0.15$ ms and we find $W = 2.2 \cdot 10^2 \text{ s}^{-1}$. Our field gradients are too small to suppress the spin diffusion [115]. The nearest neighbor distance a is 0.256 nm [116, p. 24]. This gives us a spin diffusion constant of $D = Wa^2 = 15 \text{ nm}^2\text{s}^{-1}$. This yields a diffusion length, l_D , after one second of $l_D = 2\sqrt{Dt} = 7.6$ nm. For the lowest temperature of 42 mK, we expected a Korringa constant of 28 seconds, resulting in $l_D = 40$ nm. We measured the Korringa relation at a position where a maximum signal was obtained. The signal when the spin has moved 40 nm further

in the x-direction can be calculated to have an estimate if this can have affected the observed Korringa relation. We see for the frequency of 625 kHz a reduction of the magnetization of approximately 10%. From this we can say that the lower Korringa relation could possibly be caused by the spin diffusion of the saturated magnetization in the resonance slice towards areas where the coupling with the cantilever is smaller. Also, the spin diffusion can possibly give an additional relaxation channel [107, p. 139].

A second mechanism to obtain a shorter T_1 time is discussed by [112] and may be caused by electronic magnetic impurities. Also in reference [111] it is discussed that tiny impurities can alter the Korringa constant. We don't expect impurities to play a big role, because the copper was capped with gold. However, the dangling bonds at the surface of the silicon substrate [97] could have been an additional relaxation channel for nearby copper nuclei.

7.5.2 The resonance slice thickness

We also would like to discuss the resonant slice thickness we found, since this is important for the resolution of possible future imaging or spectroscopic experiments, or when similar measurements are performed on much thinner films.

First, there is the width of the Lorentzian resonance curve in a conventional magnetic resonance experiment [107]. The full width half maximum (FWHM) is equal to twice the Rabi frequency. In our case that is approximately $6 \mu\text{T}$. When this number is divided by the field gradient $|\nabla_r \mathbf{B}(\mathbf{r})|$ which is up to $5 \cdot 10^4 \text{ T/m}$, we obtain a thickness $d = 0.1 \text{ nm}$, which cannot account for the found resonance slice thickness by the simulation in figure 7.2c).

Secondly, we need to consider the motion of the cantilever itself. We estimate from the quality factor at each height and the piezo's drive amplitude, that we drove the cantilever 60, 37 and 100 nm respectively for the found slice thicknesses of 90, 38 and 31 nm. The cantilever's motion is in the x-direction, while in our simulation, we take in the resonance slice thickness in the radial direction. When we perform the simulation and take the slice thickness only in the x-direction, we see a best fit with the data for a cantilever motion of approximately 250, 100 and 90 nm respectively. From this we conclude that a resonance slice thickness only determined by the motion in the x-direction of the cantilever is not likely, and that there is another mechanism that broadens the resonance slice in the radial direction.

One possibility to broaden in the radial direction is the effect of the local fields. The copper nuclei have an internal field of 0.34 mT, caused by direct coupling with neighbors and by indirect coupling via conduction electrons with neighbors. We can approximate the internal field as a Gaussian distribution. During a RF pulse, the spin can feel a different local magnetic field due to a changing environment, or the spin can flip-flop with a neighboring spin [114]. The flip-flop speed is $W = 2.2 \cdot 10^2 \text{ s}^{-1}$, as calculated before, and the number of Rabi oscillations with the one second pulse is $\gamma B_1 \cdot 1 \text{ s} \approx 3 \cdot 10^1$. From these numbers we can conclude that it is likely that the resonance slice is broadened by approximately the distribution of the local magnetic field. When we take the obtained resonance slice thicknesses of 90, 38 and 31 nm, we calculate that we need a broadening of 6.3, 4.3 and 4.6 times the average local field strength respectively. These numbers are not unlikely, considering that within

a small volume only a small fraction of spins needs to have the exact local field to meet the resonance condition within $|\mathbf{B}(\mathbf{r}) - \mathbf{B}_1| < |\mathbf{B}(\mathbf{r}) + \mathbf{B}_{loc}| < |\mathbf{B}(\mathbf{r}) + \mathbf{B}_1|$, after which the flip-flops or the changing environment can destroy the magnetization of the whole ensemble.

7.6 Conclusion

To summarize, we have performed nuclear magnetic resonance force microscopy experiments down to 42 mK. We verified the local temperature by verifying the Korringa relation for copper. Since this relation is a direct probe of the electronic susceptibility of the material, we believe that MRFM may prove to be a useful tool for measuring novel quantum materials.

-

Chapter 8

Radio frequency pulses for nuclear magnetic resonance force microscopy

Radio frequent pulses are one of the crucial ingredients in magnetic resonance force microscopy. The magnitude of the spin signal is influenced by the used RF pulse sequence. Moreover, issues involving spurious crosstalk, heat dissipation, and incomplete inversions are important considerations in designing the pulse. In this chapter, several radio frequent pulses, used in NMR and MRFM will be discussed.

As discussed in Chapter 3, in MRFM one can focus either on creating a force interaction or a gradient force interaction between the spins and the magnetic particle of the cantilever. This requires different RF pulses according to the desired interaction. The goal of this chapter is to provide a basic and intuitive understanding of the ways to influence spins, which may be relevant for designing new experiments, especially in our group. In addition, we propose a pulse sequence which is used in NMR and MRI, which may be useful for MRFM experiments in which T_2 measurements are relevant.

In the first sections the motion of a (classical) magnetic moment, with only an external magnetic field (section 8.1) and with time varying magnetic field (section 8.2 and section 8.3) will be described. These sections form a foundation for the explanation of common RF pulses (section 8.4) and adiabatic inversions (section 8.5). In section 8.6, the pulse sequence called B_1 Insensitive Rotation (BIR) will be described. In the final sections (sections 8.7, 8.8 and 8.9), the use of adiabatic pulses in MRFM and relevant pulses for our group will be discussed.

8.1 The motion of a magnetic moment in an external magnetic field

In the following part, we will use a semiclassical description. Further, we will assume that the spins are not interacting and that no dissipation channels are present. The

equation of motion for a magnetic moment $\boldsymbol{\mu}$ in an external magnetic field \mathbf{B} is found by equating the torque $\boldsymbol{\mu} \times \mathbf{B}$ and the rate of change of the angular momentum \mathbf{J} :

$$\frac{d\mathbf{J}}{dt} = \boldsymbol{\mu} \times \mathbf{B} \quad (8.1)$$

Hence, since $\boldsymbol{\mu} = \gamma\mathbf{J}$:

$$\frac{d\boldsymbol{\mu}}{dt} = \boldsymbol{\mu} \times \gamma\mathbf{B} \quad (8.2)$$

where γ is the gyro-magnetic ratio. Since the direction of change is perpendicular to both $\boldsymbol{\mu}$ and \mathbf{B} , the magnetic moment vector will precess around the external magnetic field, thereby describing a cone. Note that the initial angle between the magnetic moment and the external field remains fixed during precession. The frequency at which the magnetic moment precesses around the magnetic field is called the Larmor frequency, which is: $\boldsymbol{\omega}_L = \gamma\mathbf{B}$.

It is convenient to define a rotating reference frame, in which this frame is rotating with an arbitrary angular frequency $\boldsymbol{\Omega}$ relative to the inertial frame (also called the laboratory frame). In this rotating reference frame, the equation of motion of the magnetic moment is [108, p. 12]:

$$\frac{\delta\boldsymbol{\mu}}{\delta t} = \boldsymbol{\mu} \times \gamma(\mathbf{B} + \boldsymbol{\Omega}/\gamma) \quad (8.3)$$

In which the symbol $\delta/\delta t$ represents the time derivative in the rotating reference frame. Note that now the magnetic field \mathbf{B} is in terms of the rotating reference frame coordinates. This equation is similar to equation 8.2 by replacing the magnetic field with an effective magnetic field: $\mathbf{B}_{\text{eff}} = \mathbf{B} + \boldsymbol{\Omega}/\gamma$. Therefore the magnetic moment is precessing around the effective magnetic field \mathbf{B}_{eff} in the rotating reference frame. This rotating reference frame description is convenient when time varying magnetic fields are used, since a varying magnetic field appears to be static when the reference frame rotates with the angular rotation of the varying magnetic field. From equation 8.3, we see that the magnetic moment is static in the rotating reference frame ($\frac{\delta\boldsymbol{\mu}}{\delta t} = 0$) when the direction and amplitude of the angular frequency matches to the Larmor frequency ($\boldsymbol{\Omega} = -\boldsymbol{\omega}_L = -\gamma\mathbf{B}$).

8.2 Time varying magnetic field

By applying a time varying magnetic field $\mathbf{B}_1(t)$, which can be achieved by sending radio frequent (RF) waves, one can influence the magnetic moment of spins. In the laboratory frame, the equation of motion of a magnetic moment will be:

$$\frac{d\boldsymbol{\mu}}{dt} = \boldsymbol{\mu} \times \gamma(\mathbf{B} + \mathbf{B}_1(t)) \quad (8.4)$$

In the rotating reference frame, the time dependence of the \mathbf{B}_1 field can be dropped when the varying magnetic field is rotating with $\boldsymbol{\Omega}$. To prevent \mathbf{B} to get a time

dependence in terms of the new coordinates, $\mathbf{\Omega}$ needs to be parallel to \mathbf{B} . This means that \mathbf{B}_1 will be perpendicular to \mathbf{B} . Therefore in the rotating reference frame:

$$\frac{\delta\boldsymbol{\mu}}{\delta t} = \boldsymbol{\mu} \times \gamma(\mathbf{B} + \mathbf{\Omega}_{\parallel\mathbf{B}}/\gamma + \mathbf{B}_{1\perp\mathbf{B}}) \quad (8.5)$$

Most of the processes in magnetic resonance are described in the rotating reference frame, rotating with the \mathbf{B}_1 field.

8.3 Sending an RF field

Suppose, a radio frequent field is sent in the x-direction (laboratory frame) and the external magnetic field is pointing along the z-direction. Then the magnetic field from this electromagnetic wave can have the following form: $\mathbf{B}_x = 2B_1\cos(\omega t)\hat{\mathbf{x}}$, which can be decomposed into a left rotating \mathbf{B}_L and right rotating field \mathbf{B}_R :

$$\mathbf{B}_x = \mathbf{B}_L + \mathbf{B}_R \quad (8.6)$$

$$\begin{aligned} \mathbf{B}_R &= B_1(\cos(\omega t)\hat{\mathbf{x}} + \sin(\omega t)\hat{\mathbf{y}}) \\ \mathbf{B}_L &= B_1(\cos(\omega t)\hat{\mathbf{x}} - \sin(\omega t)\hat{\mathbf{y}}) \end{aligned} \quad (8.7)$$

Where $2B_1$ is the amplitude and ω is the angular frequency of the radio frequent field. From equation 8.7, we see that \mathbf{B}_L interchanges with \mathbf{B}_R by replacing ω by $-\omega$. Therefore, when \mathbf{B}_R is at resonance, the influence of \mathbf{B}_L is negligible and vice versa, since the difference in angular frequency is 2ω . By defining an angular frequency ω_z which can be positive or negative, the rotating magnetic field will be:

$$\mathbf{B}_1 = B_1(\cos(\omega_z t)\hat{\mathbf{x}} + \sin(\omega_z t)\hat{\mathbf{y}}) \quad (8.8)$$

Therefore \mathbf{B}_1 will become \mathbf{B}_L or \mathbf{B}_R , depending on ω_z . Using equation 8.4 with (B_0 in $\hat{\mathbf{z}}$) we have:

$$\frac{d\boldsymbol{\mu}}{dt} = \boldsymbol{\mu} \times \gamma(B_0\hat{\mathbf{z}} + B_1\cos(\omega_z t)\hat{\mathbf{x}} + B_1\sin(\omega_z t)\hat{\mathbf{y}}) \quad (8.9)$$

The time dependence of \mathbf{B}_1 can be dropped in the rotating reference frame, where the coordinate system rotates about the z-direction with angular frequency ω_z . Using equation 8.5, the motion of the magnetic moment will be:

$$\frac{\delta\boldsymbol{\mu}}{\delta t} = \boldsymbol{\mu} \times \gamma((B_0 + \omega_z/\gamma)\hat{\mathbf{z}}' + B_1\hat{\mathbf{x}}') \quad (8.10)$$

Where B_1 is taken along the x-direction. By taking $\omega_z = -\omega$, we see that the resonance condition for equation 8.10 will be $\omega = \gamma B_0$ for positive γ . In this case the left rotating field component of the radio frequent field causes the resonance for positive γ . The motion of the magnetic moment in the rotating reference frame, rotating with $-\omega$, is therefore [108, p. 21]:

$$\frac{\delta\boldsymbol{\mu}}{\delta t} = \boldsymbol{\mu} \times \gamma\mathbf{B}_{\text{eff}} \quad (8.11)$$

$$= \boldsymbol{\mu} \times \gamma((B_0 - \omega/\gamma)\hat{\mathbf{z}}' + B_1\hat{\mathbf{x}}') \quad (8.12)$$

8.4 Common RF pulses

In the following part we will describe pulses that are used in NMR and MRI. Again, we assume that initially the magnetic moment μ is pointed along the external magnetic field $B_0\hat{\mathbf{z}}$ in the z -direction. In resonance ($\omega = \gamma B_0$), the magnetic moment is precessing around $B_1\hat{\mathbf{x}}'$ in the rotating reference frame. Therefore the z -component of the magnetic moment is oscillating between positive z and negative z , with a frequency $\omega_1 = \gamma B_1$, called the Rabi- or nutation frequency. In the laboratory frame, the tip of the vector of the magnetic moment describes a spherical spiral around the z -axis. When the magnetic field is off-resonance, we see that the effective field, around which the magnetic moment is precessing, receives a z -component. In this case, the magnetic moment cannot reach the full magnitude along $\hat{\mathbf{z}}$. It is important to note however that off-resonant excitation does excite the spins. As a rule of thumb, it helps to keep in mind that the width of a peak in an NMR spectrum has a width (at full width half maximum (FWHM)) that is at least as wide as twice the B_1 field, $\delta\omega_{FWHM} = 2\gamma B_1$.

Any rotation θ , relative to the z -axis of the magnetic moment can be achieved by sending a resonance RF pulse with amplitude B_1 for a duration of $\tau = \theta/(\gamma B_1)$. The magnetic moment will be rotated to the transverse plane when a so-called $\pi/2$ -pulse or 90 degree pulse is applied. A 180 degree rotation of the magnetic moment is called the π -pulse or inversion pulse.

8.5 Adiabatic inversion

In conventional MRI and NMR, $\pi/2$ -pulses and π -pulses are commonly used. However, for MRFM applications these pulses are less convenient for several reasons: First, due to the demand of low dissipation and high power RF sources, generally these sources do not generate a homogeneous B_1 field, which makes $\pi/2$ and π -pulses unsuitable because different positions in the sample require to have different pulse widths. The second argument will be made clear in the following: In MRFM, the signal to noise ratio increases if the spin has a force interaction with the cantilever (force sensor). This force interaction is achieved by driving the spins in resonance with the cantilever. If one tries to drive the cantilever with Rabi-oscillations (continuous π -pulses), the B_1 field should be homogeneous and the Rabi frequency should exactly match the cantilever frequency (ω_c): $\gamma B_1 = \omega_c$.

When performing adiabatic pulses, on the other hand, the sweep time of the adiabatic pulses determines the time of inversion. Therefore, one can achieve exactly timed adiabatic inversions as long as the adiabatic condition is fulfilled: $\omega_c \ll \gamma B_1$, which will be described later. Finally, due to the inhomogeneous B_0 -field, the resonance slice thickness is more easily controlled by performing adiabatic pulses.

In the following, an adiabatic pulse will be described, in the rotating reference frame.

The magnetic moment can be inverted when the frequency of the B_1 field is swept from far below resonance to far above resonance. For convenience, assume that initially the magnetic moment μ is pointed along the external magnetic field $B_0\hat{\mathbf{z}}$ in the z -direction and assume that $B_1 \ll B_0$. Note that the description below

is also valid for a magnetic moment which is initially in the opposite direction. A magnetic moment, which is parallel to the effective field, is called *spin locked*. Likewise a magnetic moment, antiparallel to the effective magnetic field, is called *spin anti-locked*. Starting with a frequency of the B_1 field below resonance, the direction of the effective magnetic field and therefore the direction of the magnetic moment will alter only slightly. Moreover, the z-component of the effective magnetic field is dominant off-resonance, (assuming that $B_1 \ll B_0$).

We see that the effective field \mathbf{B}_{eff} rotates about the y-axis in the rotating reference plane as the frequency approaches resonance, see 8.12. Using equation 8.12, the magnitude of \mathbf{B}_{eff} and the angle α between the z-axis and \mathbf{B}_{eff} is:

$$B_{\text{eff}} = \sqrt{(B_0 - \omega(t)/\gamma)^2 + B_1(t)^2} \quad (8.13)$$

$$\alpha = \arctan\left(\frac{B_1(t)}{B_0 - \omega(t)/\gamma}\right) \quad (8.14)$$

We have kept the frequency ω and B_1 time-dependent, since adiabatic inversion described below requires a frequency and amplitude modulation. From these equations, we see that a sweep of the B_0 field can have the same effect as a frequency sweep of ω . Therefore an adiabatic inversion can equally well be performed by both methods.

It is now convenient to introduce another reference frame, in which the z-axis follows \mathbf{B}_{eff} in the rotating reference frame, also called the B_{eff} -frame, as in ref. [117]. Therefore we obtain a doubly rotating reference frame, which rotates with $\omega_a = \frac{d\alpha}{dt}$ about the $\hat{\mathbf{y}}'$ -axis. Hence, the motion of the magnetic moment in this reference frame is:

$$\frac{\tilde{\delta}\boldsymbol{\mu}}{\tilde{\delta}t} = \boldsymbol{\mu} \times \gamma (B_{\text{eff}}\hat{\mathbf{z}}'' + (\omega_a/\gamma)\hat{\mathbf{y}}'') \quad (8.15)$$

In which the symbol $\tilde{\delta}/\tilde{\delta}t$ represents the time derivative in the doubly rotating reference frame. From this equation, it becomes clear that in the case of a fast inversion (a large ω_a), the component in $\hat{\mathbf{y}}'' = \hat{\mathbf{y}}'$ -direction becomes significant. This means that, after an inversion pulse, the magnetic moment can have a component in the lateral direction, which therefore blurs the inversion. The magnetic moment only follows the effective magnetic field \mathbf{B}_{eff} , provided that:

$$\omega_a(t) \ll \gamma B_{\text{eff}} \quad \forall t \quad (8.16)$$

Since $B_1 \ll B_0$, the minimal magnitude of the effective magnetic field is equal to B_1 . Hence,

$$\omega_a(t) \ll \gamma B_1 \quad (8.17)$$

This is called the adiabatic condition. A full inversion can only be achieved if this adiabatic condition is fulfilled. In the previous description, we treated the spins as being isolated. However, the spins have interaction with their environment, i.e. spin-lattice interaction and spin-spin interaction. If the spin system applies to the Bloch equations [118], it is sufficient to add a condition in which the relaxation mechanisms due to the environmental interactions are negligible during the adiabatic inversion [18, p. 66]:

$$1/\omega_a(t) \ll T_1, T_2 \quad (8.18)$$

Combining this condition with the previous (Eq. 8.17) and since T_2 is usually much smaller than T_1 ($T_2 \ll T_1$):

$$\frac{1}{T_2} \ll \omega_a(t) \ll |\gamma B_1| \quad (8.19)$$

Since T_2 times can be very short, the necessary speed of the passage has caused the adiabatic inversion to be called ‘adiabatic rapid passage’ [18, p. 66]. However, for solids, this inequality is far too stringent with RF fields larger than the local field from neighboring spins. [18, p. 66] [119]. A hand-waving argument, according to Redfield et al. [119] is as follows: Suppose that the magnetization with magnitude (M_1) is initially in the direction of the RF field, then according to the Bloch equations, the magnetization will decay exponentially to zero in a time T_2 . The work during this decay is equal to $M_1 B_1$. Since we assumed that $T_2 \ll T_1$, the energy (during T_2) can only come from the spin-spin energy. Therefore, for $B_{loc} \ll B_1$ and due to conservation of energy, the spin system is not able to acquire the entire energy ($M_1 B_1$) corresponding to the applied rotating field B_1 , which means that the T_2 decay according to the Bloch equations is partially forbidden. As a result, the transverse decay for the component of the magnetization parallel to the B_1 field (say, x’-direction in the rotating frame) is rather in the order of the T_1 time [119] [18, p. 66 and p. 539-545]. Meanwhile, the transverse decay for the component of the magnetization perpendicular to the B_1 (y’-direction) still decays with the T_2 time according to the Bloch equations. Since the magnetization follows the effective field if the adiabatic condition is fulfilled, only a small contribution of the field is in the y-direction. For many experiments the following less stringent inequality can be applied [18, p. 66]:

$$\frac{1}{T_1} \ll \omega_a(t) \ll |\gamma B_1| > |\gamma B_{loc}| \simeq \frac{1}{T_2} \quad (8.20)$$

Where B_{loc} is the local magnetic field experienced by neighboring spins.

Many pulse shapes are used with several different forms of $\omega(t)$ and $B_1(t)$ [18, 117, 120, 121]. Most of the pulses will also give a time dependence of $B_{eff}(t)$ and $\omega_a(t)$. However, we can try to find a time independent solution by requiring that $dB_{eff}/dt = 0$ and $\omega_a = d\alpha/dt$ is constant. The latter requirement ensures a constant angular velocity of the effective field vector. Then, using equations 8.13 and 8.14 and taking $\omega(t) = \gamma B_0 + \Delta\omega(t)$, we find the following differential equations:

$$0 = B_1(t)\dot{B}_1(t) - \frac{\Delta\omega(t)\Delta\dot{\omega}(t)}{\gamma^2} \quad (8.21)$$

$$\omega_a = \frac{\dot{B}_1(t)\Delta\omega(t)/\gamma + B_1(t)\Delta\dot{\omega}(t)/\gamma}{B_1(t)^2 + \Delta\omega(t)^2/\gamma^2} \quad (8.22)$$

We take the boundary condition such that the spin is aligned to the external magnetic field (in z-direction) at $t=0$. This yields at resonance $\Delta\omega(\frac{\pi/2}{\omega_a}) = 0$ and $B_1(\frac{\pi/2}{\omega_a}) = B_{1_0}$. By solving the differential equations with the latter boundary conditions, we obtain a full adiabatic inversion with the following time dependencies of the B_1 field

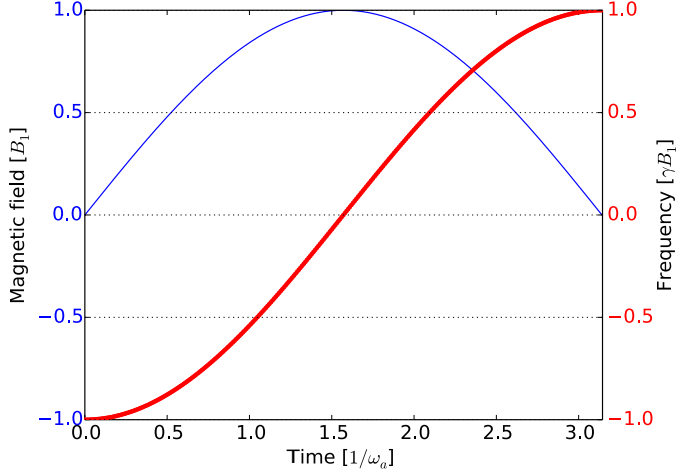


Figure 8.1: Adiabatic rapid passage in which the change in the magnitude of the effective field is zero and in which the tip of the effective field rotates with a constant angular velocity. The red curve corresponds with the frequency sweep of $\Delta\omega$ and the blue curve corresponds with the amplitude modulation of $B_1(t)$.

and angular frequency modulation ($\Delta\omega$):

$$B_1(t) = B_{10} \sin(\omega_a t) \quad 0 \leq t \leq \frac{\pi}{\omega_a} \quad (8.23)$$

$$\Delta\omega(t) = -\gamma B_{10} \cos(\omega_a t) \quad 0 \leq t \leq \frac{\pi}{\omega_a} \quad (8.24)$$

In figure 8.1, the adiabatic inversion pulse is shown. The same adiabatic inversion would have been obtained if we sweep the external magnetic field ($B_0^*(t)$) instead of $\Delta\omega(t)$, according to:

$$B_0^*(t) = B_0 + \Delta B_0 = B_0 + B_{10} \cos(\omega_a t) \quad 0 \leq t \leq \frac{\pi}{\omega_a} \quad (8.25)$$

Since ω_a is constant in these equations, the adiabatic condition without time dependence of ω_a applies for these pulse shapes (see Eq. 8.17).

Other pulse shapes are designed to be more independent of resonance offsets or they are designed to decrease the average or peak power of the RF-radiation. These so called offset independent adiabaticity (OIA) pulses are useful in NMR and MRI to obtain larger signals. In the case of MRFM, one would rather like to have small resonance slices, which omits the requirement of large offset independent pulses. However, it may still be of interest to control the resonance slice thickness with these pulses, to increase the signal to the desired level. In the following, we will evaluate a condition

for offset independent adiabaticity pulses [117]. If we apply the adiabatic condition (Eq. 8.16) with a resonance offset Ω incorporated, we obtain:

$$C(\Omega, t) = \frac{\gamma B_{eff}(t)}{d\alpha(t)/dt} \quad (8.26)$$

$$= \frac{((\Omega - \Delta\omega(t))^2 + \gamma^2 B_1^2(t))}{\gamma \dot{B}_1(t)(\Omega - \Delta\omega(t)) + \gamma B_1(t)|\Delta\dot{\omega}(t)} \gg 1 \quad (8.27)$$

$$= \text{for } |\Omega| \leq \max(|\Delta\omega|) = A \quad (8.28)$$

Where A is the frequency sweep amplitude and C indicates how much the adiabatic condition is fulfilled. In order to obtain high independence of Ω in the bandwidth A , we can require that the condition must be equally satisfied for all Ω . This means that C needs to be independent of Ω , which is satisfied on resonance ($\Omega = \Delta\omega$) at time t_Ω :

$$C(t_\Omega) = \frac{\gamma^2 B_1^2(t_\Omega)}{\Delta\dot{\omega}(t_\Omega)} \gg 1 \quad (8.29)$$

Therefore, we obtain an equation for which the condition satisfies equally well for all $|\Omega| \leq |A|$:

$$C(t_\Omega)\Delta\dot{\omega}(t_\Omega) = \gamma^2 B_1^2(t_\Omega) \quad (8.30)$$

Since at resonance, the effective field is only determined by B_1 , which normally corresponds to the lowest effective field for $B_1 \ll B_0$, the adiabatic condition and Eq. 8.29 is most critical at t_Ω . Therefore we can assume that usually Eq. 8.27 is satisfied for all t within the pulse. The simplest RF pulse which satisfies Eq. 8.30 equally well for all $|\Omega| \leq A$, is a constant B_1 field and a linear frequency sweep. This pulse is often used in MRFM [2, 30, 122]. Therefore the condition in Eq. 8.29 is often shown as the adiabatic condition. Equation 8.30 assembles to Eq. 3.21 for a straight line frequency sweep: $\Delta\omega(t) = A\omega_a \frac{t}{2\pi} - \frac{1}{2}A$ and constant B_1 , where $\omega_a = 2\pi/T_p$ with T_p the pulse length.

From equations 8.23, 8.24 and 8.14, we see that the adiabatic rotation of the spin is only independent of the B_1 field if the rotation is 90 or 180 degrees. For in-plane rotations, such as performed in spin echo experiments, the end phase of an adiabatic in-plane inversion depends on the frequency and magnetic field. Since these are not constant during the pulse, the phases of the components of the magnetization will only slightly refocus after an in-plane rotation. This means that spin echo experiments yield poor results when performed by conventional adiabatic in-plane inversions. This effect can be impaired if a composite pulse like a B_1 insensitive rotation (BIR) pulse is used. This pulse will be described in the next section.

8.6 T_2 measurements with B_1 insensitive rotation (BIR)

In contrast to free induction decay as used in conventional nuclear magnetic resonance (NMR) and magnetic resonance imaging (MRI), in MRFM it is hard to measure the

spin-spin relaxation times (T_2 relaxation), since usually inhomogeneous B_1 fields are present. However, a lot of interesting information is buried in the T_2 relaxation times of materials.

In order to measure the T_2 relaxation times, one usually performs spin-echo experiments. The conventional way of performing spin-echo experiments is by applying a $\pi/2$ π pulse (Hahn echo), in which the magnetization is transferred to the transverse plane where the dephasing occurs, whereupon the components of the magnetization can refocus after being inverted. This procedure only applies when the B_1 field is homogeneous over the sample, since otherwise the majority of spins would not make an exact $\pi/2$ or π pulse. Moreover, in the case of spin-echo experiments for MRFM, the spins have to be transferred to the longitudinal direction after being dephased and refocused. As stated above, since usually in MRFM one has to deal with an inhomogeneous B_1 -field, a spin echo has to be performed with an adiabatic pulse.

In the following, an adiabatic pulse sequence that is used in NMR and MRI will be described, which may be useful for future MRFM experiments in which spin-spin relaxation is relevant.

The pulse sequence and the schematic description of the pulse is shown in figure 8.2. First, the so called BIR-1 will be described, which is the more simple version of the later discussed BIR-4. Both pulses were introduced and described by Garwood et al. [123, 117] The basic idea is to perform an adiabatic pulse in which the dephasing and refocusing occurs due to a combination of a phase delay in the RF pulse and an inversion of the effective field. The phase delay determines the final rotation of the magnetization vector. The BIR-1 pulse consists of two segments and will be described in the rotating reference frame. Again, we assume that initially the magnetization vector is pointed in the z-direction, parallel to the external field.

The pulse starts with the effective field in the transverse plane in the x-direction (in resonance), whereupon the effective field is rotated to the z-axis by an adiabatic sweep. During this sweep the magnetic moment precesses perpendicularly around the effective field to the transverse plane. During this precession, dephasing occurs mainly due to inhomogeneities of the B_1 - and B_0 field. After the end of this adiabatic pulse ($T_p/2$), the effective field is inverted by a sign change with magnitude $\Delta\omega$. At exactly the same moment ($T_p/2$) a phase shift of $\Delta\phi = \pi + \theta$ is introduced in which θ will be the final rotation of the magnetization. For a 90 degrees rotation, one therefore needs a 270 degrees phase shift of the RF pulse. During this event, the rotation direction of the precession changes (in the rotating reference frame), which means that the accumulated phase runs back and therefore refocuses the components of the magnetization. The phase shift causes the effective field to rotate to the -y-axis instead of the x-axis. Due to the symmetry of the pulse, which zeroes the accumulated phase when off-resonance effects are omitted, the magnetization vector ends on the transverse plane in the -x-direction.

In the case of a B_0 field inhomogeneity, yielding a resonance offset Ω , the total accumulated phase may not be zero [117]:

$$\Psi_{tot} = \Psi_1 + \Psi_2 = - \int_0^{T_p/2} B_{eff}(t) dt + \int_{T_p/2}^{T_p} B_{eff}(t) dt \quad (8.31)$$

Where B_{eff} is as Eq. 8.13, from which $\omega(t)$ is shown in figure 8.2. We can see from

the formulas and looking at figure 8.2, that the two integrals (corresponding to the two pulse segments) do not equal each other when a frequency offset is present. As an example, in the case of a positive resonance offset, the difference $\omega_0 - \omega(t)$ is smaller in the first integral than in the second.

This effect can be eliminated by the BIR-4 pulse as described below. Another effect, which cannot be compensated by the BIR-4 pulse but does not depend on the length of the pulse, is the fact that the initial effective magnetic field receives an angle, see Eq. 8.14. The BIR-4 pulse essentially consists of two concatenated BIR-1 pulses with four segments. In segment three, the pulse continues on BIR-1, in which the phase starts to increase (opposite to segment one). In between segment three and four, the effective field is inverted again, with an accompanied phase shift. In this way, the total phase is zero, since $-\Psi_1 = \Psi_3$ and $\Psi_2 = -\Psi_4$. With the BIR-4 pulse, two phase shifts have to be applied in accordance with:

$$\Delta\phi_1 = \pi + \theta/2 \tag{8.32}$$

$$\Delta\phi_2 = -\pi + \theta/2 \tag{8.33}$$

Where θ is the final rotation of the magnetization vector.

The effect of the spin-spin interaction becomes apparent when the short-lived interactions with other spins cause irreversible additional phases to the components of the magnetization. This eventually ends up in a dephased (smaller) magnetization vector. In a free induction decay experiment, this will be apparent after several spin-echo experiments with different delays between the $\pi/2$ and π pulses.

In the case of a BIR-4 180 degree rotation, after dephasing and rotating the magnetization to the z-axis, a resultant smaller z component of the magnetization will be observed. Using different pulse lengths, in which the phase error increases with pulse length, a T_2^* measurement may be performed. Another advantage of the BIR pulse is that any rotation of the magnetization can be performed adiabatically. Note that the T_2 relaxation time of the pulse may not be too short when the B_1 field is much smaller than the local field (B_{loc}), else all information may be lost already during one pulse, see Eq. 8.19 and Eq. 8.20.

8.7 Pulse sequences for MRFM: OSCAR and CERM-IT

The pulse sequences that are described in this section are designed to invert spins in synchronization with the resonance frequency of the cantilever. In the following, the OSCillation Cantilever-driven Adiabatic Reversals (OSCAR) and interrupted OSCAR (iOSCAR) will be described [124, 27]. When the cantilever is moving at its resonance frequency in the presence of a B_1 -field, the dipolar field from the magnet sweeps its resulting resonance slice back and forth through the sample. This creates an oscillating B_0 field around the resonance slice. Looking at Eq. 8.13 and Eq. 8.14, the spins invert back and forth adiabatically. These inversions create a force which either repels or attracts the cantilever, depending on the relative position of the cantilever and the spins as well as on the orientation of the spins. The oscillating force changes

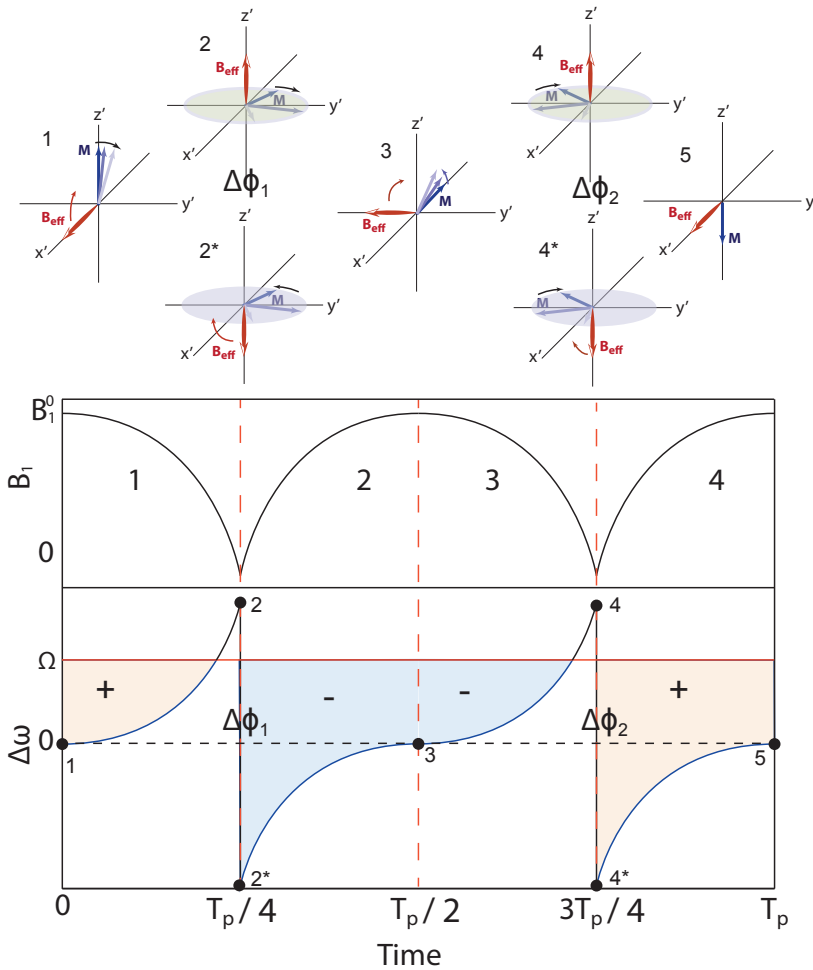


Figure 8.2: The pulse shape of a B_1 independent rotation in the case of a BIR-4 pulse. The simpler BIR-1 pulse, which does not compensate for resonance offsets Ω , consists of just half the BIR-4 pulse with time $T_p/2$. The red dashed lines divide the pulse into 4 segments. On the upper side of the image, the accompanying representation of the pulse in the rotating frame is shown. In this representation, the evolution of the B_{eff} field and the components of the magnetization (M) are shown for the events during the pulse, which are numbered from 1 to 5 and marked by black dots on the curve. Initially, the magnetization is supposed to be in the z' -direction (the accent marks the rotating frame representation). The effective field starts on resonance, and is chosen to be at the x' axis. The magnetization stays perpendicular to the effective field when the adiabatic condition is fulfilled. It rotates around the effective field with its corresponding frequency γB_{eff} . Dephasing occurs mainly due to B_1 field inhomogeneity. The accumulated phase error refocuses again after the abrupt frequency step, in which the effective field changes sign. Due to an added phase shift of 270° between point 2 and 2*, the magnetization ends up in the transverse plane. The same procedure is repeated in segment 3 and 4 to undo the extra phase shift when a resonance offset Ω is present. The compensation of the accumulated phase error due to the offset can be seen by the filled areas, which are related to the accumulated phase error; segment 3 compensates segment 1 and segment 4 compensates segment 2 (at point 2 and 4, the phase accumulation is reversed).

the restoring force from the cantilever, shifting its effective spring constant [124]: $\Delta k = F_{spin}/\Delta z$.

In order to obtain a large and reproducible signal from the spins, the B_1 field is switched on at the maximum deflection of the cantilever. The frequency shift, which corresponds to the spring constant shift can be detected by a PLL-measurement or by frequency detection while self-oscillating the cantilever. The pulse is shown in figure 8.3a. As described in chapter 3 and chapter 6, surface noise, which is responsible for most of the $1/f$ noise at the eigenfrequency of the cantilever, is a major problem of this detection method. For this reason the iOSCAR protocol was introduced, in which the frequency shift is modulated. The protocol is shown in figure 8.3c. This protocol makes use of the fact that the shift of the spring constant changes sign, depending on the relative phase of the movement of the cantilever and the rotations of the spins.

In this protocol, the B_1 field is switched off for half a cycle in every N cycles of the cantilever. During the off-cycle, the relative phase accumulates to a 180 degree phase shift, changing the sign of the frequency shift. The number of cycles (N) determines the frequency of the frequency shift changes: $f(\Delta f) = f_0/2N$. By the use of this protocol, the spin signal of a single electron was detected [27].

Another method, which is very similar to the OSCAR protocol, is the Cantilever Enabled Readout by Magnetization Inversion Transients (CERMIT) protocol [40], see figure 8.3b. In this protocol, the magnetization direction in the resonance slice determines the spring constant shift of the cantilever. Therefore this protocol is based on a different interaction than the OSCAR protocol. The advantage of this protocol is that instead of continuously driving the B_1 field, only one inversion is necessary to shift the resonance. This eventually lowers the power dissipation of the RF source, which will make it easier to reach lower temperatures.

Similar to the iOSCAR protocol, one can also modulate the frequency shift by cyclically inverting the spins, called cyclic CERMIT, see figure 8.3d. Practically, the pulse sequence is exactly the same as the iOSCAR protocol, but with the on and off state of the B_1 field interchanged. Both RF protocols are based on a response to a force gradient, changing the spring constant and therefore the frequency of the cantilever. However, the origin and amplitude of the force interaction are different.

8.8 Pulse sequences for MRFM: cyclic adiabatic driving

A force detection method is favorable, since it is more sensitive than frequency detection, as described in Chapter 3. This requires a method in which the cantilever is cyclically driven by the spins at the eigenfrequency of the cantilever, since static forces only shift the position of the cantilever. However, due to symmetry, when Boltzmann polarization is dominant, only a force from cyclic spin inversions is experienced by the cantilever when it is vibrating towards the surface (a cantilever with the long direction parallel to the surface). One of the first experiments with MRFM having this cantilever configuration was performed with cyclic saturation [125] and later on with cyclic adiabatic inversion [126]. This configuration is not favorable, since the cantilever may snap into contact with the surface, especially with the often used

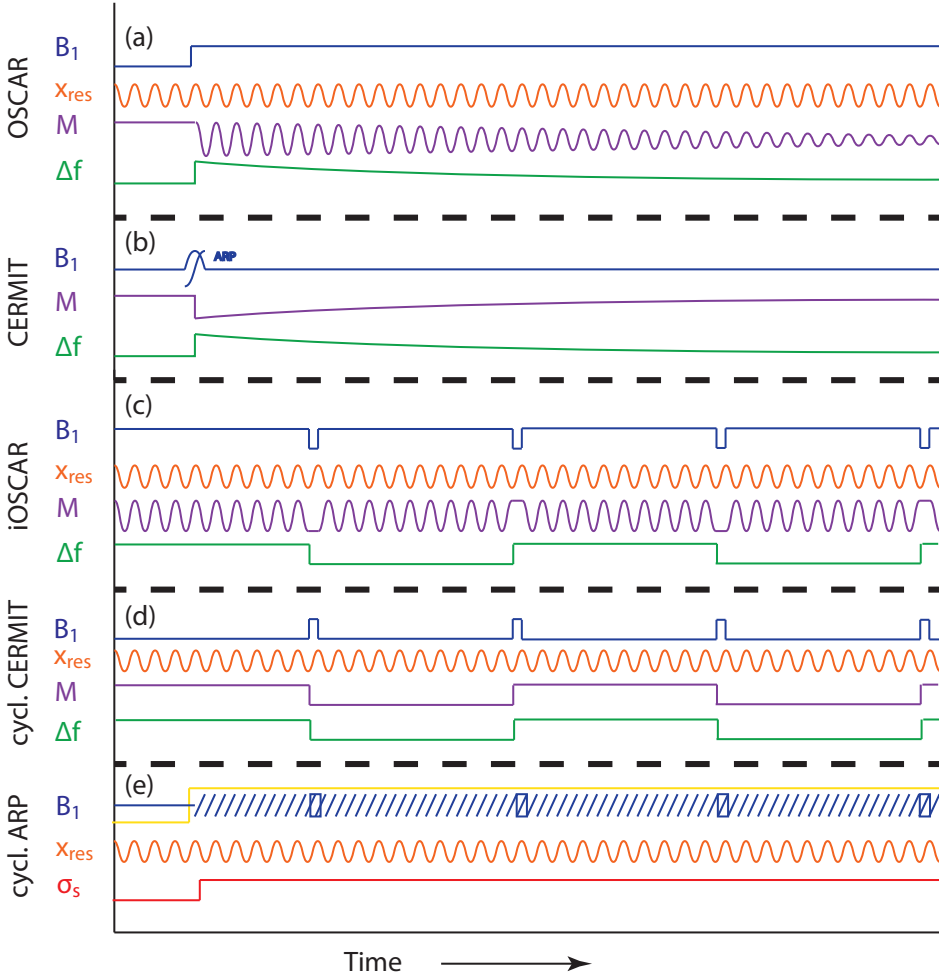


Figure 8.3: Radio frequency pulse sequences used in MRFM. (a) OSCillation Cantilever-driven Adiabatic Reversals (OSCAR) pulse sequence. The motion of the magnetic particle on the cantilever (x_{res}) causes adiabatic inversions when the oscillating magnetic field (B_1) is switched on at a maximum of x_{res} . The oscillating magnetization M causes a frequency shift Δf on the frequency of the cantilever. (b) Cantilever Enabled Readout by Magnetization Inversion Transients (CERMIT). An adiabatic inversion causes a different spin configuration, changing the magnetization and the effective spring constant. (c) interrupted OSCAR (iOSCAR). By periodically switching off the B_1 field, a phase shift of M corresponding to x_{res} changes Δf in synchrony. (d) cyclic CERMIT. By periodically applying adiabatic inversions, the frequency is shifted accordingly. (e) Cyclic adiabatic rapid passages. This pulse is applied for statistically polarized samples. By applying adiabatic inversions at twice the cantilever frequency, the spin inversions create a force on the cantilever depending on the configuration. The variance of these force interactions are translated into a variance σ_s in the in phase component of the cantilever motion. To decrease measuring time, randomization pulses may be applied, which decrease the correlation of spin configurations (the squares in the B_1 field represent the randomization pulses).

floppy MRFM cantilever.

In the case of statistical polarization, a different cantilever orientation may still be used (perpendicular to the surface), since the force on the cantilever is dependent on the configuration of randomly oriented spins. The spin signal can be detected by using cyclic adiabatic pulses at twice the cantilever frequency while measuring the variance of the in-phase signal of the cantilever motion [2, 30, 122], see figure 8.3e. The doubling of the frequency of inversion pulses is required, because a full cycle of spins is obtained after two inversion cycles. This detection method was used for 3D imaging of virus particles with a resolution smaller than 10 nm [2].

A limiting factor, especially at low temperatures, is the required radio frequency current through the RF wire, due to the required fulfillment of the adiabatic condition in Eq. 8.17. The adiabatic condition in ref. [30] for fluorine with a gyromagnetic ratio of 40 MHz/T for a linear frequency sweep with a modulation amplitude of 1.4 MHz corresponding to Eq. 3.21 is equal to 1 if the B_1 field is 2 mT for a 6 kHz pulse frequency (2 times the cantilever frequency). Twice this B_1 -field (4 mT) yields reasonable inversions [30]. Since only one of the rotating directions is in resonance (left rotating or right rotating, see section 8.3), the applied field has to be twice as large. This means that an oscillating magnetic field of 8 mT has to be sent (for a 4 mT B_1 field), which corresponds to an RF current of 20 mA for a sample at a distance of 500 nm from the RF wire such as in ref. [30].

In conclusion; although the force sensitivity increases signal-to-noise ratio, aspects such as cantilever orientation and RF current requirements limit the use of this method.

8.9 T_1 and T_2 measurements with a single adiabatic inversion

As described in the previous section and section 3.5, the necessary RF currents cause considerable heating, even when using a superconducting wire. In our current setup, the heating of the superconducting wire from the required current for cyclic adiabatic rapid passage is too much for measurements at millikelvin temperatures. However, we could perform a single and slower adiabatic passage to invert spins, such that the adiabatic condition 8.17 is satisfied more easily. On the other hand, when the B_1 field is lower than the local magnetic field (B_{loc}) we should take into account that the T_2 time should be large enough to fulfill the condition in Eq. 8.19. In the case of large RF fields, in the order of the local magnetic field or larger, the adiabatic rapid passage is limited by T_1 , see Eq. 8.20 and section 8.5.

In the case of samples in which the spins carrying magnetic moments are close to each other (such as often the case in solids), the T_2 time may especially become short, since the T_2 time is approximately equal to the Larmor period from the local field of the neighboring spins [113, p. 14]. In the case of the copper sample, where the T_2 time is only 0.15 ms, a field larger than 500 μT is enough to considerably increase the effective T_2^* time. The required current at 1 μm from the RF wire is therefore 5-10 mA. The length of the adiabatic pulse may then be much longer, i.e. a fraction of the T_1 time, being $T_1 = 1$ second to 20 seconds depending on the temperature ($T < 1$ K).

The use of slow adiabatic (rapid) passage on silicon is much more feasible, since the natural abundance of ^{29}Si (having a magnetic moment) is only 4.6% [127], yielding a longer T_2 time through larger average neighbor distance. Moreover the B_1 field is easily larger than the local field. The T_2 time is measured to be 25 seconds for undoped natural silicon at room temperature [128, p. 427]. If this T_2 time is dominated by dipolar interactions, it is expected to have little change when going to lower temperatures. Since the T_1 time is very long especially at low temperatures, it may be interesting, for example to measure the T_2 time of ^{29}Si by using the BIR-protocol (see section 8.6) [128, p. 427]. The T_1 time is more than 8 hours at low temperatures (10 K) [128, p. 427]. Any other diluted spin system may also be of interest for slow adiabatic passage.

Appendices

Appendix A

Copper sample fabrication

In this appendix, we will give a detailed description of the fabrication procedure of the copper sample and the pick-up coil.

We used a wafer with a 375 nm NbTiN film with a resistivity of $92 \mu\Omega\text{cm}$ and a critical temperature of 15.3 K.

A.1 Patterning pick-up coil and RF-line

The following procedure was used to pattern a pick-up coil into the superconducting film.

1. Cleaned the sample with acetone, then isopropanol, dried with nitrogen gas.
2. Spin coated chemically enhanced negative resist AR 7700.18 at 4000 rpm
3. Baked at hot plate at 85°C for 1 min.
4. e-beam at $14 \mu\text{C}/\text{cm}^2$ at 30 kV
5. Baked at hot plate at 105°C for 2 min.
6. 60 s developer 300-46
7. 30 s rinsed with stopper millipore H_2O , dried with N_2
8. Baked hot plate at 120°C for 2 min.

A.2 Reactive ion etching

The film and resist was etched in Delft (Kavli Institute of NanoScience) with David Thoen, using a reactive ion etcher, with the following settings:

1. Pre-etch with Gas flow: 12.5 sccm SF_6 and 5 sccm O_2 and RF power 50W_f and 5W_r , Bias Voltage 334 Vb, 8 nT

2. Current stable after 30 seconds.
3. Etched for 7 min and 20 sec plus 20 sec. overetch.
4. Oxygen cleaned 50WF, 5Wr, 445Vb, 6mT, 20sccm for 100 sec.
5. Extra overetch step for 60 sec. We saw a shortcut at the pick-up coil
6. with these settings: SF6/O2, 50Wf, 10Wr, 400Vb

A.3 Fabricating the second copper layer

For the second copper layer, we used the following procedure for patterning the structure:

1. Ultrasonic cleaning with acetone and, several times in new acetone (>3 times)
2. Spin coat 200k PPMA from AllResist 642.12 at 4000 rpm
3. Baked at hot plate at 160 degrees for 3 min.
4. Spin coat 950k PPMA (AllResist 672.045) at 4000 rpm
5. Bake at hot plate at 160 degrees for 3 min.
6. e-beam at $200 \mu\text{C}/\text{cm}^2$ at 30kV.
7. 3 min. developer (AllResist 600.56)
8. 30 seconds stopper isopropanol
9. Dried with nitrogen gas N_2

A.4 Sputtering copper and gold

After the preparation of the sample, the chip was sputtered with a 300 nm copper layer and a 16 nm gold layer with an ATC-sputtermachine, operated by D. Boltje. We used the following parameters for sputtering copper:

1. Argon pressure: 5 mTorr ($7 \cdot 10^{-3}$ mbar)
2. Flow: 25 sccm
3. Current: 400 mA
4. Duration: 18 min, yielding an expected 300 nm with approximately 10 nm roughness.

The sputter parameters for gold are:

1. Argon pressure 10 mTorr ($13 \cdot 10^{-3}$ mbar)
2. Flow: 25 sccm
3. Current: 200 mA
4. Duration: 1 min (16 nm)

A.5 Lift off

Using acetone and an ultrasonic bath, the resist with the copper on top dissolves and the remaining copper stays on the chip. The whole process of applying the second layer of copper was done twice, because the part of the copper structure that had to stick to the silicon had come loose while being in the ultrasonic bath. Although, using a 50°C acetone bath for the second time, it was still needed to use an ultrasonic bath to dissolve the remaining resist with the copper. This second lift-off attempt was successful however.

Appendix B

Transformation algorithm for cantilever positioning

In this appendix, the calculations of the transformation from the heights at the piezoknobs to the xyz-position of the cantilever tip are given. These calculations were used (in chapter 6 and chapter 7) to determine the positions of the cantilever above the samples. The readout of the heights was performed by capacitance sensors, which were calibrated at room temperature.

In figure B.1, the MRFM positioning system and several viewpoints of the piezoknobs are shown. Figure B.1a shows a platform with a cantilever holder attached to it. This platform, shown in figure B.1c can be moved by the piezoknobs to several orientations in comparison with the MRFM cover plate. Since the cantilever holder with cantilever is attached to the platform (sticking out in the figure), the cantilever can be put in any position in the range defined by the piezoknobs. For example, when turning piezoknob 1 to the right (assuming a right-turning screw thread), the platform moves up at piezoknob 1, which results in a movement of the cantilever to the right (in the x-direction). Note that the distance between the contact points may change if piezoknobs are turned. Therefore, degrees of freedom need to be added to the contact points while keeping the platform fixed. This is accomplished by having three different contact points; The contact point of piezoknob 2 is fixed, the contact point of piezoknob 1 can move in only one direction (x-direction) and the contact point of piezoknob 3 can move in xy-direction (any direction in plane), see figure B.1d.

The problem is to find the xyz-position of the cantilever from the heights at the piezoknobs. In reality, the height at piezoknobs is derived from the height at the capacitance sensors, which are positioned close but not exactly at the place of the piezoknobs. The input parameters are therefore the distances (not the directions) at the piezoknobs, d_1 , d_2 and d_3 . In addition, many fixed parameters, set by the design of the MRFM positioning system (design parameters) have to be incorporated for the final calculation. A summary of the input and design parameters are shown in table B.1.

It is convenient to put the origin of the coordinate system at point p_2 , since this

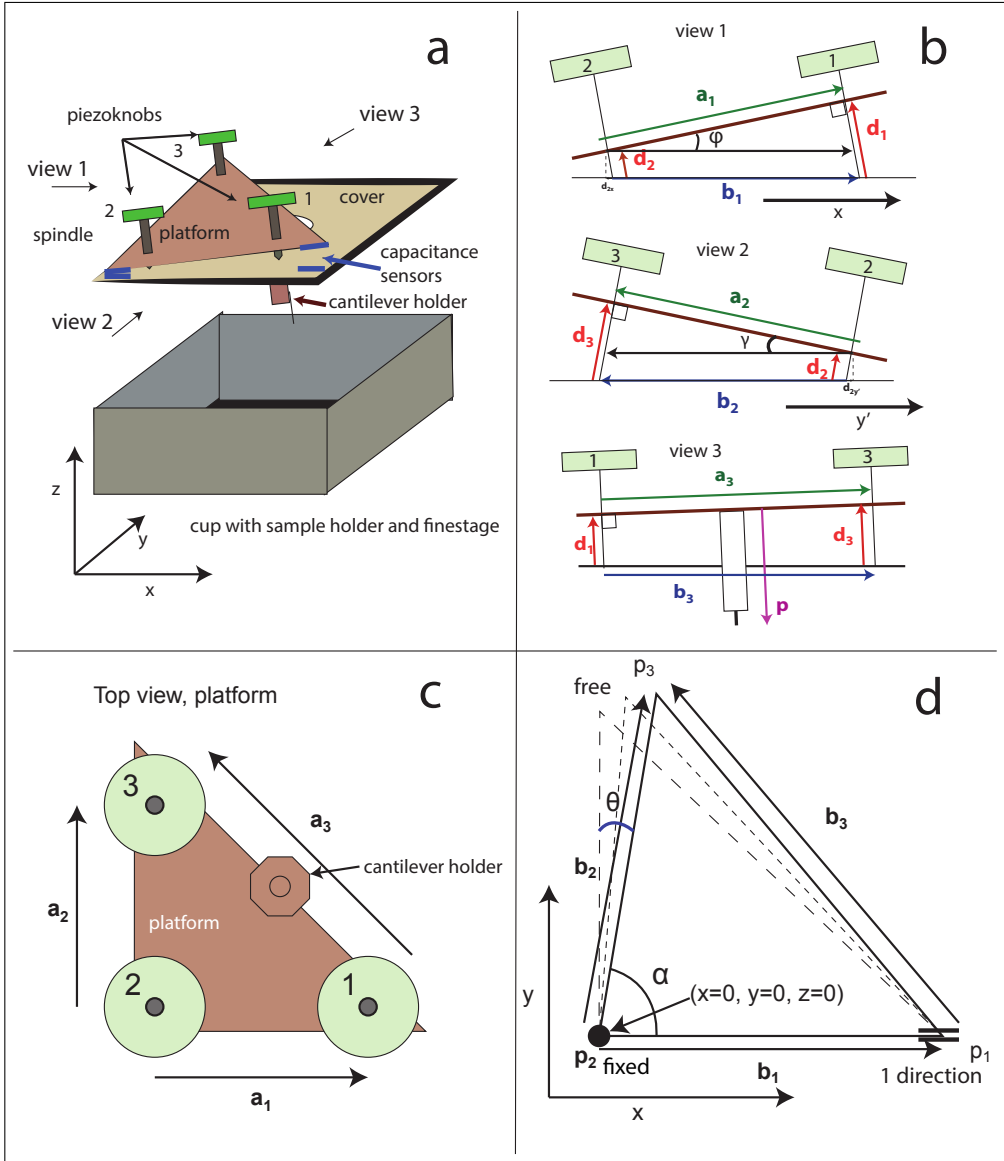


Figure B.1: MRFM positioning system and drawings for the piezoknob transformation calculations. (a) three-dimensional drawing of the MRFM positioning system, the piezoknobs move the platform in comparison with the cover plate. (b) three different views as shown in [a] with the definitions of \mathbf{d}_1 , \mathbf{d}_2 and \mathbf{d}_3 . All three views are perpendicular to the platform. (c) Top view of the platform with the definition of vectors \mathbf{a}_1 and \mathbf{a}_2 . (d) The contact points of the endpoints of the piezoknobs, indicated by p_1 , p_2 and p_3 . At p_1 , the contact point of the piezoknob can only move in the x-direction, at p_2 , the contact point is fixed, which is therefore chosen as the origin, and at p_3 , the contact point can move both in x and y. The vectors \mathbf{b}_1 and \mathbf{b}_2 point to the contact points p_1 and p_2 from the origin (p_2). $\mathbf{b}_3 = \mathbf{b}_2 - \mathbf{b}_1$.

Table B.1: parameters of MRFM positioning system

parameters	meaning	defined in fig.	value
input:			
d_1	distance at piezoknob 1	B.1b view 1, 3	-
d_2	distance at piezoknob 2	B.1b view 1, 2	-
d_3	distance at piezoknob 3	B.1b view 2, 3	-
design:			
a_1	distance between p1, p2 on platform	B.1b,c	38 mm
a_2	distance between p3, p2 on platform	B.1b,c	38 mm
$a_3 = \sqrt{a_1^2 + a_2^2}$	distance between p1, p3 on platform	B.1b,c	54 mm
p	length of the cantilever holder	B.1b view 3	24 mm

point does not move. The route in solving this problem is by finding the vector from the origin to the cantilever in Cartesian coordinates. We first want to find the length of the vectors of the contact points, $b_1 = \|\mathbf{b}_1\|$, $b_2 = \|\mathbf{b}_2\|$ and $b_3 = \|\mathbf{b}_3\|$ in terms of the input- and design-parameters (d_1 , d_2 , d_3 and a_1 , a_2) as defined in figure B.1b, B.1c and B.1d:

From figure B.1b, view 1, we see:

$$b_1 = \sqrt{a_1^2 + (d_1 - d_2)^2} \quad (\text{B.1})$$

Similar for view 2:

$$b_2 = \sqrt{a_2^2 + (d_3 - d_2)^2} \quad (\text{B.2})$$

Similar for view 3:

$$b_3 = \sqrt{a_1^2 + a_2^2 + (d_3 - d_1)^2} \quad (\text{B.3})$$

Hence we can determine the vectors \mathbf{b}_1 , \mathbf{b}_2 , and \mathbf{b}_3 , which are in the xy-plane. Since the contact point p_2 is fixed and p_1 can only move to the right:

$$\mathbf{b}_1 = b_1 \hat{\mathbf{x}} \quad (\text{B.4})$$

For determining \mathbf{b}_2 , we first obtain α and θ from the cosine rule, which are defined in figure B.1d.

$$\alpha = \arccos\left(\frac{b_1^2 + b_2^2 - b_3^2}{2b_1b_2}\right) \equiv \arccos(D) \quad (\text{B.5})$$

Therefore:

$$\theta = \frac{\pi}{2} - \alpha = \arcsin\left(\frac{b_1^2 + b_2^2 - b_3^2}{2b_1b_2}\right) \quad (\text{B.6})$$

Hence:

$$\mathbf{b}_2 = b_2 (\sin \theta \hat{\mathbf{x}} + \cos \theta \hat{\mathbf{y}}) \quad (\text{B.7})$$

$$= b_2 (D \hat{\mathbf{x}} + \sqrt{1 - D^2} \hat{\mathbf{y}}) \quad (\text{B.8})$$

We can derive \mathbf{b}_3 by:

$$\mathbf{b}_3 = \mathbf{b}_2 - \mathbf{b}_1 \quad (\text{B.9})$$

In the following, we determine the vectors which follow the direction of the piezoknob spindles \mathbf{d}_1 , \mathbf{d}_2 and \mathbf{d}_3 , see figure B.1b and B.2a. They all have the same direction, since these vectors are all perpendicular to the platform. Therefore we only need to determine the directions for one of the three vectors. It is convenient to calculate the direction of $\mathbf{d}_2 = d_{2x}\hat{\mathbf{x}} + d_{2y}\hat{\mathbf{y}} + d_{2z}\hat{\mathbf{z}} \equiv d_2\boldsymbol{\epsilon}$. The projection of \mathbf{d}_2 on the x-axis, (d_{2x}), can be found by using figure B.1b:

$$d_{2x} = -d_2 \sin(\phi) \quad (\text{B.10})$$

$$= d_2 \frac{d_2 - d_1}{b_1} \quad (\text{B.11})$$

$$\equiv d_2 \epsilon_x \quad (\text{B.12})$$

Since piezoknob 1 is fixed in the y-direction (moves only in x), d_{2x} does not change when piezoknob 3 changes. In other words, trivially, rotation of the stage around the x-axis does not change d_{2x} . This is not the case in the y-direction, since the contact point of piezoknob 3 may also move in the x-direction. For the projection in the y-direction d_{2y} , we use figure B.2. We can easily calculate the projection of d_2 along the line following \mathbf{b}_2 , which we define as $d_{2y'}$. From figure B.1b, view 2, we find:

$$d_{2y'} = d_2 \sin(\gamma) \quad (\text{B.13})$$

$$= d_2 \frac{d_2 - d_3}{b_2} \quad (\text{B.14})$$

With two projections on the xy-plane and the known magnitude of \mathbf{d}_2 , the vector is uniquely defined. By drawing two lines that intersect perpendicularly at d_{2x} and $d_{2y'}$, the projection of \mathbf{d}_2 on the xy-plane, \mathbf{d}_{2r} , is found (see figure B.2a). The y-component of this vector is equal to d_{2y} . Therefore, using figure B.2a:

$$d_{2x'} = \frac{d_{2y'}}{\sin(\theta)} = \frac{d_{2y'}}{D} \quad (\text{B.15})$$

$$d_{2y} = \Delta d_{2x} \tan(\theta) = (d_{2x'} - d_{2x}) \tan(\theta) \quad (\text{B.16})$$

$$= d_2 \left(\frac{d_2 - d_3}{b_2} - D \frac{d_2 - d_1}{b_1} \right) \frac{1}{\sqrt{1 - D^2}} \quad (\text{B.17})$$

$$\equiv d_2 \epsilon_y \quad (\text{B.18})$$

We can find the z-component of \mathbf{d}_2 by using the x- and y-values:

$$d_{2z} = \sqrt{d_2^2 - d_{2x}^2 - d_{2y}^2} \quad (\text{B.19})$$

$$= d_2 \sqrt{1 - \frac{(d_2 - d_1)^2}{b_1^2} - \left(\frac{d_2 - d_3}{b_2} - D \frac{d_2 - d_1}{b_1} \right)^2 \frac{1}{1 - D^2}} \quad (\text{B.20})$$

$$\equiv d_2 \epsilon_z \quad (\text{B.21})$$

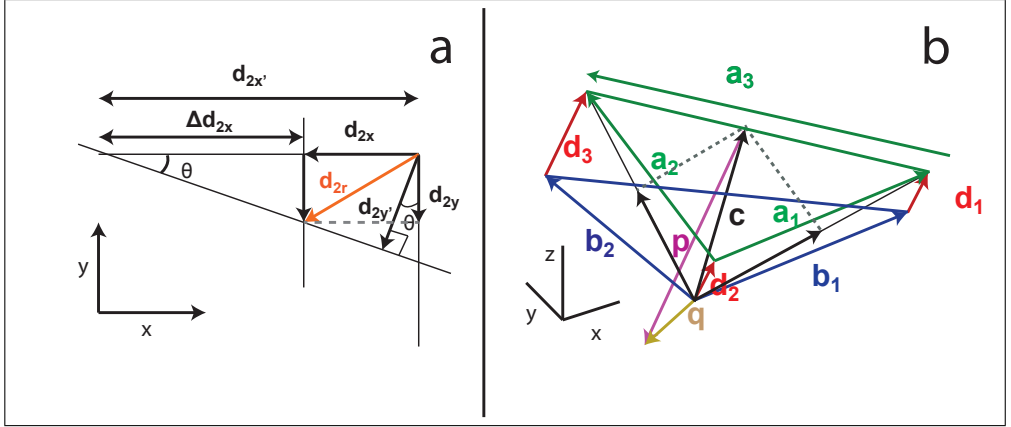


Figure B.2: Vector drawings. (a) Drawing for the calculation of d_{2y} . The components d_{2x} and d_{2y}' are also shown in figure B.1b. The vector \mathbf{d}_{2r} can be composed from d_{2x} and d_{2y}' and represents the projection of \mathbf{d}_2 on the xy -plane. The y -component of this vector is d_{2y} . (b) All vectors that compose the configuration of the positioning system.

Since the vectors \mathbf{d}_1 and \mathbf{d}_3 also have the same direction, we can write:

$$\mathbf{d}_1 = d_1 \epsilon \quad (\text{B.22})$$

$$\mathbf{d}_2 = d_2 \epsilon \quad (\text{B.23})$$

$$\mathbf{d}_3 = d_3 \epsilon \quad (\text{B.24})$$

In figure B.2b, all vectors that compose the configuration of the MRFM positioning system are shown. With the calculated vectors (\mathbf{b}_1 , \mathbf{b}_2 , \mathbf{b}_3 , \mathbf{d}_1 , \mathbf{d}_2 and \mathbf{d}_3) we have sufficient information to find the other vectors. We can for example calculate the vectors \mathbf{a}_1 and \mathbf{a}_2 , which follow the sides of the platform, see also figure B.1c:

$$\mathbf{a}_1 = \mathbf{d}_1 + \mathbf{b}_1 - \mathbf{d}_2 \quad (\text{B.25})$$

$$\mathbf{a}_2 = \mathbf{d}_3 + \mathbf{b}_2 - \mathbf{d}_2 \quad (\text{B.26})$$

These vectors are perpendicular to each other and have values, a_1 and a_2 , given by the design. A check for validity of the above calculations is therefore the calculation of the inproduct: $\mathbf{a}_1 \cdot \mathbf{a}_2 = 0$.

We have defined the vector \mathbf{q} as the vector that points to the cantilever, see figure B.2b. To determine \mathbf{q} , we need to find the vector that points to the attachment of the cantilever holder to the platform, vector \mathbf{c} , and the vector that points from this attachment to the cantilever, vector \mathbf{p} . Since the cantilever holder is perpendicular to the platform, like the spindles, the vector \mathbf{p} is given by:

$$\mathbf{p} = -p\epsilon \quad (\text{B.27})$$

Where p is the length of the cantilever holder. We can find the vector \mathbf{c} by looking

at figure B.2b:

$$\mathbf{c} = \frac{1}{2}(\mathbf{d}_3 + \mathbf{b}_2) + \frac{1}{2}(\mathbf{d}_1 + \mathbf{b}_1) \quad (\text{B.28})$$

$$= \frac{1}{2}(d_3 + d_1)\boldsymbol{\epsilon} + \frac{1}{2}(\mathbf{b}_1 + \mathbf{b}_2) \quad (\text{B.29})$$

Hence, we find for the cantilever position:

$$\mathbf{q} = \mathbf{c} + \mathbf{p} \quad (\text{B.30})$$

$$= \frac{1}{2}(d_3 + d_1 - 2p)\boldsymbol{\epsilon} + \frac{1}{2}(\mathbf{b}_1 + \mathbf{b}_2) \quad (\text{B.31})$$

Decomposed in x, y and z yields:

$$x = \frac{1}{2}(d_3 + d_1 - 2p)\frac{d_2 - d_1}{b_1} + \frac{1}{2}(b_1 + b_2D) \quad (\text{B.32})$$

$$y = \frac{1}{2}(d_3 + d_1 - 2p)\left(\frac{d_2 - d_3}{b_2} - D\frac{d_2 - d_1}{b_1}\right)\frac{1}{\sqrt{1 - D^2}} + \frac{1}{2}b_2\sqrt{1 - D^2} \quad (\text{B.33})$$

$$z = \frac{1}{2}(d_2 + d_1 - 2p).$$

$$\sqrt{1 - \frac{(d_2 - d_1)^2}{b_1^2} - \left(\frac{d_2 - d_3}{b_2} - D\frac{d_2 - d_1}{b_1}\right)^2 \frac{1}{1 - D^2}} \quad (\text{B.34})$$

$$D = \frac{b_1^2 + b_2^2 - b_3^2}{2b_1b_2} \quad (\text{B.35})$$

$$b_1 = \sqrt{a_1^2 + (d_1 - d_2)^2} \quad (\text{B.36})$$

$$b_2 = \sqrt{a_2^2 + (d_3 - d_2)^2} \quad (\text{B.37})$$

$$b_3 = \sqrt{a_1^2 + a_2^2 + (d_3 - d_1)^2}. \quad (\text{B.38})$$

To position the cantilever at a desired location, the reverse transformation, which is the transformation from x, y and z to the heights at the piezoknobs, is useful. For this we can use a linear approximation, since usually the relative movements are small in comparison with the size of the MRFM positioning system. A 30 micrometer movement yields angle changes of less than 0.1 degrees.

We want to approximate the solution around a point where the movements have to take place. In other words, we approximate around the setpoint d_1^0 , d_2^0 and d_3^0 , corresponding to positions x^0 , y^0 and z^0 . A linear approximation near these points can be found via a multidimensional Taylor approximation:

$$\mathbf{q} = \begin{pmatrix} x \\ y \\ z \end{pmatrix} \quad \mathbf{q}^0 = \begin{pmatrix} x^0 \\ y^0 \\ z^0 \end{pmatrix} \quad \mathbf{d} = \begin{pmatrix} d_1 \\ d_2 \\ d_3 \end{pmatrix} \quad \mathbf{d}^0 = \begin{pmatrix} d_1^0 \\ d_2^0 \\ d_3^0 \end{pmatrix} \quad (\text{B.39})$$

$$\mathbf{q} - \mathbf{q}^0 = \mathbf{A}(\mathbf{d}^0)(\mathbf{d} - \mathbf{d}^0) \quad (\text{B.40})$$

with

$$\mathbf{A}(\mathbf{d}^0) = \begin{pmatrix} \frac{\partial x}{\partial d_1}(d^0) & \frac{\partial x}{\partial d_2}(d^0) & \frac{\partial x}{\partial d_3}(d^0) \\ \frac{\partial y}{\partial d_1}(d^0) & \frac{\partial y}{\partial d_2}(d^0) & \frac{\partial y}{\partial d_3}(d^0) \\ \frac{\partial z}{\partial d_1}(d^0) & \frac{\partial z}{\partial d_2}(d^0) & \frac{\partial z}{\partial d_3}(d^0) \end{pmatrix} \quad (\text{B.41})$$

$$d^0 \equiv (d_1^0, d_2^0, d_3^0)$$

Where \mathbf{d} is the vector with the new measured heights at the piezoknobs and \mathbf{q} is the corresponding new position vector of the cantilever. In order to find the linear transformation matrix for the relative heights at the piezoknobs from the relative xyz-position of the cantilever, we just have to take the inverse of this matrix:

$$\mathbf{d} - \mathbf{d}^0 = \mathbf{A}^{-1}(\mathbf{d}^0)(\mathbf{q} - \mathbf{q}^0) \quad (\text{B.42})$$

These calculations are implemented in a Labview program, such that positions can be read out and also new positions can be set.

Bibliography

- [1] J. A. Sidles. “Noninductive detection of single-proton magnetic resonance”. *Applied Physics Letters*, vol. 58, pp. 2854–2856, 1991.
- [2] C. L. Degen, M. Poggio, H. J. Mamin, C. T. Rettner, and D. Rugar. “Nanoscale magnetic resonance imaging”. *Proc. Natl. Acad. Sci. U. S. A.*, vol. 106, no. 5, pp. 1313–7, 2009.
- [3] W. Kühlbrandt. “Cryo-EM enters a new era”. *Elife*, vol. 3, no. e03665, 2014.
- [4] R. McIntosh, D. Nicastro, and D. Mastronarde. “New views of cells in 3D: an introduction to electron tomography”. *Trends in Cell Biology*, vol. 15, no. 1, pp. 43 – 51, 2005.
- [5] J. C. Kendrew, G. Bodo, H. M. Dintzis, R. Parrish, H. Wyckoff, and D. C. Phillips. “A three-dimensional model of the myoglobin molecule obtained by x-ray analysis”. *Nature*, vol. 181, no. 4610, pp. 662–666, 1958.
- [6] H. M. Berman, J. Westbrook, Z. Feng, G. Gilliland, T. N. Bhat, H. Weissig, I. N. Shindyalov, and P. E. Bourne. “The Protein Data Bank”. *Nucleic Acids Res*, vol. 28, pp. 235–242, 2000.
- [7] Protein Data Bank, <http://www.rcsb.org>.
- [8] G. Scapin. “Structural biology and drug discovery”. *Current pharmaceutical design*, vol. 12, no. 17, pp. 2087–2097, 2006.
- [9] M. Congreve, C. W. Murray, and T. L. Blundell. “Keynote review: Structural biology and drug discovery”. *Drug discovery today*, vol. 10, no. 13, pp. 895–907, 2005.
- [10] V. Lounnas, T. Ritschel, J. Kelder, R. McGuire, R. P. Bywater, and N. Foloppe. “Current progress in structure-based rational drug design marks a new mindset in drug discovery”. *Computational and Structural Biotechnology Journal*, vol. 5, no. 6, pp. 1 – 14, 2013.
- [11] T. P. Knowles, M. Vendruscolo, and C. M. Dobson. “The physical basis of protein misfolding disorders”. *Physics today*, vol. 68, no. 3, p. 36, 2015.

- [12] J. P. Overington, B. Al-Lazikani, and A. L. Hopkins. “How many drug targets are there?” *Nat Rev Drug Discov*, vol. 5, no. 12, pp. 993–996, 2006.
- [13] Membrane proteins of known 3D structure, <http://blanco.biomol.uci.edu/mpstruc/>.
- [14] J. J. Babcock and M. Li. “Deorphanizing the human transmembrane genome: A landscape of uncharacterized membrane proteins”. *Acta pharmacologica Sinica*, vol. 35, no. 1, pp. 11–23, 2014.
- [15] E. P. Carpenter, K. Beis, A. D. Cameron, and S. Iwata. “Overcoming the challenges of membrane protein crystallography”. *Current opinion in structural biology*, vol. 18, no. 5, pp. 581–586, 2008.
- [16] Y. Tao, J. Boss, B. Moores, and C. Degen. “Single-crystal diamond nanomechanical resonators with quality factors exceeding one million”. *Nature communications*, vol. 5, 2014.
- [17] A. Vinante, A. Kirste, A. den Haan, O. Usenko, G. Wijts, E. Jeffrey, P. Sonin, D. Bouwmeester, and T. H. Oosterkamp. “High sensitivity SQUID-detection and feedback-cooling of an ultrasoft microcantilever”. *Applied Physics Letters*, vol. 101, no. 12, 123101, 2012.
- [18] A. Abragam. *The Principles of Nuclear Magnetism*. pages: 363 (Ch. 1), 138-139 (Ch. 7), 66, 539-545 (Ch. 8) International series of monographs on physics. Clarendon Press, 1961.
- [19] S. Kuehn, S. A. Hickman, and J. A. Marohn. “Advances in mechanical detection of magnetic resonance”. *The Journal of Chemical Physics*, vol. 128, no. 5, 052208, 2008.
- [20] A. Vinante, G. Wijts, O. Usenko, L. Schinkelshoek, and T. H. Oosterkamp. “Magnetic resonance force microscopy of paramagnetic electron spins at millikelvin temperatures”. *Nature Communications*, vol. 2, 572, 2011.
- [21] J. M. de Voogd, J. J. T. Wagenaar, and T. H. Oosterkamp. “Dissipation and resonance frequency shift of a resonator magnetically coupled to a semiclassical spin”. 2015.
- [22] H. B. Callen and T. A. Welton. “Irreversibility and Generalized Noise”. *Phys. Rev.*, vol. 83, pp. 34–40, 1951.
- [23] H. J. Mamin, R. Budakian, B. W. Chui, and D. Rugar. “Detection and Manipulation of Statistical Polarization in Small Spin Ensembles”. *Phys. Rev. Lett.*, vol. 91, p. 207604, 2003.
- [24] B. Chui, Y. Hishinuma, R. Budakian, H. Mamin, T. Kenny, and D. Rugar. “Mass-loaded cantilevers with suppressed higher-order modes for magnetic resonance force microscopy”. In “TRANSDUCERS, Solid-State Sensors, Actuators and Microsystems, 12th International Conference on, 2003”, vol. 2, pp. 1120–1123. 2003.

- [25] H. C. Overweg, A. M. J. den Haan, H. J. Eerkens, P. F. A. Alkemade, A. L. La Rooij, R. J. C. Spreeuw, L. Bossoni, and T. H. Oosterkamp. “Probing the magnetic moment of FePt micromagnets prepared by focused ion beam milling”. *Applied Physics Letters*, vol. 107, no. 7, 072402, 2015.
- [26] G. H. C. J. Wijts. *Magnetic Resonance Force Microscopy at milliKelvin Temperatures*. pages: 13-39, 31, 87 (Ch. 2), 32-39 (Ch. 5), Ph.D. thesis, Leiden University, 2013.
- [27] D. Rugar, R. Budakian, H. J. Mamin, and B. W. Chui. “Single spin detection by magnetic resonance force microscopy”. *Nature*, vol. 430, no. 6997, pp. 329–332, 2004.
- [28] O. Usenko, A. Vinante, G. Wijts, and T. H. Oosterkamp. “A superconducting quantum interference device based read-out of a subattonewton force sensor operating at millikelvin temperatures”. *Applied Physics Letters*, vol. 98, no. 13, 133105, 2011.
- [29] J. A. Marohn, R. Fainchtein, and D. D. Smith. “An optimal magnetic tip configuration for magnetic-resonance force microscopy of microscale buried features”. *Applied Physics Letters*, vol. 73, no. 25, 1998.
- [30] M. Poggio, C. L. Degen, C. T. Rettner, H. J. Mamin, and D. Rugar. “Nuclear magnetic resonance force microscopy with a microwire rf source”. *Applied Physics Letters*, vol. 90, no. 26, 263111, 2007.
- [31] K. Bastiaans. *Power dissipation of a type II superconducting microwire carrying large oscillating currents at low temperatures*. pages: 32,33 (ch. 2), 9-19, 37 (ch. 3) master thesis, Leiden University, 2015.
- [32] R. N. Kleiman, G. Agnolet, and D. J. Bishop. “Two-level systems observed in the mechanical properties of single-crystal silicon at low temperatures”. *Phys. Rev. Lett.*, vol. 59, pp. 2079–2082, 1987.
- [33] Z. Hao, A. Erbil, and F. Ayazi. “An analytical model for support loss in micromachined beam resonators with in-plane flexural vibrations”. *Sensors and Actuators A: Physical*, vol. 109, no. 12, pp. 156 – 164, 2003.
- [34] E. M. Chudnovsky and D. A. Garanin. “Damping of a nanocantilever by paramagnetic spins”. *Phys. Rev. B*, vol. 89, p. 174420, 2014.
- [35] D. Rugar, O. Zger, S. Hoen, C. S. Yannoni, H.-M. Vieth, and R. D. Kendrick. “Force Detection of Nuclear Magnetic Resonance”. *Science*, vol. 264, no. 5165, pp. 1560–1563, 1994.
- [36] S. Perisanu, P. Vincent, A. Ayari, M. Choueib, S. T. Purcell, M. Bechelany, and D. Cornu. “High Q factor for mechanical resonances of batch-fabricated SiC nanowires”. *Applied Physics Letters*, vol. 90, no. 4, 043113, 2007.

- [37] S. Perisanu, V. Gouttenoire, P. Vincent, A. Ayari, M. Choueib, M. Bechelany, D. Cornu, and S. T. Purcell. “Mechanical properties of SiC nanowires determined by scanning electron and field emission microscopies”. *Phys. Rev. B*, vol. 77, p. 165434, 2008.
- [38] T. R. Albrecht, P. Grtter, D. Horne, and D. Rugar. “Frequency modulation detection using highQ cantilevers for enhanced force microscope sensitivity”. *Journal of Applied Physics*, vol. 69, no. 2, 1991.
- [39] J. I. Kilpatrick, A. Gannepalli, J. P. Cleveland, and S. P. Jarvis. “Frequency modulation atomic force microscopy in ambient environments utilizing robust feedback tuning”. *Review of Scientific Instruments*, vol. 80, no. 2, 023701, 2009.
- [40] S. R. Garner, S. Kuehn, J. M. Dawlaty, N. E. Jenkins, and J. A. Marohn. “Force-gradient detected nuclear magnetic resonance”. *Applied Physics Letters*, vol. 84, no. 25, 2004.
- [41] L. Chen, J. G. Longenecker, E. W. Moore, and J. A. Marohn. “Long-lived frequency shifts observed in a magnetic resonance force microscope experiment following microwave irradiation of a nitroxide spin probe”. *Applied Physics Letters*, vol. 102, no. 13, 132404, 2013.
- [42] K. Kobayashi, H. Yamada, and K. Matsushige. “Frequency noise in frequency modulation atomic force microscopy”. *Review of Scientific Instruments*, vol. 80, no. 4, 043708, 2009.
- [43] Private communication with J.J.T. Wagenaar.
- [44] A. I. B. E. J. Clarke. *The SQUID Handbook, Vol. I Fundamentals and Technology of SQUIDs and SQUID Systems*. pages: 31-42, WILEY-VCH Verlag GmbH and Co. KGaA Weinheim, 2004.
- [45] W. P. Robins. *Phase Noise in Signal Sources: Theory and Applications*. pages: 20-26, Peter Peregrinus Ltd. IEE Telecommunications, 1984.
- [46] J. Kawamura, J. Chen, D. Miller, J. Kooi, J. Zmuidzinas, B. Bumble, H. G. LeDuc, and J. A. Stern. “Low-noise submillimeter-wave NbTiN superconducting tunnel junction mixers”. *Applied Physics Letters*, vol. 75, no. 25, 1999.
- [47] F. Crick and A. Hughes. “The physical properties of cytoplasm: A study by means of the magnetic particle method Part I. Experimental”. *Experimental Cell Research*, vol. 1, no. 1, pp. 37 – 80, 1950.
- [48] S. B. Smith, L. Finzi, and C. Bustamante. “Direct Mechanical Measurements of the Elasticity of Single DNA Molecules by Using Magnetic Beads”. *Science*, vol. 258, pp. 1122–1126, 1992.
- [49] J. G. Longenecker, H. Mamin, A. W. Senko, L. Chen, C. T. Rettner, D. Rugar, and J. A. Marohn. “High-gradient nanomagnets on cantilevers for sensitive detection of nuclear magnetic resonance”. *ACS nano*, vol. 6, no. 11, pp. 9637–9645, 2012.

- [50] A. I. Sidorov, R. J. McLean, B. A. Sexton, D. S. Gough, T. J. Davis, A. Akulshin, G. I. Opat, and P. Hannaford. “Structures magnétiques à l’échelle micrométrique pour l’optique atomique”. *Academie des Sciences Paris Comptes Rendus Serie Physique Astrophysique*, vol. 2, pp. 565–571, 2001.
- [51] S. Whitlock, R. Gerritsma, T. Fernholz, and R. J. C. Spreeuw. “Two-dimensional array of microtraps with atomic shift register on a chip”. *New Journal of Physics*, vol. 11, no. 2, p. 023021, 2009.
- [52] T. J. Davis. “Atomic de Broglie waveguides and integrated atom-optics using permanent magnets”. *Journal of Optics B: Quantum and Semiclassical Optics*, vol. 1, pp. 408–414, 1999.
- [53] Y. T. Xing, A. Eljaouhari, I. Barb, R. Gerritsma, R. J. C. Spreeuw, and J. B. Goedkoop. “Hard magnetic FePt films for atom chips”. *Physica Status Solidi C Current Topics*, vol. 1, pp. 3702–3705, 2004.
- [54] Y. T. Xing, I. Barb, R. Gerritsma, R. J. C. Spreeuw, H. Luigjes, Q. F. Xiao, C. Rétif, and J. B. Goedkoop. “Fabrication of magnetic atom chips based on FePt”. *Journal of Magnetism and Magnetic Materials*, vol. 313, pp. 192–197, 2007.
- [55] R. Gerritsma, S. Whitlock, T. Fernholz, H. Schlatter, J. A. Luigjes, J.-U. Thiele, J. B. Goedkoop, and R. J. C. Spreeuw. “Lattice of microtraps for ultracold atoms based on patterned magnetic films”. *Phys. Rev. A*, vol. 76, no. 3, 033408, 2007.
- [56] V. Y. F. Leung, D. R. M. Pijn, H. Schlatter, L. Torralbo-Campo, A. L. La Rooij, G. B. Mulder, J. Naber, M. L. Soudijn, A. Tauschinsky, C. Abarbanel, B. Hadad, E. Golan, R. Folman, and R. J. C. Spreeuw. “Magnetic-film atom chip with 10 μm period lattices of microtraps for quantum information science with Rydberg atoms”. *Review of Scientific Instruments*, vol. 85, no. 5, 053102, 2014.
- [57] S. Jose, P. Surendran, Y. Wang, I. Herrera, L. Krzemien, S. Whitlock, R. McLean, A. Sidorov, and P. Hannaford. “Periodic array of Bose-Einstein condensates in a magnetic lattice”. *Phys. Rev. A*, vol. 89, no. 5, 051602, 2014.
- [58] M. Poggio and C. Degen. “Force-detected nuclear magnetic resonance: recent advances and future challenges”. *Nanotechnology*, vol. 21, no. 34, p. 342001, 2010.
- [59] B. C. Stipe, H. J. Mamin, T. D. Stowe, T. W. Kenny, and D. Rugar. “Magnetic Dissipation and Fluctuations in Individual Nanomagnets Measured by Ultrasensitive Cantilever Magnetometry”. *Physical Review Letters*, vol. 86, p. 2874, 2001.
- [60] N. E. Jenkins. “Batch fabrication and characterization of ultrasensitive cantilevers with submicron magnetic tips”. *Journal of Vacuum Science Technology B: Microelectronics and Nanometer Structures*, vol. 22, p. 909, 2004.

- [61] S. Rubanov and P. R. Munroe. “FIB-induced damage in silicon”. *Journal of Microscopy*, vol. 214, no. 3, pp. 213–221, 2004.
- [62] L. Giannuzzi and F. Stevie. “A review of focused ion beam milling techniques for TEM specimen preparation”. *Micron*, vol. 30, no. 3, pp. 197 – 204, 1999.
- [63] C. Rossel, P. Bauer, D. Zech, J. Hofer, M. Willemin, and H. Keller. “Active microlevers as miniature torque magnetometers”. *Journal of Applied Physics*, vol. 79, pp. 8166–8173, 1996.
- [64] W. K. Shen, J. H. Judy, and J.-P. Wang. “In situ epitaxial growth of ordered FePt (001) films with ultra small and uniform grain size using a RuAl underlayer”. *Journal of Applied Physics*, vol. 97, no. 10, 10H301, 2005.
- [65] E. C. Heeres, A. J. Katan, M. H. van Es, A. F. Beker, M. Hesselberth, D. J. van der Zalm, and T. H. Oosterkamp. “A compact multipurpose nanomanipulator for use inside a scanning electron microscope”. *Review of Scientific Instruments*, vol. 81, no. 2, p. 023704, 2010.
- [66] J. P. Attané, D. Ravelosona, A. Marty, V. D. Nguyen, and L. Vila. “Coercivity enhancement in FePt nanowires due to the suppression of available paths for domain wall propagation”. *Phys. Rev. B*, vol. 84, p. 144418, 2011.
- [67] J. P. Cleveland, S. Manne, D. Bocek, and P. K. Hansma. “A nondestructive method for determining the spring constant of cantilevers for scanning force microscopy”. *Review of Scientific Instruments*, vol. 64, pp. 403–405, 1993.
- [68] T. N. Ng, N. E. Jenkins, and J. A. Marohn. “Thermomagnetic fluctuations and hysteresis loops of magnetic cantilevers for magnetic resonance force microscopy”. *IEEE Transactions on Magnetism*, vol. 42, pp. 378–381, 2006.
- [69] C. Hammel, private communication.
- [70] R. Gerritsma. *Permanent magnetic atom chips and Bose-Einstein condensation*. Ph.D. thesis, Universiteit van Amsterdam, 2007.
- [71] V. Leung, A. Tauschinsky, N. van Druuten, and R. Spreeuw. “Microtrap arrays on magnetic film atom chips for quantum information science”. *Quantum Information Processing*, vol. 10, no. 6, pp. 955–974, 2011.
- [72] I. Herrera, Y. Wang, P. Michaux, D. Nissen, P. Surendran, S. Juodkazis, S. Whitlock, R. J. McLean, A. Sidorov, M. Albrecht, and P. Hannaford. “Sub-micron period lattice structures of magnetic microtraps for ultracold atoms on an atom chip”. *Journal of Physics D Applied Physics*, vol. 48, no. 11, 115002, 2015.
- [73] K. Uhlig. “Cryogen-free dilution refrigerators”. *Nature*, vol. 485, no. 5, p. 052039, 2012.
- [74] W. J. Nuttal, R. H. Clarke, and B. A. Glowacki. “Resources: Stop squandering helium”. *Journal of Physics: Conference Series*, vol. 400, no. 7400, pp. 573–575, 2012.

- [75] S. H. Pan, E. W. Hudson, and J. C. Davis. “ ^3He refrigerator based very low temperature scanning tunneling microscope”. *Review of Scientific Instruments*, vol. 70, no. 2, pp. 1459–1463, 1999.
- [76] J. Wiebe, A. Wachowiak, F. Meier, D. Haude, T. Foster, M. Morgenstern, and R. Wiesendanger. “A 300mK ultra-high vacuum scanning tunneling microscope for spin-resolved spectroscopy at high energy resolution”. *Review of Scientific Instruments*, vol. 75, no. 11, pp. 4871–4879, 2004.
- [77] E. Tartaglioni, T. G. A. Verhagen, F. Galli, M. L. Trouwborst, R. Mller, T. Shiota, J. Aarts, and J. M. van Ruitenbeek. “New directions in point-contact spectroscopy based on scanning tunneling microscopy techniques (Review Article)”. *Low Temperature Physics*, vol. 39, no. 3, pp. 189–198, 2013.
- [78] Y. J. Song, A. F. Otte, V. Shvarts, Z. Zhao, Y. Kuk, S. R. Blankenship, A. Band, F. M. Hess, and J. A. Stroscio. “Invited Review Article: A 10 mK scanning probe microscopy facility”. *Review of Scientific Instruments*, vol. 81, no. 12, 121101, 2010.
- [79] Cryomech. *Cryogenic Refrigerator manual*.
- [80] A. Waele. “Basic Operation of Cryocoolers and Related Thermal Machines”. *Journal of Low Temperature Physics*, vol. 164, no. 5-6, pp. 179–236, 2011.
- [81] M. Pelliccione, A. Sciambi, J. Bartel, A. J. Keller, and D. Goldhaber-Gordon. “Design of a scanning gate microscope for mesoscopic electron systems in a cryogen-free dilution refrigerator”. *Review of Scientific Instruments*, vol. 84, no. 3, 033703, 2013.
- [82] Leiden Cryogenics, CF-650, Leiden, The Netherlands.
- [83] Cryomech, PT415, Syracuse, NY.
- [84] F. Pobell. *Matter and Methods at Low Temperatures*, p. pages: 225 (Ch. 6). Springer, 3rd ed., 2007.
- [85] K. Uhlig. “ $^3\text{He}/^4\text{He}$ dilution refrigerator with pulse-tube refrigerator precooling”. *Cryogenics*, vol. 42, no. 2, pp. 73 – 77, 2002.
- [86] Amatec, E0360-055-3500S, Alphen aan den Rijn, The Netherlands.
- [87] O. Usenko. *Development and testing of the gravitational wave antenna Mini-GRAIL in its full-featured configuration*. Ph.D. thesis, Leiden University, 2012.
- [88] Geospace Technologies, GS11D, Houston, Texas.
- [89] S. Kelly. *Complex Oxides Studied by Scanning Tunneling Microscopy/Spectroscopy*. Ph.D. thesis, Leiden University, 2012.
- [90] S. Pan. “Piezoelectric motor”, 1993. WO Patent App. PCT/GB1993/000,539.
- [91] PhysikInstrument, P-142.10, Karlsruhe, Germany.

- [92] Leiden Probe Microscopy, LPM, Video Rate SPM Control Electronics, Leiden, The Netherlands.
- [93] Hightech Development Leiden, HDL, SRD1000 sensor and CMN1000 sensor, Leiden, The Netherlands.
- [94] S. Hembacher, F. J. Giessibl, J. Mannhart, and C. F. Quate. “Revealing the hidden atom in graphite by low-temperature atomic force microscopy”. *Proceedings of the National Academy of Sciences*, vol. 100, no. 22, pp. 12539–12542, 2003.
- [95] A. M. J. Den Haan, G. H. C. J. Wijts, F. Galli, O. Usenko, G. J. C. Van Baarle, D. J. Van Der Zalm, and T. H. Oosterkamp. “Atomic resolution scanning tunneling microscopy in a cryogen free dilution refrigerator at 15 mK”. *Rev. Sci. Instrum.*, vol. 85, no. 3, p. 035112, 2014.
- [96] Leiden Spin Imaging, LSI, Leiden, The Netherlands.
- [97] A. M. J. den Haan, J. J. T. Wagenaar, J. M. de Voogd, G. Koning, and T. H. Oosterkamp. “Spin-mediated dissipation and frequency shifts of a cantilever at milliKelvin temperatures”. *Phys. Rev. B*, vol. 92, p. 235441, 2015.
- [98] S. Kuehn, R. F. Loring, and J. A. Marohn. “Dielectric fluctuations and the origins of noncontact friction”. *Phys. Rev. Lett.*, vol. 96, no. 15, p. 156103, 2006.
- [99] B. C. Stipe, H. J. Mamin, T. D. Stowe, T. W. Kenny, and D. Rugar. “Magnetic dissipation and fluctuations in individual nanomagnets measured by ultrasensitive cantilever magnetometry”. *Phys. Rev. Lett.*, vol. 86, no. 13, pp. 2874–2877, 2001.
- [100] J. G. E. Harris, R. Knobel, K. D. Maranowski, A. C. Gossard, N. Samarth, and D. D. Awschalom. “Damping of micromechanical structures by paramagnetic relaxation”. *Appl. Phys. Lett.*, vol. 82, no. 20, pp. 3532–3534, 2003.
- [101] D. Rugar, H. J. Mamin, P. Guethner, S. E. Lambert, J. E. Stern, I. McFadyen, and T. Yogi. “Magnetic force microscopy: General principles and application to longitudinal recording media”. *J. Appl. Phys.*, vol. 68, no. 3, pp. 1169–1183, 1990.
- [102] R. P. Taylor, G. F. Nellis, S. A. Klein, D. W. Hoch, J. Fellers, P. Roach, J. M. Park, and Y. Gianchandani. “Measurements of the Material Properties of a Laminated Piezoelectric Stack at Cryogenic Temperatures”. In “Advances in Cryogenic Engineering”, vol. 824, pp. 200–207. AIP Publishing, 2006.
- [103] D. Haneman. “Electron paramagnetic resonance from clean single-crystal cleavage surfaces of silicon”. *Phys. Rev.*, vol. 170, no. 3, pp. 705–718, 1968.
- [104] B. P. Lemke and D. Haneman. “Low-Temperature EPR Measurements on *in situ* Vacuum-Cleaved Silicon”. *Phys. Rev. Lett.*, vol. 35, pp. 1379–1382, 1975.

- [105] T. Rosskopf, A. Dussaux, K. Ohashi, M. Loretz, R. Schirhagl, H. Watanabe, S. Shikata, K. M. Itoh, and C. L. Degen. “Investigation of surface magnetic noise by shallow spins in diamond”. *Phys. Rev. Lett.*, vol. 112, no. 14, p. 147602, 2014.
- [106] D. A. Alexson, S. A. Hickman, J. A. Marohn, and D. D. Smith. “Single-shot nuclear magnetization recovery curves with force-gradient detection”. *Applied Physics Letters*, vol. 101, no. 2, 022103, 2012.
- [107] A. Abragam. *Principles of Nuclear Magnetism*. 1961.
- [108] C. Slichter. *Principles of Magnetic Resonance*. pages: 12-21 (Ch. 8), Springer Series in Solid-State Sciences. Springer Berlin Heidelberg, 1996.
- [109] J. M. de Voogd, J. J. T. Wagenaar, and T. H. Oosterkamp. “Dissipation and resonance frequency shift of a resonator magnetically coupled to a semiclassical spin”. *ArXiv e-prints*, 2015.
- [110] A. Suter, M. Mali, J. Roos, and D. Brinkmann. “Mixed magnetic and quadrupolar relaxation in the presence of a dominant static Zeeman Hamiltonian”. *Journal of Physics: Condensed Matter*, vol. 10, no. 26, p. 5977, 1998.
- [111] O. Lounasmaa. *Experimental principles and methods below 1 K*. Academic Press, 1974.
- [112] M. Huiku, T. Jyrkkio, J. Kyynarainen, M. Lojonen, O. Lounasmaa, and A. Oja. “Investigations of nuclear antiferromagnetic ordering in copper at nanokelvin temperatures”. *Journal of Low Temperature Physics*, vol. 62, no. 5-6, pp. 433–487, 1986.
- [113] A. Oja and O. Lounasmaa. “Nuclear magnetic ordering in simple metals at positive and negative nanokelvin temperatures”. *Reviews of Modern Physics*, vol. 69, no. 1, p. p. 14, 1997.
- [114] N. Bloembergen. “On the interaction of nuclear spins in a crystalline lattice”. *Physica*, vol. 15, no. 34, pp. 386 – 426, 1949.
- [115] G. P. Berman, B. M. Chernobrod, V. N. Gorshkov, and V. I. Tsifrinovich. “Spin diffusion and relaxation in a nonuniform magnetic field”. *Phys. Rev. B*, vol. 71, p. 184409, 2005.
- [116] C. Kittel. *Introduction to Solid State Physics*. John Wiley & Sons, Inc., New York, 6th ed., 1986.
- [117] A. Tannús, M. Garwood, et al. “Adiabatic pulses”. *NMR in Biomedicine*, vol. 10, no. 8, pp. 423–434, 1997.
- [118] F. Bloch. “Nuclear Induction”. *Phys. Rev.*, vol. 70, pp. 460–474, 1946.
- [119] A. G. Redfield. “Nuclear magnetic resonance saturation and rotary saturation in solids”. *Physical Review*, vol. 98, no. 6, p. 1787, 1955.

- [120] J. Baum, R. Tycko, and A. Pines. “Broadband and adiabatic inversion of a two-level system by phase-modulated pulses”. *Phys. Rev. A*, vol. 32, pp. 3435–3447, 1985.
- [121] Ē. Kupce and R. Freeman. “Stretched adiabatic pulses for broadband spin inversion”. *Journal of Magnetic Resonance, Series A*, vol. 117, no. 2, pp. 246–256, 1995.
- [122] T. Oosterkamp, M. Poggio, C. Degen, H. Mamin, and D. Rugar. “Frequency domain multiplexing of force signals with application to magnetic resonance force microscopy”. *Applied Physics Letters*, vol. 96, no. 8, p. 083107, 2010.
- [123] M. Garwood and Y. Ke. “Symmetric pulses to induce arbitrary flip angles with compensation for RF inhomogeneity and resonance offsets”. *Journal of Magnetic Resonance (1969)*, vol. 94, no. 3, pp. 511–525, 1991.
- [124] B. Stipe, H. Mamin, C. Yannoni, T. Stowe, T. Kenny, and D. Rugar. “Electron spin relaxation near a micron-size ferromagnet”. *Physical review letters*, vol. 87, no. 27, p. 277602, 2001.
- [125] D. Rugar, C. Yannoni, and J. Sidles. “Mechanical detection of magnetic resonance”. *Nature*, vol. 360, no. 6404, pp. 563–566, 1992.
- [126] K. Wago, D. Botkin, C. S. Yannoni, and D. Rugar. “Force-detected electron-spin resonance: Adiabatic inversion, nutation, and spin echo”. *Phys. Rev. B*, vol. 57, pp. 1108–1114, 1998.
- [127] WebElements, <http://www.webelements.com/>.
- [128] P. Bhattacharya, R. Fornari, and H. Kamimura. *Comprehensive Semiconductor Science and Technology, Six-Volume Set: Online version*. page: 427. Elsevier Science, 2011.

Samenvatting

Een kernspinresonantiekrachtmicroscop (zie titel) is een apparaat dat wij ontwikkelen voor het in hoge resolutie in beeld brengen en meten van driedimensionale structuren van materialen.

In dit proefschrift worden methoden en experimenten beschreven die de ontwikkeling van dit apparaat weergeven. Daarnaast laten we metingen zien waarbij, zij het in lagere resolutie, alle eigenschappen van de microscoop worden gebruikt. Het hoofddoel van deze experimenten is om bij te dragen aan de ontwikkeling van een microscoop die driedimensionale structuren van biologische monsters op nagenoeg atomair niveau in beeld kan brengen. Het bereiken van dit doel kan zeker op het gebied van celmembraaneiwitten een significante betekenis hebben, mede omdat deze eiwitten een doelwit vormen voor de ontwikkeling van medicijnen en voor het inzichtelijk maken van de functionaliteit van deze eiwitten. Deze celmembraaneiwitten kunnen door huidige technieken moeilijk in beeld gebracht worden. Naast deze toepassing kunnen tijdens de ontwikkeling van de microscoop ook experimenten worden gedaan voor de wetenschap, waarin met name vaste stoffysica een belangrijk onderdeel kan zijn. Wij laten hiervan twee voorbeelden zien.

Onze groep is gespecialiseerd in het ontwikkelen van deze microscopie techniek bij zeer lage temperaturen, namelijk vanaf 0.01 graad Kelvin boven het absolute nulpunt. Bij deze lage temperaturen is de gevoeligheid groter en kunnen er bijzondere eigenschappen naar voren komen bij complexe materialen in de vaste stoffysica.

Aangezien voor metingen in de vaste stoffysica een minder hoge resolutie vereist is kunnen resultaten in een kleiner tijdsbestek worden verwacht. Gedurende deze experimenten kunnen de (meestal) vereiste verfijningen een grote bijdrage leveren aan het uiteindelijke hoofddoel.

De hierboven genoemde microscoop wordt in het Engels "Magnetic Resonance Force Microscope" genoemd. De werking van de microscoop zit deels in de naam verscholen en heeft gelijkenissen met de werking van de welbekende magnetic resonance imaging (MRI) scanner. In beide technieken worden de magnetische eigenschappen van de kernen van atomen gebruikt. Het is ook mogelijk, zoals in het proefschrift van G. Wijts [26], om de eigenschappen van de elektronen in een materiaal te benutten. Alhoewel het effect van de elektronen vele malen (ongeveer 1000x) groter is dan de effecten van kernen, zijn de gegevens vaak lastig te interpreteren, onder andere vanwege complexe interacties met andere elektronen.

In het volgende gedeelte wordt de microscoop (magnetic resonance force microscope) in het kort uitgelegd.

Afhankelijk van de samenstelling van de kern van een atoom, bevat de kern een magnetisch moment ('magneetje'). Dit wordt veroorzaakt doordat de kern een kwantummechanische eigenschap bezit, namelijk kernspin. In aanwezigheid van een magnetisch veld, zullen deze 'magneetjes' in de kernen zich, net als een kompasnaald, richten in het magnetische veld.

Omdat de temperatuur de richting van de 'magneetjes' ook kan beïnvloeden, zullen bij hoge temperaturen effectief maar weinig 'magneetjes' richten naar het magneetveld (1 op de 200000 voor waterstof bij kamertemperatuur en bij een magnetisch veld van 1 Tesla).

Alleen als de meerderheid van de 'magneetjes' in de richting van het magneetveld staat kunnen ze op een zodanige manier gemanipuleerd worden dat ze gemeten kunnen worden. Een zeer sterk veld, zoals bij een MRI-scanner (3 Tesla tot 7 Tesla), is daarom nodig om voldoende 'magneetjes' te laten richten bij kamertemperatuur (1 op de 30000 bij 7 Tesla). Als het niet om het in beeld brengen van mensen gaat, maar van een klein monster, kunnen we deze ook afkoelen naar zeer lage temperaturen. Bij deze lage temperaturen staan veel meer 'magneetjes' in de richting van het magneetveld, bijvoorbeeld bij 10 mK staat 1 op de 5 'magneetjes' in de richting van een magneetveld van 1 Tesla.

Net als in een MRI-scanner willen we met deze kernspinresonantiekrachtmicroscopie (MRFM) de dichtheid van de 'magneetjes' op alle plekken in het monster bepalen. De nauwkeurigheid van deze microscoop willen we uiteindelijk zodanig verhogen dat we de exacte locatie van ieder 'magneetje' te weten kunnen komen.

Een andere eigenschap die de kernen ('magneetjes') met zich mee brengen is een tollende beweging in een magneetveld. Net als een tol in een zwaartekrachtveld (bijvoorbeeld op aarde) gaat precesseren, zullen deze 'magneetjes' in een magneetveld met een bepaalde frequentie gaan precesseren. Deze frequentie wordt evenredig groter als het magneetveld toeneemt. Hetzelfde geldt voor een tol op de maan, waar die langzamer zal precesseren dan op aarde door een lager zwaartekrachtveld.

Om de 'magneetjes' te kunnen meten moeten deze zodanig gemanipuleerd worden dat deze een ander signaal afgeven. Deze manipulatie kan worden geïnduceerd door radio frequente magnetisch velden (RF-veld) uit te zenden waarvan de frequentie exact gelijk is aan het tollende van de 'magneetjes'. Dit wordt resonantie genoemd. Door dit effect zal het 'magneetje' gaan draaien ten opzichte van het aangelegde magnetische veld. Na deze draaiing zullen de 'magneetjes' een ander signaal afgeven aan de detector.

De detectie in een MRI-scanner geschiedt door middel van een spoeltje dat de veranderende magneetvelden opvangt van de tollende 'magneetjes'. Deze veranderingen zijn maximaal als de 'magneetjes' loodrecht op het aangelegde magneetveld tollende.

De detectie in een magnetische resonantie microscoop wordt op een andere wijze verkregen. Hier wordt de richting (die mogelijk veranderd is door een RF-veld) gemeten door de kracht van deze 'magneetjes' op een ander magneetje, het detectiemagneetje, te meten. Door dit detectiemagneetje vast te maken aan een hefboompje (dun flexibel naaldje) kan deze een bepaalde uitwijking krijgen onder invloed van de richting van de 'magneetjes'. Nauwkeurige meting van de uitwijking van dit detectiemagneetje zegt iets over de kracht die deze 'magneetjes' uitoefenen op het detectiemagneetje.

Zowel in een MRI-scanner als in een kernspinresonantiekrachtmicroscopie (MRFM)

kunnen driedimensionale afbeeldingen gemaakt worden door een speciaal magneetveld aan te leggen waarvan de grootte gradueel varieert in het object of het monster (gradiënt magneetveld). Hierdoor tollen de ‘magneetjes’ op verschillende frequenties in het object of monster, waardoor alleen de ‘magneetjes’ worden gemanipuleerd waarvan de frequentie correspondeert met de frequentie van het RF-veld (radiogolven). Een driedimensionale afbeelding kan worden verkregen door dit gradiënt magneetveld te veranderen of door de frequentie van de radiogolven te veranderen.

In tegenstelling tot een MRI-scanner, waar spoelen worden gebruikt voor het gradiënt magneetveld, wordt in deze krachtmicroscop (MRFM) het detectiemagneetje zelf gebruikt, welke door zijn kleine afmeting (3 micrometer) vanzelf een gradiënt magneetveld creëert, waardoor de ‘magneetjes’ met de ‘juiste’ frequentie vanzelf worden geselecteerd. Een driedimensionale afbeelding wordt in dit geval verkregen via het scannen door het detectiemagneetje in drie dimensies en vervolgens een complex conversiealgoritme toe te passen.

Ondanks dat de resolutie die de krachtmicroscop heeft behaald (10 nanometer) vele malen groter is (1 miljard keer) dan de beste MRI-scanner, moeten vele stappen worden gezet om een gevoeligheid te halen waarbij individuele kernen (‘magneetjes’) zichtbaar worden in drie dimensies. Deze vereiste gevoeligheid ligt aan de zeer kleine kracht van een kernspin op het detectiemagneetje aan het hefboompje, welke slechts rond de 10 zeptonewton ($10 \cdot 10^{-21}$ N) is voor waterstof. Deze kracht is vergelijkbaar met de zwaartekracht tussen een mens en een mug op meer dan 100 meter afstand. De kracht op het magneetje resulteert weer in verplaatsing van het hefboompje met vaak een zeer kleine uitwijking, rond de picometer (10^{-12} meter). Zeker bij lage temperaturen is het een uitdaging om deze kleine bewegingen om te zetten in een meetbaar signaal. Een conventionele manier om deze bewegingen waar te nemen is door middel van een *laser interferometer*, een optische techniek, waarbij het hefboompje wordt beschenen door een laser. Echter bij lage temperaturen zorgt de warmtedissipatie van de laser in het hefboompje voor opwarming, wat ook de gevoeligheid verlaagt.

Wij gebruiken voor het detecteren van de beweging van het hefboompje een “Superconducting Quantum Interference Device” (SQUID). Via een supergeleidend spoeltje zet dit apparaatje de beweging van het magneetje aan het hefboompje om in een elektrisch signaal. Doordat in dit circuit verwaarloosbare dissiperende elementen aanwezig zijn, resulteert deze techniek in een manier om de detectie van de beweging van het hefboompje bij millikelvin temperaturen te meten.

Een andere moeilijkheid bij millikelvin temperaturen is de warmte die ontstaat door het genereren van een RF-veld. Voor het genereren van dit RF-veld, gebruiken we een supergeleidend microdraadje (met een rechthoekige doorsnede van 0.3 micrometer bij 2 micrometer) waar we zo hoog mogelijke RF-stromen doorheen willen sturen. Ondanks dat deze supergeleidende draadjes bij constante stroom geen weerstand hebben, loopt de weerstand snel op wanneer oscillerende stromen met hoge frequenties door dit microdraadje worden gestuurd. Dit resulteert in warmteontwikkeling bij het monster. Deze warmteontwikkeling wordt volgens ons veroorzaakt door kleine ‘wervelwindjes’ van stroompjes die zich verplaatsen [31]. De uitleg en meerdere verbeteringen staan beschreven in hoofdstuk 2 en hoofdstuk 3.

Naast deze technische implementaties is veel aandacht besteed aan onderdelen om de gevoeligheid te verbeteren. Voorbeelden zijn de optimalisatie van het hefboompje,

het verkleinen en versterken van het magneetje en het werken bij lage temperaturen. Zoals eerder gezegd, heeft onze groep zich gespecialiseerd in lage temperaturen, wat de gevoeligheid op twee manieren vergroot. Ten eerste doordat de beweging van het hefboompje door de temperatuur minder wordt en daardoor het spin-sigitaal beter zichtbaar wordt. Ten tweede doordat effectief meer ‘magneetjes’ zich richten in het aangelegde magneetveld.

Daarnaast hebben we het magneetje dat vastzit aan het hefboompje verder verkleind, wat hopelijk een groter gradueel veranderend magneetveld genereert, zoals beschreven in hoofdstuk 4. Dit zorgt voor een grotere selectiviteit omdat er een kleiner frequentiegebiedje correspondeert met de radiofrequentie van de radiogolven. Ook geeft het een betere gevoeligheid, omdat de ‘magneetjes’ in een groter gradiënt magneetveld meer kracht kunnen uitoefenen op het detectiemagneetje aan het hefboompje.

Naast temperatuur kunnen trillingen ook voor extra signaal op het hefboompje zorgen, waardoor het signaal van de ‘magneetjes’ verdoezeld wordt. We gebruiken voor onze opstelling, vanwege de vereiste lage temperaturen, een koelmachine (cryostaat) welke vele vibraties met zich meebrengt. Deze vibraties worden veroorzaakt door een koelmechanisme dat heliumgas in een gesloten compartiment pulserend in en uit het systeem haalt. Ondanks dat er koelmethode zijn waar de trillingen lager zijn heeft deze koelmethode de voorkeur voor MRFM-toepassingen vanwege meerdere redenen: er hoeft geen heliumgas toegevoegd te worden, de experimenteertijd kan veel langer zijn, de ruimte voor het experiment kan groter zijn en het apparaat is minder arbeidsintensief (als er niets defect raakt!).

Desalniettemin is het ook noodzakelijk voor MRFM om deze trillingen tot een minimum te reduceren. Dit kan worden bereikt door meerdere mechanismen in de cryostaat in te bouwen, waaronder veerophanging, demping (d.m.v. eddy current dempers) en loskoppeling van het vibrerende koelmechanisme (de *pulsbuis*). Implementatie hiervan heeft ons in staat gesteld om met dit koelmechanisme een zeer trillingsgevoelige meting uit te voeren met een “Scanning Tunneling Microscope” (STM), waarbij koolstofatomen in beeld zijn gebracht. De technieken voor de trillingsdemping en het STM-experiment staan nauwkeurig beschreven in hoofdstuk 5.

Door de inspanning op onder andere deze technisch uitdagende gebieden zijn wij in staat geweest om voor het eerst kernspinresonantie door middel van mechanische detectie (het detectiemagneetje met hefboompje) bij millikelvin temperaturen (vanaf 43 mK) uit te voeren. Daarnaast hebben we een nieuw formalisme voor de interactie van ongepaarde elektronenspinnen met een MRFM-hefboompje experimenteel kunnen bevestigen door meerdere experimenten uit te voeren boven een siliciummonster met een vanzelf ontstane dunne siliciumoxidelaag. Dit experiment en het kernspinresonantie-experiment staan beschreven in respectievelijk hoofdstuk 6 en hoofdstuk 7.

In het laatste hoofdstuk (hoofdstuk 8) van dit proefschrift worden radiofrequente pulsen beschreven die relevant zijn voor toekomstige onderzoeken in met name onze groep. Het biedt daarnaast ook een achtergrond in een deel van de uitgebreide kernspinresonantietheorie.

Publications

1. A. Vinante, A. Kirste, A. den Haan, O. Usenko, G. Wijts, E. Jeffrey, P. Sonin, D. Bouwmeester, and T. H. Oosterkamp. High sensitivity SQUID-detection and feedback-cooling of an ultrasoft microcantilever. *Applied Physics Letters*, 101(12):123101, 2012
2. A. M. J. Den Haan, G. H. C. J. Wijts, F. Galli, O. Usenko, G. J. C. Van Baarle, D. J. Van Der Zalm, and T. H. Oosterkamp. Atomic resolution scanning tunneling microscopy in a cryogen free dilution refrigerator at 15 mK. *Rev. Sci. Instrum.*, 85(3):035112, 2014
3. H. C. Overweg, A. M. J. den Haan, H. J. Eerkens, P. F. A. Alkemade, A. L. La Rooij, R. J. C. Spreeuw, L. Bossoni, and T. H. Oosterkamp. Probing the magnetic moment of FePt micromagnets prepared by focused ion beam milling. *Applied Physics Letters*, 107(7), 2015
4. A. M. J. den Haan*, J. J. T. Wagenaar*, J. M. de Voogd, G. Koning, and T. H. Oosterkamp. Spin-mediated dissipation and frequency shifts of a cantilever at milliKelvin temperatures. *Phys. Rev. B*, 92:235441, 2015
5. J. J. T. Wagenaar*, A. M. J. den Haan*, J. M. de Voogd, K. M. Bastiaans, T. de Jong, D. J. Thoen, A. Endo, T. M. Klapwijk and T.H. Oosterkamp. Nuclear magnetic resonance force microscopy at milliKelvin temperatures. *in preparation*

* These authors contributed equally

Curriculum Vitae

Arthur Mattheus Johannes den Haan was born on June 18th 1985, in Brouwershaven, The Netherlands.

He completed his first year in electrical engineering at Hogeschool Zeeland, after finishing the school of higher general secondary education (havo) at Pontes Pieter Zeeman in 2003.

In 2004 he started to study physics at Leiden University and obtained his Bachelor of Science degree in 2008, for which he studied the dynamics of silver sulfide and liposomes using a high speed atomic force microscope.

He went on to do a master in experimental physics at Leiden University, for which he performed two master projects in condensed matter physics. First he studied acoustic wave propagation in soft granular matter under supervision of prof. dr. M. van Hecke. In his second project, he studied optimal control feedback in Magnetic Resonance Force Microscopy and characterized a new MRFM setup by using a Scanning Tunneling Microscope in the group of prof. dr. ir. T.H. Oosterkamp. He obtained his Master of Science degree in 2011.

In 2012 he started his PhD at Leiden University on a project funded by the Foundation for Fundamental Research on Matter (FOM), where he continued to work in the group of prof. dr. ir. T.H. Oosterkamp to explore and develop further the Magnetic Resonance Force Microscope for the use in condensed-matter physics systems.

Acknowledgments

I would like to thank my supervisor prof. dr. ir. T. H. Oosterkamp. He supported me in many areas and was very involved, also in difficult times.

Most of the experimental work and analysis shown in this thesis was performed together with Jelmer Wagenaar. Without the good cooperation with him, it would not have been possible to achieve the results presented in this thesis. We contributed equally to the majority of the experiments presented in this thesis. It was hard to get to the point in which the experiment (and especially the cryostat) worked. Without his input, this journey would have been like trying to wire-bond niobium.

Many people from the fine-mechanics department, in particular Gert Koning, Fred Schenkel and Dian van der Zalm have made indispensable contributions to the development of the experiments.

Furthermore I would like to thank the following people:

Bert Crama for helping with the radio-frequency circuitry.

Co Koning, Arno van Amersfoort and Raymond Koehler for their assistance in electronic issues.

Dr. Geert Wijts, Dr. Andrea Vinante and Dr. Sasha Usenko for handing over the experiment and explaining experiments and operations.

Marcel Hesselberth for his expertise and assistance on e-beam lithography and electron microscopy.

Dr. Amrita Singh for assisting the microfabrication of the copper sample with e-beam lithography.

Professor Teun Klapwijk and David Thoen for providing and etching NbTiN, for their expertise in superconductivity and for the involvement in lowering RF-dissipation.

Koen Bastiaans for characterizing the dissipation mechanisms in NbTiN.

Daan Boltje for assisting in the sputtering of copper and gold.

Dr. Mykhailo Azarkh, Dr. Jennifer Mathies and Dr. Peter Gast for magnetizing the magnetic particle on the cantilever.

Dr. Federica Galli and Dr. Gert-Jan van Baarle for helping with the Scanning Tunneling Microscopy.

Dr. Wim Bosch for the help with cryogenic techniques and for assistance in thermometry.

Hiske Overweg, Dr. Lucia Bossoni and Hedwig Eerens, for their contribution to create and characterize a smaller magnetic particle.

Dr. Robert Spreeuw and Dr. Arthur La Rooij for providing the FePt sample.

Professor Jan Aarts and Professor Joost Frenken for their scientific input.

Tobias de Jong, Marc de Voogd and Dr. Lucia Bossoni for their help with simulations. Ellie van Rijsewijk for her support and for the reminders of what is necessary. Dr. Milan Allan for the useful comments on the thesis.

Finally I would like to thank many other people, some of them colleagues, who helped during my PhD: Bob van Waarde, Martin de Wit, Tom van der Reep, Kier Heeck, Oliver Ostojic, Dr. Sven de Man, Gesa Welker, Frank Buters, Dirk van Baarle, Dr. Marcel Rost, Rik Mom, Matthijs van Spronsen, Professor Jan van Ruitenbeek, Sasha Vrbica, Professor John Marohn, Ruud Kuyvenhoven, Andriy Taranovsky, Jeroen Meringa, Samuel Pressac, Dr. Louk Rademaker, Dr. Sander Roobol, Pavel Antonov, Nigel Fennet, Ernst Jan Vegter, Dr. Maarten van Es, Dr. Amir Saedi, Dr. Olaf Benningshof, Dr. Milan Allan, Professor Hans Hilgekamp and Dr. Dapeng Ding I thank my family for their love and support and I thank Jolien Barto for spell checking and for her love.